XLIIIrd RENCONTRES DE MORIOND

Electroweak Interactions and Unified Theories

I V - Neutrino Physics and Astrophysics

CURRENT NUMI/MINOS OSCILLATION RESULTS

A. HABIG,
for the MINOS Collaboration
Department of Physics, University of Minnesota Duluth
10 University Dr., Duluth, MN 55812 USA

The MINOS experiment is now making precise measurements of the ν_μ disappearance oscillations seen in atmospheric neutrinos, and will extend our reach towards the so far unseen θ_{13} by looking for ν_e appearance in the ν_μ beam. It does so by using the intense, well-understood NuMI neutrino beam created at Fermilab and observing it 735km away at the Soudan Mine in Northeast Minnesota. Results from MINOS' first two years of operations will be presented.

1 Introduction

Results from the Super-Kamiokande experiment used neutrinos produced by cosmic ray interactions with the upper atmosphere to show that muon neutrinos (ν_μ) of energies from a few hundred MeV through TeV oscillate to tau neutrinos (ν_τ) as they travel the tens to thousands of kilometers through the earth to the detector [1]. This implies that neutrinos have mass, a finding of fundamental importance to both particle physics and astrophysics. The K2K experiment used a beam of neutrinos shot across Japan to the Super-K detector to confirm this result in a controlled fashion [2]. The MINOS (Main Injector Neutrino Oscillation Search) experiment has unambiguously confirmed this result. MINOS will precisely measure the oscillation parameters using the intense, well-calibrated NuMI (Neutrinos at the Main Injector) beam of neutrinos generated at Fermilab. This neutrino beam was commissioned in early 2005 and is aimed toward the Soudan Underground Physics Laboratory in northeastern Minnesota. The neutrinos are observed by similar magnetized steel/scintillator calorimeters near their origin in Fermilab and after traveling 735 km to Soudan.

Differences in signals between the two detectors have already provided the best measurement yet of $\nu_\mu \leftrightarrow \nu_\tau$ flavor oscillations in a long-baseline accelerator experiment, using the first two years operation of the NuMI neutrino beam [3]. With more data, MINOS will reach its projected

sensitivity to this mixing, improved sensitivity to any sub-dominant ν_e modes (a probe of θ_{13}) and high statistics neutrino cross section studies. This paper presents the current result on $\nu_\mu \leftrightarrow \nu_\tau$ oscillations, the first look at the spectrum of neutral current ("NC") events in the MINOS near detector, the methods which will be used to search for ν_e appearance, and new data-driven sensitivities to θ_{13}.

1.1 The NuMI Beam

The NuMI neutrino beam [4] uses 120 GeV protons from the Main Injector synchrotron at Fermilab incident upon a graphite target. 90% of the primary protons interact over the two interaction-length long target, producing showers of π and K mesons. These showers are focused by a pair of parabolic aluminum "horns", pulsed electromagnets carrying current sheaths which focus the mesons into a beam. This beam is sent down a 1 m radius, 675 m long decay pipe. While in this pipe the mesons have a chance to decay into muons and muon neutrinos, but few of the muons have enough time to further decay before they are absorbed at the end of the pipe, a decay which would produce electron and anti-muon neutrinos. The resulting neutrino beam is thus composed of approximately 92.9% ν_μ, 5.8% $\overline{\nu}_\mu$, 1.2% ν_e and 0.1% $\overline{\nu}_e$ for the low-energy ("LE") beam configuration.

The target and horns are movable with respect to each other, allowing different focusing optics. The result is a beam which is configurable in energy, as seen in Fig. 1. The LE configuration produces a spectral peak closest to the first oscillation minima, given the oscillation parameters measured by Super-K and the 735 km baseline to the far detector. Moving the target with respect to the horns produces the "pME" and "pHE" beams peaked at medium and higher energies. While not at ideal energies for the ν_μ disappearance analysis, these beams are much more intense ($\sim$970 and 1340 neutrino events at the far detector per 10^{20} protons on target, compared to $\sim$390 for the LE beam) and provide extra handles when using the near detector data to model the beam's properties. The MINOS near detector is only a km away from the target, so even the LE beam produces around 10^7 neutrino interactions per 10^{20} protons on target, a very high statistics sample of this weakly interacting particle. The beam currently delivers 3.1×10^{12} protons over a 12 μs spill every 2.2 s for an average power of 270 kW. The NuMI beam has been operational since march of 2005, and to date (of this conference, March 2008) has delivered more than 4×10^{20} protons on target.

1.2 The MINOS Detectors

The MINOS experiment observes the NuMI beam with two detectors, "near" and "far". A third "calibration" detector was exposed to beams of protons, pions, electrons and muons from the the CERN PS [6] to determine detector response. The near detector at Fermilab is used to characterize the neutrino beam with high statistics and is 1 km downstream from the NuMI target. The far detector is an additional 734 km downstream. This experiment compares the spectra of different types of neutrino interactions at these two detectors to test oscillation hypotheses.

All three MINOS detectors are steel-scintillator sampling calorimeters [5] made of alternate planes of 4.1×1 cm cross section plastic scintillator strips and 2.54 cm thick steel plates. The near and far detectors have magnetized steel planes. The calibration detector was not magnetized as the incoming particle momenta were known. The extruded polystyrene scintillator strips are read out with wavelength-shifting fibers and multi-anode photomultiplier tubes. The far detector is 705 m underground in Soudan, MN, in a disused iron mine currently operated as a State Park by the Minnesota Department of Natural Resources. The 5,400 metric ton far detector consists of 486 8 m-wide octagonal steel planes interleaved with planes of plastic scintillator strips.

The 282 plane, 980 metric ton MINOS near detector is located at the end of the NuMI beam facility at Fermilab in a 100 m deep underground cavern. While the NuMI beam has diverged to

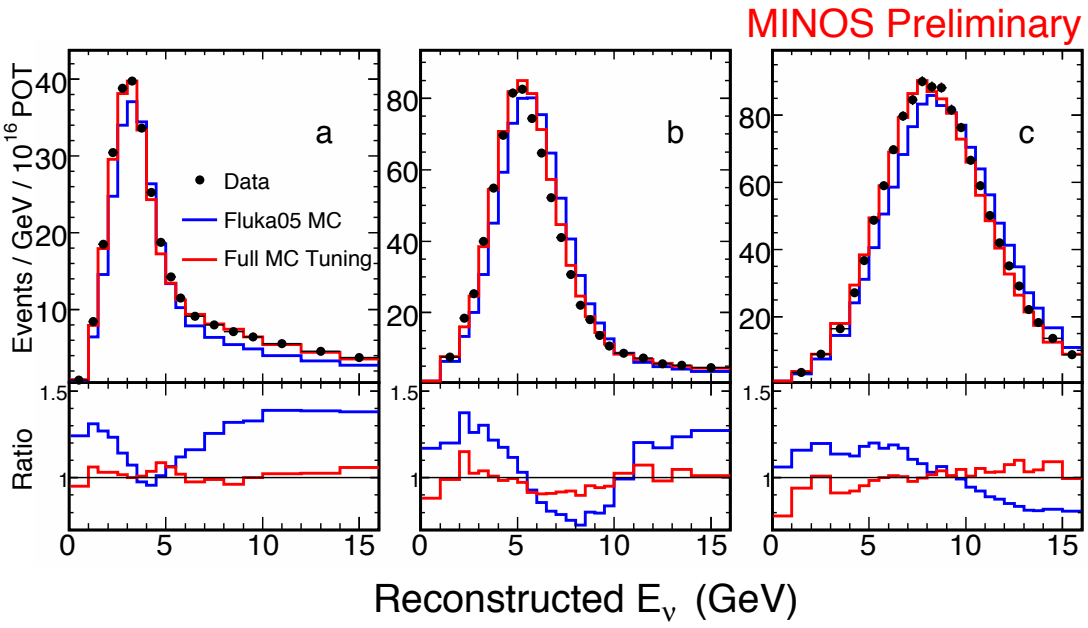

Figure 1: The measured energy spectrum of neutrinos from the NuMI beam observed by the MINOS near detector (top) and the ratios of data and expectations (bottom). Data points are the black dots, the untuned MC predictions are the blue curves, and MC predictions after tuning on hadronic x_F and p_t simultaneously across many different beam configurations are the red curves.

a mile wide at Soudan, at the near detector it is mostly contained in a meter-wide area, allowing a smaller detector and a factor of 10^6 higher neutrino rate.

The much smaller calibration detector was used to measure the detailed responses of the MINOS detectors in a charged-particle test beam. This 12 ton detector consisted of 60 planes of unmagnetized steel and scintillator, each 1×1 m^2 [6]. It measured the energy and topological responses expected in the the near and far detectors, including the different electronics used in both larger devices. The energy responses of the three MINOS detectors were normalized to each other by calibrating with cosmic-ray muons.

2 Data Analysis

MINOS beam-based data is analyzed using a "blind analysis". This method avoids looking at the actual data containing the physics being studied until the very end, removing potential biases and increasing confidence in the final result. Monte Carlo ("MC") predictions are tuned and verified using data not sensitive to the physics in question (*e.g.* near detector data which is at too short a baseline to have experienced oscillations), and analysis cuts and techniques developed solely using simulated data. Only after these techniques are optimized and set are the sensitive data (in this example, the far detector oscillated data) revealed. All three of the results discussed in this paper are blind analyses, and are at different stages in the process.

The first step, common to all beam-based analyses, is to understand the beam itself. A detailed MC tracks simulated particles through the proton-meson-neutrino chain described in Sec. 1.1, to create an expected neutrino spectrum at the near detector. This MC is developed and crosschecked with information from the NuMI beam monitoring system, including a hadron monitor in the absorber at the end of the decay pipe and three muon monitors further downstream. As can be seen in the blue curves in Fig. 1, this does a decent but not perfect job of predicting the observed neutrino spectra in the near detector. Further tuning is done by reweighting hadronic x_F and p_t in the MC simultaneously across seven different beam con-

figurations and comparing to real near detector data, as the hadronic models have the most theoretical uncertainty. Four additional beam configurations (with different horn focusing currents) beyond those shown are included in this fit, and the resulting tuned predictions are the red line in Fig. 1. With the MC truth information in hand, a far detector prediction can be made by applying changes due to mundane things like geometrical and kinematic factors, or more exciting things like neutrino oscillations.

With a beam MC prediction in hand, topological features in the near detector data can be examined. Fitters to find tracks and neutrino interaction vertices, shower-finding algorithms, and particle identification ("PID") routines can be developed, tested, and calibrated using near detector data, the beam MC, and cosmic ray data at both detectors. Once an analysis can correctly matches the real data and the MC data, efficiencies and purities of the resulting sample can be extracted from the MC truth information, systematic uncertainties estimated, and expected sensitivity curves to the final physics parameters calculated. Only at this point is the "box opened", the far detector data run through the analysis, and the hypotheses tested to see what Mother Nature is really doing..

2.1 Atmospheric sector neutrino oscillations

The main goal of the MINOS experiment is a precision measurement of the ν_μ disappearance oscillations first observed in atmospheric neutrinos. In the Standard Model, neutrinos are assumed to be massless and direct neutrino mass measurements have been able to establish only upper limits to their masses. Quantum mechanics predicts that if neutrinos do indeed possess a non-zero mass, then although the neutrinos are created and interact via the weak force as flavor eigenstates (corresponding to the flavors of leptons: electrons, muons and tauons – ν_e, ν_μ, ν_τ) they propagate through space as mass eigenstates (ν_1, ν_2, ν_3). The flavor eigenstates are simple superpositions of the mass eigenstates [7]. If the neutrinos have differing masses, then the flavor of the neutrino varies as these states drift into and out of phase with each other while propagating through space, thus "oscillating" in flavor. For the case of two-flavor oscillations (*e.g.* $\nu_\mu \leftrightarrow \nu_\tau$) the probability that a neutrino produced via the weak interaction in the muon flavor state has oscillated to, or will be detected as, the tau state by the time it interacts is:

$$P_{\nu_\mu \to \nu_\tau} = \sin^2 2\theta_{23} \sin^2 \left(\frac{\Delta m^2_{32} L}{4E_\nu} \right), \tag{1}$$

where the properties of nature being probed are the amplitude or mixing angle θ_{23} and $\Delta m^2_{32} = m^2_3 - m^2_2$. The observable quantities are the energy of the neutrino E_ν and the distance the neutrino has traveled, also called the "baseline" L. Observation of neutrino flavor oscillations which vary as L/E implies that both the terms Δm^2_{32} and $\sin^2 2\theta_{23}$ are non-zero, and that at least one of the participating neutrino flavors has mass.

The analysis techniques discussed above were applied to data from the start of the NuMI beam through March 2007, totaling 2.947×10^{20} "LE" beam protons on target ("pot"). This includes the previously published [3] 1.27×10^{20} pot, although the analysis has been improved for both old and new data. A 3% larger fiducial volume was used, the data reconstruction was improved and retained 4% more good neutrinos, and the PID algorithm was revamped to provide both better purity and efficiency. The resulting sample of 563 ν_μ charged current ("CC") neutrino interactions is plotted as a function of reconstructed neutrino energy on the left of Fig. 2, and a ratio with expectations (right) shows an energy dependent deficit.

Equation 1 was applied on a two-dimensional $(\Delta m^2, \sin^2 2\theta)$ grid to the MC predictions, and a χ^2 formed compared to the data. Estimated systematic errors are less than the current statistical errors and applied as penalty terms to the χ^2. The best fit value for the oscillation

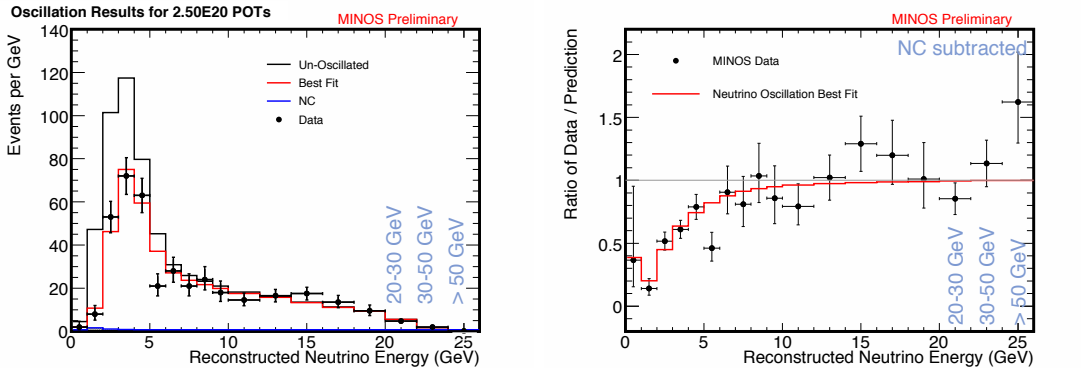

Figure 2: (Left) The observed ν_μ energy spectrum seen in the MINOS beam at the far detector for an exposure of 2.947×10^{20} pot. Black crosses are the data with statistical error bars, the black line the null hypothesis, the red line the expectations of the best fit oscillation scenario of $\left|\Delta m^2_{32}\right| = 2.38^{+0.20}_{-0.16} \times 10^{-3}\,\mathrm{eV}^2$, $\sin^2 2\theta_{23} = 1.00_{-0.08}$, and the blue line (barely visible in the first few energy bins) the expected NC contamination. (Right) The same quantities expressed as a ratio of observed over expected null hypothesis.

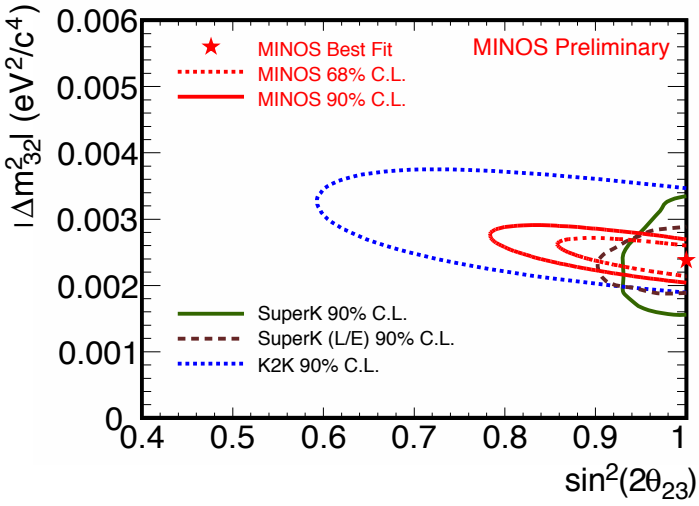

Figure 3: The allowed regions in the oscillation parameter space of Eq. 1, obtained by fitting reweighted MC predictions to the MINOS data in Fig. 2. MINOS results (red) at 68% and 90% c.l. are compared to Super-K results (green) [1, 8] and K2K results (blue) [2] at 90% c.l.

parameters to the MINOS data are $\left|\Delta m^2_{32}\right| = 2.38^{+0.20}_{-0.16} \times 10^{-3}\,\mathrm{eV}^2$ and $\sin^2 2\theta_{23} = 1.00_{-0.08}$, and the resulting 68% and 90% confidence limit contours are shown in Fig. 3.

2.2 Neutral Current Interactions

The ν_μ disappearance results discussed in the previous section (2.1) use topological information to form a PID to select a sample of CC ν_μ neutrinos, on the assumption that the flavor they are disappearing to is ν_τ, an active flavor of neutrino, unobserved in MINOS since the bulk of the NuMI neutrino flux is at energies below τ production threshold. However, if the second flavor of neutrino is a non-standard model sterile neutrino (one which experiences no weak interactions), the disappearance signature could look the same with very different underlying physics.

NC neutrino interactions hold the key to separating these two scenarios in MINOS. Active neutrinos of any flavor can experience a NC Z^0 exchange with a nucleon in the detector and produce a diffuse electromagnetic shower from the resulting π^0 decay to $\gamma\gamma$. A hypothetical sterile neutrino would not, so if some fraction of the ν_μ signal is changing to ν_s, the NC spectrum

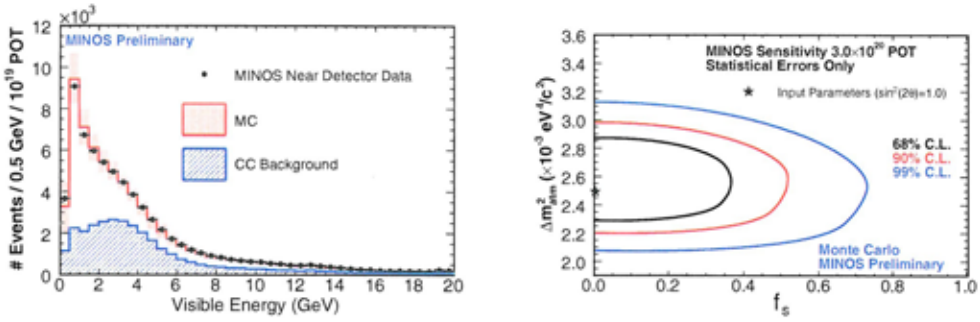

Figure 4: (Left) The spectrum of NC-selected events seen in the near detector for an exposure of 3.0×10^{20} pot. The black dots are the reconstructed neutrino data, the red boxes the expected signal (systematic error bands as the area), and the blue region the expected CC contamination to this NC signal. (Right) The projected sensitivity to a fraction of $\nu_m u$ disappearance to sterile rather than active neutrinos, as a function of Δm^2.

would be distorted and NC flux reduced. A simple set of cuts has been applied to the near detector data to select a NC-rich sample of neutrino interactions for further study. Short tracks (<60 planes) are selected, then events with either no track at all or no track beyond five planes from the shower are chosen. The resulting spectrum of NC near detector neutrino interactions is shown in the left of Fig. 4, with projected limits on f_s (the fraction of disappearance to ν_s shown on the right if no NC disappearance is observed.

This analysis is in the middle of the "blind" analysis scheme discussed above. Having chosen a set of topological cuts to select a NC signal, data and MC comparisons are being made with near detector data to verify that they are well understood before looking at the far detector data to see what the potentially oscillated signal might look like. This analysis is expected to be complete the summer of 2008.

2.3 Sensitivity to ν_e appearance

A third possibility for which particle the ν_μ's are disappearing to is ν_e. We know that there could be some natural mixing between all three active flavors of neutrinos, and the amplitude of this is parametrized as θ_{13}. The Chooz reactor experiment saw no evidence of the converse ν_e disappearance at short baselines to establish an upper limit on θ_{13} [9]. However, the presence of ν_e in the MINOS far detector beyond the low (1.3%) level inherent to the NuMI beam could provide evidence for a non-zero θ_{13} below the Chooz limit, if the background of hadronic showers masquerading as electromagnetic showers can be overcome. The PID algorithm used for ν_e selection uses a neural net technique to pick out ν_e-induced showers. At the near detector the baseline is far too short for ν_μ to have oscillated to ν_e, so any observed ν_e must either be inherent in the beam or the mis-reconstructed hadronic showers in question. To improve the MC estimations of what the levels of these backgrounds might really be in the MINOS detectors, data-driven sensitivity studies have been performed by close examination of near detector data tagged as ν_e events.

Two methods are used in these studies. The first is to take the well-understood class of CC events and subtract out those parts of the event associated with the muon track, leaving only any hadronic component near the interaction vertex caused by the nucleon's share of the interaction energy. These "Muon-Removed Charged Current" (MRCC) events which are mis-classified as ν_e interactions are exactly the sort of electromagnetic-dominated hadronic showers that form a large part of the background for a ν_e appearance search. There is a 20% discrepancy between the data and the MC predictions in both the standard ν_e and MRCC samples with the MC overestimating the background. Comparisons of standard data and MC shower topological

distributions disagree in the same way as does MRCC data with MRCC MC, confirming that hadronic shower modeling is a major component of the disagreement. The MRCC sample is thus used to make and ad-hoc correction to the model to NC events per bin, taking the beam ν_e from the well-understood beam MC.

A second method for estimating the ν_e background from hadronic showers uses comparisons between the neutrino beam produced when the focusing horn's current is turned off and the standard LE beam. The actual composition of the selected ν_e events is quite different in the two cases, allowing for the algebraic deconvolution of the different background components by expressing the total number as a sum of the different parts in the case of each beam:

$$\begin{aligned} N_{on} &= N_{NC} + N_{CC} + N_e \\ N_{off} &= r_{NC}N_{NC} + r_{CC}N_{CC} + r_eN_e \end{aligned} \tag{2}$$

where N_{NC} and N_{CC} are the numbers of background events present originating from CC or NC interactions, N_e the inherent beam ν_e taken from the beam MC, and the r's the ratios that hold the differences between the two equations, $r_{NC(CC,e)} = N^{off}_{NC(CC,e)}/N^{on}_{NC(CC,e)}$. The horn on/off ratios are extracted bin-by-bin in energy from the MC, are independent of hadronic modeling, and match well between data and MC. These fractions can then be applied to the data itself to extract the components of the background, indicating that there is 24% too much CC and 28% too much NC backgrounds in the MC. Checks with a third (pHE) beam produce similar results, and both are compatible with the corrections from the MRCC method outlined above.

These data-drive backgrounds can then be extrapolated to the far detector for use in establishing the sensitivity expected when using a ν_e appearance search to try and measure θ_{13}. These sensitivities are presented in Fig. 5 for three different exposures, the current 3.25×10^{20} pot as well as those expected for next two years. The systematic errors for the current background estimation are found to be 10%, and with more data and study it is projected to fall to 5% for future years. The unknown variable of CP-violating δ contributes to ν_e appearance through the matter effects on the beam between Fermilab and Soudan, so the y-axis of these plots shows the effect of this δ. The actual sign of $\Delta m^2 32$ also enters in, making this analysis less sensitive for the "inverted" mass hierarchy. However, after two more years of exposure MINOS will be sensitive to θ_{13} below the Chooz limit for most combinations of δ and mass hierarchy. The next step in this blind analysis is to examine far detector data in "sidebands" that allow verification of techniques without being sensitive to actual ν_e appearance.

3 Summary

The MINOS long-baseline neutrino experiment has been receiving 735 km baseline neutrinos from the NuMI neutrino beam since early 2005. The primary experimental goal of a precision measurement of the $\nu_\mu \leftrightarrow \nu_\tau$ disappearance oscillation parameters has been achieved. With the first 2.5×10^{20} protons on target, $|\Delta m^2_{32}| = 2.38^{+0.20}_{-0.16} \times 10^{-3}\,\mathrm{eV}^2$ and $\sin^2 2\theta_{23} = 1.00_{-0.08}$. This is about a quarter of the expected final exposure, which will allow fine distinction between alternative disappearance hypotheses such as decoherence and neutrino decay to be made in the future. The first measurement of the spectrum of neutral current neutrino interactions has been made in the high-statistics near detector data. When the blind analysis of the corresponding far detector is complete later this year, it will be sensitive to a sterile neutrino fraction $f_s \leq 0.5$ at 90% c.l. Again using the near detector data, a data-driven background estimate to the ν_e appearance analysis has been made. This yields a sensitivity estimates comparable to the Chooz limit for the currently available exposure of 3.25×10^20 protons on target, reaching several times lower than this limit as soon as next year.

The NuMI beam and the MINOS experiment are going strong, the data and beam are well understood, and quality results are being produced. The next year should see the completion

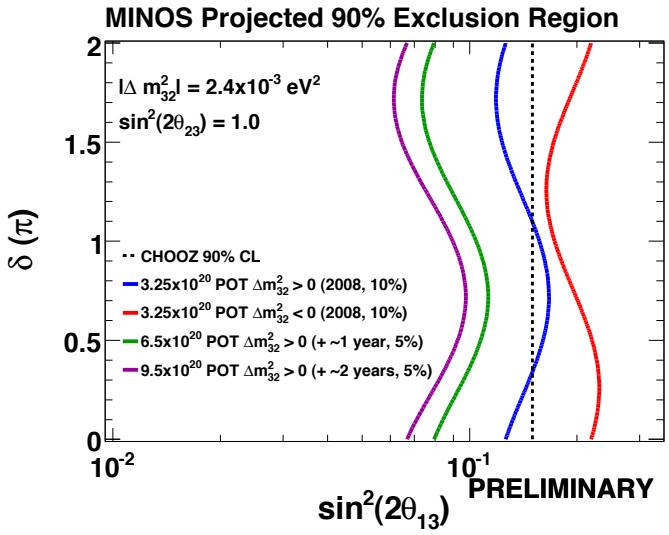

Figure 5: Projected 90% c.l. limits on θ_{13} as a function of CP-violating δ from the MINOS experiment in the absence of a ν_e appearance signal. These limits use data-driven background estimates from the near detector. The vertical dashed line is the Chooz limit [9]. The rightmost (red) curve is the limit using the current exposure in the case of an inverted mass hierarchy, the neighboring (blue) curve is the limit from the same exposure if nature has a normal neutrino mass hierarchy. The two curves on the left are the progressively more sensitive normal hierarchy limits for the increased NuMI beam exposure over the next two years. The corresponding inverted hierarchy curves for these two scenarios are not shown for ease of viewing, but improve over the current exposure limits in a corresponding manner to the normal curves.

of initial analyses on all major experimental goals and the continued refinement of the precision parameter measurement of neutrino oscillations in the atmospheric neutrino sector.

Acknowledgments

We thank the Fermilab staff and the technical staffs of the participating institutions for their vital contributions. This work was supported by the U.S. Department of Energy, the U.S. National Science Foundation, the U.K. Science and Technologies Facilities Council, and the State and University of Minnesota. We gratefully acknowledge the Minnesota Department of Natural Resources for their assistance and for allowing us access to the facilities of the Soudan Underground Mine State Park and the crew of the Soudan Underground Physics laboratory for their tireless work in building and operating the MINOS detector.

References

1. Y. Ashie *et al.*, Phys. Rev. D **71**, 112005 (2005).
2. M. H. Ahn *et al.*, Phys. Rev. D **74**, 072003 (2006).
3. P. Adamson *et al*, Phys. Rev. D **77**, 072002 (2008).
4. A. G. Abramov *et al.*, Nucl. Instrum. Meth. **A385**, 209 (2002).
5. D. G. Michael *et al* submitted to Nucl. Instrum. Meth. **A** (2008).
6. P. Adamson *et al*, Nucl. Instrum. Meth. **A566**, 119 (2006).
7. B. Pontecorvo, Sov. Phys. JETP **6**, 429 (1957); Zh. Eksp. Teor. Fiz. **33**, 549 (1957).
8. Y. Ashie *et al.*,Phys. Rev. Lett **93**, 101801 (2004).
9. M. Apollonio *et al.*, Phys. Lett. **B466**, 415 (1999).

FIRST NEUTRINO EVENTS IN THE OPERA EMULSION TARGET

C. PISTILLO
Universität Bern, Laboratorium für Hochenergie Physik,
Sidlerstrasse 5, CH-3012 Bern

OPERA is a long baseline neutrino oscillation experiment designed to observe $\nu_\mu \to \nu_\tau$ oscillations by searching for the appearance of ν_τ's in an almost pure ν_μ beam. The beam is produced at CERN and sent towards the Gran Sasso INFN laboratories where the experiment is running. OPERA started its data taking in October 2007, when the first 38 neutrino interactions where successfully located and reconstructed. This paper reviews the status of the experiment discussing its physics potential and performances for neutrino oscillation studies.

1 Introduction

OPERA [1] is a long baseline experiment at the Gran Sasso underground laboratories (LNGS) and is part of the CERN Neutrino to Gran Sasso (CNGS) [3] project. The detector has been designed to observe the $\nu_\mu \to \nu_\tau$ oscillations in the parameter region indicated by Super-Kamiokande [2] through direct observation of ν_τ charged current interactions. The detector is based on a massive lead/nuclear emulsion target complemented by electronic detectors that allow the location of the event and drive the scanning of the emulsions. A magnetic spectrometer follows the instrumented target and measures charge and momentum of penetrating tracks.

The CNGS beam is designed to provide $45 \cdot 10^{18}$ proton-on-target/year (p.o.t./y) with a running time of 200 days per year. The first CNGS technical run occurred in August 2006 with a delivered luminosity of $0.76 \cdot 10^{18}$ p.o.t. At that time only the electronic detectors were installed and under commissioning.

The first physics run occurred in October 2007, when OPERA had 40% of the target mass installed. Due to technical problems, only $0.79 \cdot 10^{18}$ p.o.t. were delivered. A new physics run is going to start in summer 2008 with a planned luminosity of $\sim 30 \cdot 10^{18}$ p.o.t.

2 The OPERA detector

OPERA is a large detector (10 m $\times$ 10 m $\times$ 20 m) located in the underground experimental Hall C of LNGS. As shown in Figure 1, the detector is made of two identical super-modules, aligned along the CNGS beam direction, each one consisting of a target and a muon spectrometer. The target section combines passive elements, the lead-emulsion bricks, and electronic detectors. Each target section consists of a multi-layer array of 31 target walls followed by pairs of planes of plastic scintillator strips (Target Tracker). A magnetic spectrometer follows the instrumented target and measures charge and momentum of penetrating tracks.

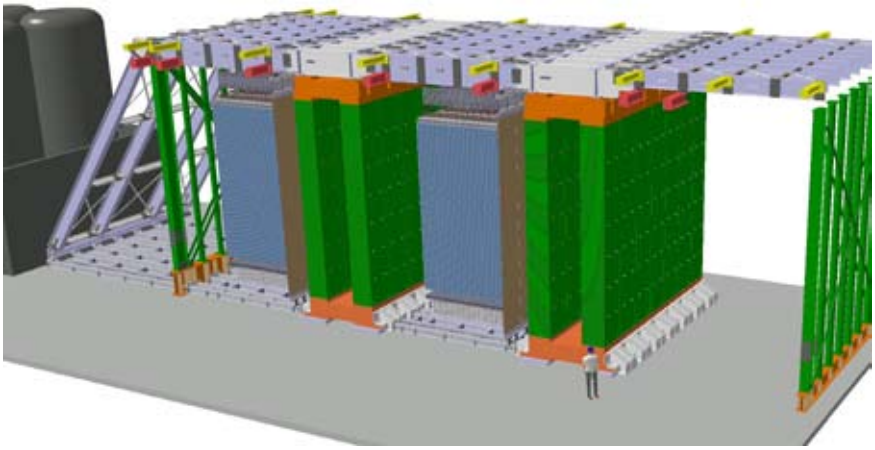

Figure 1: *Schematic view of the OPERA detector. The neutrino beam enters the detector from the left.*

2.1 The Emulsion Target

The development of automatized scanning systems during the last two decades has made possible the use of large nuclear emulsion detectors. Indeed, nuclear emulsion are still successfully used nowadays, especially in neutrino experiments [4,5]. The realization of a new scanning system has been carried out by two different R&D programs in the Nagoya University (Japan) and in several european laboratories belonging to the OPERA collaboration. These scanning systems [6,7,8] were designed to take into account the requests of high scanning speed (about 20 cm^2/h) while keeping the extremely good accuracy provided by nuclear emulsions. For the european system, the Bern group took in particular the responsability to develop an automatic emulsion film changer [9] and to implement an innovative technique of nuclear emulsion scanning with the use of dry lenses instead of oil immersion ones (as it was always in the past), in order to simplify the emulsion handling [10]. About 40 automatic microscopes are installed in the various scanning laboratories of the OPERA experiment.

The total number of emulsion films in the OPERA detector will be about 9 millions, for an area of about 110000 m^2. These quantities are orders of magnitude larger than the ones used by previous experiments. That made necessary an industrial production of the emulsion films, performed by the Fuji Film company, in Japan, after an R&D program conducted jointly with the OPERA group of the Nagoya University.

The OPERA emulsions are made up of two emulsion layers 44 μm thick coated on both sides of a 205 μm triacetate base. The AgBr crystal diameter is rather uniform, around 0.2 μm, and the sensitivity is about 35 grains/100 μm for minimum ionizing particles.

The main constituent of the OPERA target is the brick. It is a pile of 57 nuclear emulsion sheets interleaved by 1 mm thick lead plates. The brick combines the high precision tracking capabilities provided by the emulsions with the large mass given by the lead. The OPERA brick is a detector itself. In addition to the vertex identification and τ decay detection, shower reconstruction and momentum measurements using the Multiple Coulomb Scattering can be performed, being the total brick thickness of 7.6 cm equivalent to 10 X_0. Bricks are hosted in the walls of the target.

The occurrence of a neutrino interaction inside the target is triggered by the electronic detectors. Muons are reconstructed in the spectrometers and all the charged particles in the target tracker. The brick finding algorithm indicates the brick where the interaction is supposed to be occurred. The trigger is confirmed in the Changeable Sheet Doublet (CSD) [11], a pair of

emulsion films hosted in a box placed outside the brick, as interface between the latter and the target tracker. Before detaching the CSD from the brick, they are exposed to an XRay spot, in order to define a common reference system for the two CS and the first emulsion in the brick (with a precision of a few tens of μm). Afterwards the CS are developed and the predictions from target tracker are searched for within a few cm area. If these are confirmed the brick is brought outside the Gran Sasso laboratory and exposed to cosmic ray before development.
The mechanical accuracy obtained during the brick piling is in the range of 50-100 μm. The reconstruction of cosmic rays passing through the whole brick allows to improve the definition of a global reference frame, leading to a precision of 1-2 μm.
All the tracks located in the CSD are subsequently followed inside the brick, starting from the most downstream film, until they stop. Then a general scanning around the stopping point(s) is performed, tracks and vertices are reconstructed, the primary vertex is located and the kinematic analysis defines the event topology.

2.2 The Target Tracker

The main role of the Target Tracker is to provide a trigger and identify the right bricks where the event vertex should be located. Each wall is composed by orthogonal planes of plastic scintillator strips (680 cm $\times$ 2.6 cm $\times$ 1 cm). The strips are made of extruded polystyrene with 2% p-terphenyl and 0.02% POPOP, coated with a thin diffusing white layer of TiO_2. Charged particle crossing the strips will create a blue scintillation light which is collected by wavelength-shifting fibers which propagate light at both extremities of the strip. All fibers are connected at both ends to multianode Hamamatsu PMTs. The detection efficiency of each plane is at 99%. A detailed description of the Target Tracker design can be found in [12]

2.3 The Spectrometer

The spectrometer allows to suppress the background coming from charm production through the identification of wrong-charged muons and contributes to the kinematic reconstruction of the event performed in the target section. The magnet [13] is made of two vertical walls of rectangular cross section and of a top and bottom flux return path. The walls are built lining twelve iron layers (5 cm thickness) interleaved with 2 cm of air gap, allocated for the housing of the Inner Tracker detectors, Resistive Plate Chambers, RPCs. Each iron layer is made of seven slabs, with dimensions $50 \times 1250 \times 8200$ mm^3, precisely milled along the two 1250 mm long sides connected to the return yokes to minimize the air gaps along the magnetic circuit. The slabs are bolted together to increase the compactness and the mechanical stability of the magnet which acts as a base for the emulsion target support. The nuts holding the bolts serve as spacers between two slabs and fix the 20 mm air gap where the RPCs are mounted.

The precision tracker is made of drift tubes planes located in front, behind and between the two magnet walls: in total 12 drift tube planes covering an area of 8 m $\times$ 8 m. The tubes are 8 m long and have an outer diameter of 38 mm. The trackers allows to reconstruct the muon momentum with a resolution $\Delta p/p \leq 0.25$. A particle entering the spectrometer is measured by layers of vertical drift tube planes located before and after the magnet walls. Left-right ambiguities are resolved by the two dimensional measurement of the spectrometer RPCs and by two additional RPC planes, equipped with pickup strips inclined of $\pm 42.6^\circ$ with respect to the horizon (XPC). The Inner Tracker RPCs, eleven planes per spectrometer arm, give a coarse measurement of the tracks and perform pattern recognition and track matching between the precision trackers. The OPERA RPCs [14] are "standard" bakelite RPCs, similar to those used in the LHC experiments: two electrodes, made of 2 mm plastic laminate (HPL) are kept 2 mm apart by means of polycarbonate spacers in a 10 cm lattice configuration. The double coordinate readout is performed by means of copper strip panels. The strip pitch is 3.5 cm for the horizontal

strips and 2.6 cm for the vertical layers. The OPERA RPCs have a rectangular shape, covering an area of about 3.2 m^2. The sensitive area between the iron slabs (8.75×8 m^2), is covered by twenty one RPCs arranged on seven rows, each with three RPCs in a line. In total, 1008 RPCs have been installed in the two spectrometers.

3 Physics performances

The OPERA detector will host 155000 bricks for a total target mass of 1350 tons. The signal of the occurrence of $\nu_\mu \rightarrow \nu_\tau$ oscillation is the charged current interaction of the ν_τ's inside the detector target ($\nu_\tau N \rightarrow \tau^- X$). The reaction is identified by the detection of the τ lepton in the final state through the decay topology and its decay modes into an electron, a muon, and a single or three charged hadrons:

$$\tau^- \rightarrow e^- \nu_\tau \overline{\nu_e} \qquad \tau^- \rightarrow \mu^- \nu_\tau \overline{\nu}_\mu \qquad \tau^- \rightarrow (h^- h^+) h^- \nu_\tau (n\pi^0)$$

The branching ratio for the electronic, muonic and hadronic channel are 17.8%, 17.7% and 64.7% respectively. For the typical τ energies expected with the CNGS spectrum the average decay length is ~ 450 μm.

Neutrino interactions will occur predominantly inside lead plates. Once the τ lepton is produced, it will decay either within the same plate, or further downstream. In the first case, τ decays are detected by measuring the impact parameter of the daughter track with respect to the tracks originating from the primary vertex, while in the second case the kink angle between the charged decay daughter and the parent direction is evaluated.

The τ search sensitivity, calculated for 5 years of data taking with a total number of 45×10^{18} integrated p.o.t. per year, is given in table 1.

Table 1: *Expected number of signal and background events after 5 years of data taking.*

τ decay	Signal $\div \Delta m^2$ (Full mixing)		Background
channels	2.5×10^{-3} (eV^2)	3.0×10^{-3} (eV^2)	
$\tau \rightarrow \mu^-$	2.9	4.2	0.17
$\tau \rightarrow e^-$	3.5	5.0	0.17
$\tau \rightarrow h^-$	3.1	4.4	0.24
$\tau \rightarrow 3h$	0.9	1.3	0.17
ALL	10.4	15.0	0.76

The main background sources are given by large angle scattering of muons produced in $\nu_\mu CC$ interactions, secondary hadronic interaction of daughter particles produced at primary ν_μ interaction vertex and decays of charmed particles produced at primary ν_μ interaction vertex. Comparing the total number of detected ν_τ interaction with the estimated background it's clearly seen that OPERA is quite a background-free experiment. In Figure 2 the ν_τ observation probability at 3 and 4 σ as a function of Δm^2 is reported.

4 Results from the first runs

The first CNGS run was held in August 2006 [15]. At that time only electronic detectors were installed: the brick filling started indeed at the beginning of 2007. From 18 to 30 August 2006 a total intensity of 0.76×10^{18} p.o.t. was integrated and 319 neutrino-induced events were collected (interactions in the rock surrounding the detector, in the spectrometers and in the target walls). Thanks to this first technical run the detector geometry was fixed and the full reconstruction of

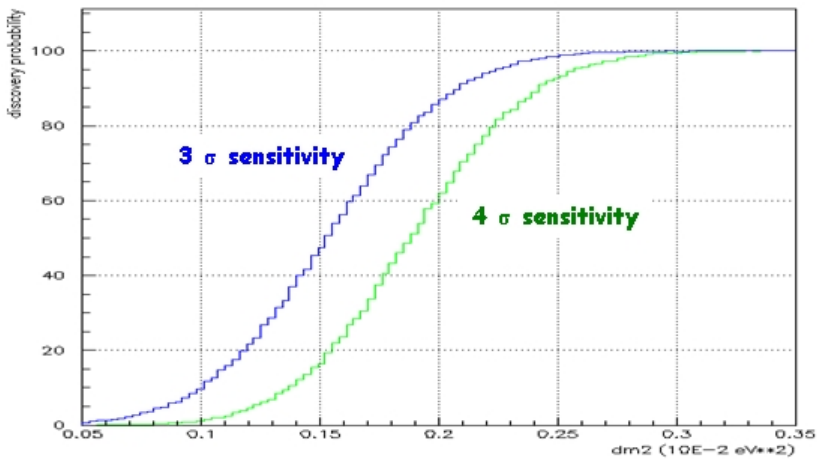

Figure 2: *3 and 4 σ observation probability as a function of Δm^2.*

electronic detectors data tested. It was also possible to fine-tune the synchronization between CERN and Gran Sasso, performed using GPS clocks. Furthermore, the zenith-angle distribution from penetrating muon tracks was reconstructed and the measured mean angle of 3.4 ± 0.3^o was well in agreement with the value of 3.3^o expected for CNGS neutrinos traveling from CERN to the LNGS underground laboratories.

The first OPERA physical run was held in October 2007. At that time about 40% of the target was installed, for a total mass of about 550 tons. In about 4 days of continuous data taking 0.79×10^{18} p.o.t. were produced at CERN and 38 neutrino interactions in the OPERA target were triggered by the electronic detectors. The corresponding bricks indicated by the brick finding algorithm were extracted and developed after the cosmic ray exposure and their emulsions sent to the scanning laboratories. In a few hours the first neutrino interactions of the OPERA experiment were successfully located and reconstructed. In Figure 3 the display of two events is shown. The left one is a ν_μCC interaction with 5 prongs and a shower reconstructed pointing to the primary interaction vertex (γ conversion after a π^o decay). In the second a quite energetic shower (about 4.7 GeV) coming from the primary interaction vertex is visible.

This first physical run was quite short but very significative. Indeed it allowed a full testing of the electronic detectors and the data acquisition. Furthermore, the brick finding algorithm was successfully used to locate the bricks were the neutrino interaction occurred. Finally, the target tracker to brick matching was proved to be able to satisfy the expectations and the full scanning strategy validated.

5 Outlook and future plans

The OPERA target will by completed by May 2008. In June a first 150-day period of CNGS beam at nominal intensity is expected to start. About 30×10^{18} p.o.t. will be integrated, equivalent to about 3500 neutrino interactions. More then 100 charm decays will be collected, so that the capability to reconstruct τ decays will be fully exploited. The corresponding number of expected triggered ν_τ is 1.3: with some luck the first ν_τ candidate event will be observed during the 2008 OPERA run.

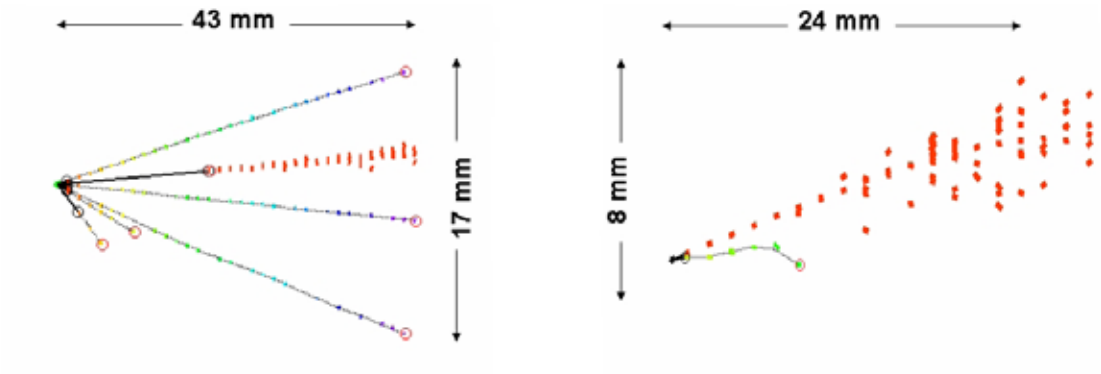

Figure 3: *Two reconstructed neutrino interaction from the OPERA 2007 run. The event displayed on the left is a a ν_μCC interaction. The right side shows an event where an energetic shower comes from the interaction vertex.*

References

1. M. Guler *et al.*, *"An appearance experiment to search for oscillations in the CNGS beam"*, CERN/SPSC 2000-028, SPSC/P318, LNGS P25/2000, Jul. 2000
2. Y. Fukuda *et al.*, *Phys. Rev. Lett.* **81**, 1562 (1998)
3. CNGS project: http://proj-cngs.web.cern.ch/proj-cngs/
   G. Acquispace *at al.*, CERN-98-02 (1998)
   R. Bailey *et al.*, CERN-SL/99-034 (1999)
   A. E. Ball *et al.*, CERN-SL/Note-2000-063 (2000)
4. E. Eskut *et al*, *Nucl. Instrum. Methods* A **401**, 7 (1997)
5. K. Kodama *et al*, *Phys. Lett.* B **504**, 218 (2001)
6. T. Nakano (CHORUS collaboration), *International Europhysics Conference on High-Energy Physics* (HEP 2001), Budapest, Hungary, 12-18 July 2001
7. M. De Serio *et al*, *Nucl. Instrum. Methods* A **554**, 247 (2005)
8. N. Armenise *et al*, *Nucl. Instrum. Methods* A **551**, 261 (2005)
9. K. Borer *et al*, *Nucl. Instrum. Methods* A **566**, 327 (2006)
10. I. Kreslo *et al*, *JINST* **3**, P04006 (2008)
11. A. Anokhina *et al*, submitted to *JINST*
12. T. Adam *et al.*, *Nucl. Instrum. Methods* A **577**, 523 (2007)
13. M. Ambrosio *et al.*, *IEEE Trans. Nucl. Sci.* **51**, 975 (2004)
14. A. Bergnoli *et al.*, *IEEE Trans. Nucl. Sci.* **52**, 2963 (2005)
15. R. Acquafredda *et al.*, OPERA collaboration, *New J.Phys* **8**, 303 (2006)

NEUTRINO OSCILLATIONS, LOW-ENERGY EXCESS, NUMI NEUTRINOS, AND ANTINEUTRINOS IN MINIBOONE

C.C. POLLY
On behalf of the MiniBooNE Collaboration
Indiana University Cyclotron Facility,
2401 Milo B. Sampson Lane, Bloomington, IN–USA.

The MiniBooNE collaboration published initial results from a search for ν_μ to ν_e oscillations in June 2007. While no evidence of ν_e appearance was found in the region of neutrino energies expected from LSND under a standard 2ν mixing hypothesis, a significant excess was observed at lower energies. The results from the oscillation analysis, the excess at low energies, an analysis of neutrino events from the NuMI beamline in the MiniBooNE detector, and the current running in $\overline{\nu}$-mode are discussed.

1 Introduction

The primary motivation of the MiniBooNE experiment at Fermi National Laboratory is to search for the oscillation of neutrinos from ν_μ into ν_e flavors over a short baseline consistent with the mixing parameters found by the LSND experiment [1]. To achieve the required neutrino flux, MiniBooNE extracts 8.89 GeV/c protons directly from the Booster and impacts them on a Be-target at the center of a focusing horn pulsed at 174 kA. The horn was initially operated in a polarity such that positively charged pions were focused to create a ν_μ beam. Ideally the content of the secondary neutrino beam at the detector would be purely ν_μ, however kaons produced at the target as well as muons from the pion decay chain result in an intrinsic ν_e contamination that is 0.5% of the ν_μ flux, and intrinsic $\overline{\nu}_e$ contamination of only 0.05%. At the event level, intrinsic ν_e are indistinguishable from oscillation ν_e, but have an energy distribution that extends to higher energies than that expected for ν_e appearing due to oscillation. The wrong-sign background, i.e. $\overline{\nu}_\mu$ in a ν_μ beam or vice versa, forms 6% of the flux at the detector. The ν-mode fluxes at the detector for all neutrino species are plotted as a function of energy in Figure 1(a). In this mode of operation, the experiment has collected a total of 6.6×10^{20} protons on target (POT), although results in this document and elsewhere have only been presented for 5.7×10^{20} POT.

By switching the polarity of the horn, negatively charged pions are focused to create a predominantly $\overline{\nu}_\mu$ neutrino beam. The K^- production at the target in $\overline{\nu}_\mu$ mode is suppressed relative to the corresponding K^+ in ν-mode, resulting in a reduced intrinsic $\overline{\nu}_e$ contamination of 0.4%. However, at 0.2% the wrong-sign intrinsic ν_e contamination in $\overline{\nu}$-mode is higher than the wrong-sign $\overline{\nu}_e$ component was in ν-mode. Overall the total fraction of intrinsic $\nu_e + \overline{\nu}_e$ contamination remains the same. The primary difference in $\overline{\nu}$-mode relative to ν-mode is that leading particle effects cause the π^- to have softer momenta and higher production angles, thus making it more difficult for the horn to efficiently focus the negative pions. The overall neutrino

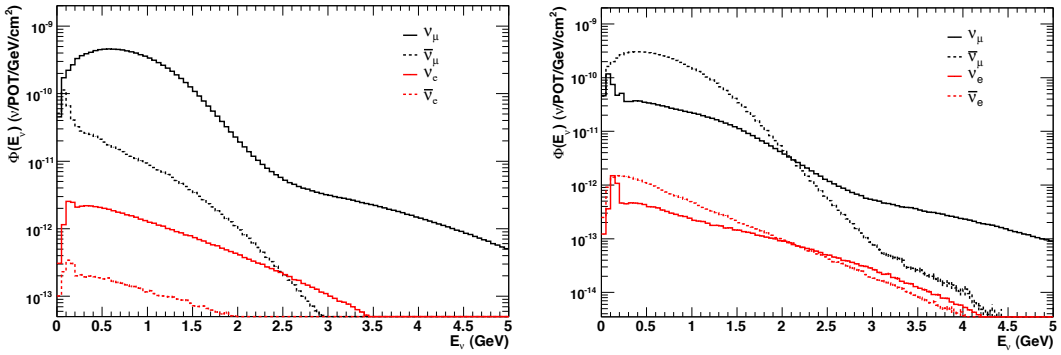

(a) ν-mode flux **(b)** $\overline{\nu}$-mode flux

Figure 1: Total predicted flux at the MiniBooNE detector by neutrino species for (a) neutrino and (b) antineutrino modes.

flux at the detector is reduced by approximately a factor of two in $\overline{\nu}$-mode. In addition to this reduction, the cross-section $\overline{\nu}$ charge-current interactions is smaller than ν resulting in total factor of 4 reduction in the overall rate of neutrino interactions per POT. Another consequence of running in $\overline{\nu}$-mode is that the harder spectrum of the π^+ make them more difficult to defocus. As shown in Figure 1(b), this results in a much larger wrong-sign component where ν_μ now form 16% of the beam in $\overline{\nu}$-mode. As of this writing, the experiment has collected nearly 3.0×10^{20} POT with an eventual goal of reaching a total of 5.0×10^{20} POT over the next year. A complete discussion of the MiniBooNE beamline and the flux prediction has been recently summarized [3] and submitted to PRD.

The average energy of the neutrino beam is 800 MeV, which requires placing the detector at a distance of 0.5 km in order to preserve the L/E of LSND. The detector consists of 800 tons of pure mineral oil contained in a 12 m diameter sphere. The sphere is divided into an inner and outer region via an optical barrier, with the outer region serving as an active veto lined with 240 8 in photomultiplier tubes (PMTs). The inner region contains 1280 inward-facing PMTs. Although the optical barrier is at a radius of 540 cm, most analyses require events to be contained and the reconstructed vertices to fall within a sphere of radius ≈ 500 cm. A more complete description of the detector has been recently submitted to NIM and can be found on the archive [4].

The fundamental strength of the detector lies in the ability to separate ν_e-CCQE signal events with an e in the final state from ν_μ-CCQE events that produce a μ. It is also necessary to resolve when two electromagnetic particles are created in order to separate NC-π^0 interactions where the pion immediately decays, $\pi^0 \rightarrow \gamma\gamma$. Since pure mineral oil is used, the detector is mainly a Cerenkov-type detector, where particle ID is performed through analysis of the multiplicity and topology of rings projected on the outer wall of the detector. However, despite being very pure, high quality Marcol 7 mineral oil, impurities result in some scintillation light. A Michel e from ν_μ decay will typically have 75% of its light contained in the prompt Cerenkov ring, while another 25% is emitted isotropically with a dominant time constant of 34 ns. The upside is that it means the detector can also be used to detect pure NC events where no particles are relativistic enough to emit a Cerenkov cone. The downside is that the optical model is a very complex system where the modeling of the light production and propagation must account for Cerenkov flux, scintillation flux, absorption and readmission of light (fluorescence), Raman and Rayleigh scattering, reflections, along with the PMT response. A satisfactory set of parameters for the optical model, several of which are wavelength dependent, were obtained through a combination of benchtop tests and *in situ* calibrations.

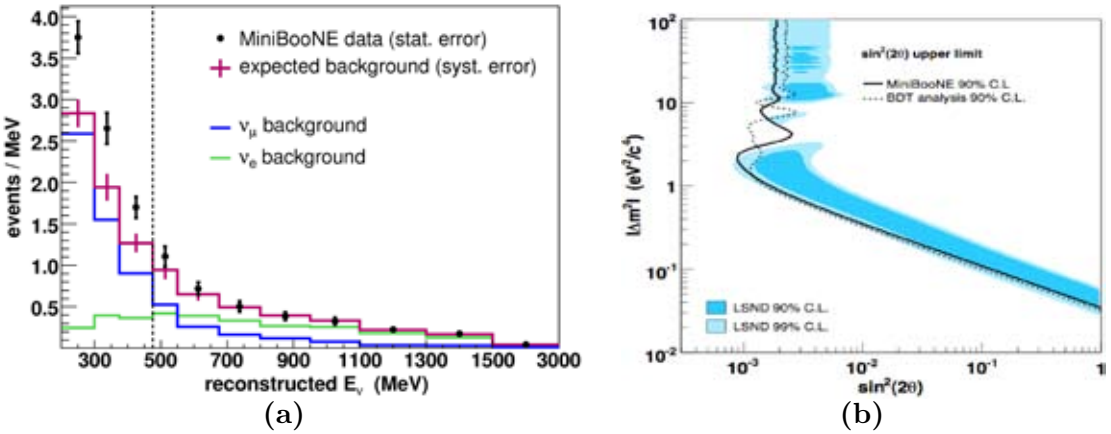

Figure 2: (a) The reconstructed energy spectrum for events passing ν_e-like cuts in the TBL analysis, and (b) the resulting 90% CL exclusion curve when fitting above the analysis threshold of 475 MeV. Also, shown in (b) is the limit curve resulting from a fit to energies about 300 MeV in the BDT analysis.

2 The Oscillation Result and the Low Energy Excess

The basics of the oscillation analysis have been described in the original oscillation result paper[2]. The steps involve calibrating the raw PMT data, passing both data and Monte Carlo through event reconstruction, developing a robust particle ID for extracting the ν_e-CCQE candidates, applying constraints arising from the well-measured ν_μ-CCQE and NC-π^0 samples[5,6], and then performing a χ^2 minimization under a full systematic error covariance matrix.

The analysis was divided into two quasi-independent analyses, referred to as the boosted-decision tree (BDT) and the track-based likelihood (TBL). Both analyses relied on the same underlying Monte Carlo samples to form their background prediction. As such they share identical sources of systematic errors stemming from underlying uncertainties in the flux prediction, understanding of cross-sections in the 1 GeV range, and optical modeling. They diverged starting at the reconstruction stage where the TBL analysis used a more sophisticated (and consequently CPU intensive) set of algorithms. The TBL analysis then constructed a set of maximum likelihoods under the fit hypotheses that the final state consisted of a single e, ν_μ, or π^0. In addition to the basic pre-cuts shared by both analyses, the TBL analysis formed particle ID cuts using these likelihoods and the reconstructed pion mass. By comparison the BDT analysis used a much faster reconstruction algorithm, constructed a large sample of macroscopic variables, and then input ≈ 170 of these quantities into a boosted-decision tree to form a single variable as its PID cut. When tested on the Monte Carlo, the BDT analysis had a larger signal-to-background ratio than the TBL. However, when a systematic error analysis was performed by running 1000s of underlying Monte Carlo worlds with changes in the underlying model parameters, the response of the BDT analysis showed a higher sensitivity to systematic errors, which marginally outweighed any gains in signal-to-background. In a predefined procedure, the analysis with the better ultimate sensitivity, TBL, was quoted as the final experimental result, with the BDT serving as a very powerful cross-check. Neither analysis saw an excess of ν_e events in the region of reconstructed E_ν above 475MeV where and LSND-like would have appeared under a 2ν mixing hypothesis. The resulting limit curves for both analyses are shown in Figure 2(b), with the TBL ν_e spectrum shown in Figure 2(a). The analyses were comparable enough in sensitivity that after the unblinding, a downward fluctuation in the BDT data set resulted in the limit curve actually being a little better than the TBL analysis at low Δm^2.

Below the oscillation analysis region, a 3.4 σ excess of 96 ± 28 events was observed in the 300-475 MeV region. Many consistency checks have been performed on the events in that region

to verify that they do not exhibit undue pathologies. The x, y, z, and r distributions are consistent with neutrino interactions spatially distributed throughtout the the detector, the events are uniformly distributed in time throughout the duration of the run, and perhaps most importantly, a visual inspection of the event displays for events in the low energy region confirms all of the events exhibit the characteristics expected of a single ring from an electromagnetic shower. It should be noted that ring originating from a single e or a single γ are indistinguishable. Since the initial publication of the low energy result, the existing analysis was pushed down in threshold to include a bin in the 200-300 MeV range. The excess in this region is similar in significance at 91 ± 31 events, although the highly correlated systematic error at low energies precludes a simple quadrature sum of the overall significance.

In addition to performing consistency checks and extending the analysis to lower energies, a full reevaluation of all of the backgrounds and associated systematic errors was undertaken. The results are expected to be presented in a paper to be published later in the year and will include:

- Photonuclear disintegration which was absent from GEANT3, and can create a background if one of the γs in a NC-π^0 event is lost.
- More comprehensive hadronic errors, particularly in the final states after a photonuclear event occurs.
- Better handling of beam π^+ uncertainties with errors propagated directly from meson production errors.
- Improved measurement of neutrino-induced π^0 with finer momentum binning.
- Internal MiniBooNE measurement of the coherent/resonant π^0 fraction.
- Refined cuts that efficiently remove backgrounds coming from ν interactions in the dirt surrounding the detector.
- Extra ν-mode data acquired since the initial publication, 16% increase in statistics.
- A comprehensive review of how the radiative Δ decay rate is extracted from the measured π^0 rate.

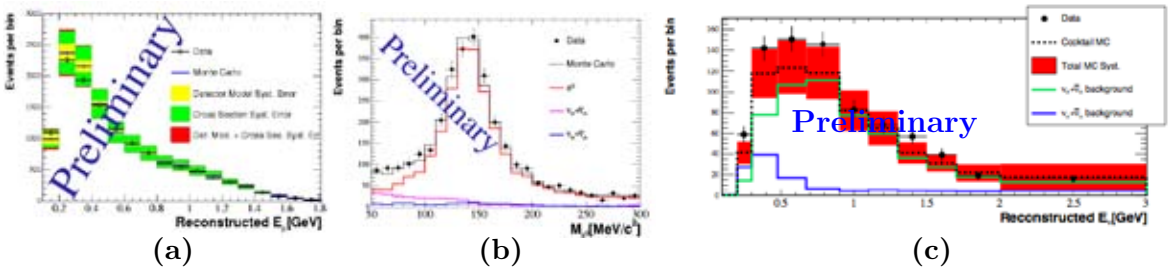

Figure 3: Preliminary data to Monte Carlo comparisons for events in the MiniBooNE detector coming from the NuMI beamline. Cuts have been applied to isolate (a) ν_μ-CCQE, (b) NC-π^0, and (c) ν_e-CCQE like samples.

3 Events in MiniBooNE from the NuMI Beamline

The MiniBooNE detector is positioned 110 mrad off-axis from the NuMI beamline that delivers neutrinos to the MINOS experiment. By comparison, the off-axis angle in T2K is 35 mrad and NOVA is somewhat smaller at 14.5 mrad, however, even at 110 mrad MiniBooNE still sees a

significant flux of neutrinos from NuMI. Since the NuMI and BooNE neutrinos are produced in independent spills, there is no confusion about which beam the neutrino events originate from and a dedicated NuMI trigger can easily be established. At the large off-axis angle, neutrinos in MiniBooNE from the NuMI beamline have a similar average energy as the normal Booster neutrino beam. The distance from the NuMI target to the MB detector is a little larger, so the overall L/E is about 1.4 times larger. The largest difference in the neutrino flux coming from the NuMI beam is in the amount of intrinsic ν_e contamination, which at 5% is an order of magnitude higher than in the Booster neutrino beam.

A track-based analysis with very similar cuts to the official TBL analysis has been performed on the NuMI events. The preliminary results are shown in Figure 3. The agreement in the ν_μ-CCQE and NC-π^0 samples is very good, which validates both the flux prediction from the NuMI beamline and the response of the MiniBooNE detector. The ν_e-CCQE sample shows an excess in the region from 200-900 MeV. However, the large correlated systematic error results in a statistical significance of only 1.3σ.

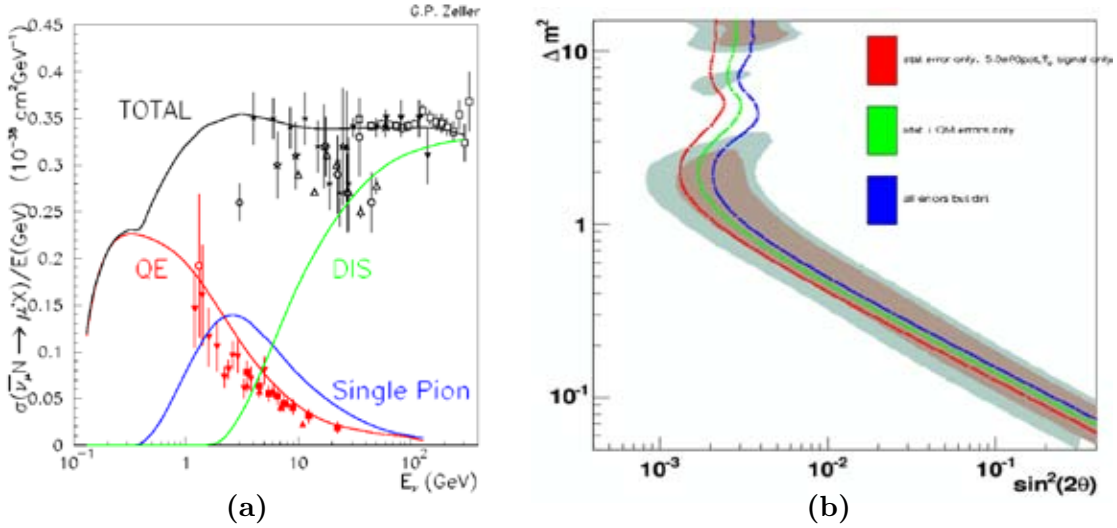

Figure 4: (a) World data for $\overline{\nu}$ cross-sections in charged-current processes, and (b) the projected sensitivity to $\overline{\nu}_e$ appearance for 5×10^{20} POT delivered in $\overline{\nu}$-mode.

4 Running in $\overline{\nu}$-mode

Currently MiniBooNE is running in $\overline{\nu}$-mode in order to check for $\overline{\nu}_\mu$ oscillating into $\overline{\nu}_e$. However, due to the considerations discussed in Section 1, the lower neutrino rate will reduce the sensitivity relative to the same POT delivered in ν-mode, see Figure 4(b). Preliminary projections for sensitivities with errors ranging from statistics-only to a nearly full systematic error treatment are shown. Since the LSND experiment used a $\overline{\nu}_\mu$ beam, this will provide a more direct but less sensitive check of the LSND signal.

In addition to $\overline{\nu}$ oscillations, current knowledge of antineutrino cross-sections at energies below 1 GeV is limited, see Figure 4(a). MiniBooNE will be able to provide measurements of various exclusive NC and CC channels. Absolute measurements will be limited by a flux uncertainty that is currently 15%, however, measuring $\nu/\overline{\nu}$ ratios should have smaller errors and could prove to be very useful for experiments like T2K where the beam will also be operated in both modes with neutrinos of a similar energy.

Finally, valuable information about the low energy excess will be revealed since several of the potential explanations, including anomaly-mediated photons or new gauge bosons presented

elsewhere in these proceedings, make distinct predictions for how the excess should extrapolate to a $\overline{\nu}_\mu$ beam.

References

1. A. Aguilar *et al.* [LSND Collaboration], Phys. Rev. D **64**, 112007 (2001) [arXiv:hep-ex/0104049].
2. A. A. Aguilar-Arevalo *et al.* [MiniBooNE Collaboration], Phys. Rev. Lett. **98**, 231801 (2007) [arXiv:0704.1500 [hep-ex]].
3. A. A. Aguilar-Arevalo *et al.* [MiniBooNE Collaboration], arXiv:0806.1449 [hep-ex].
4. A. A. Aguilar-Arevalo *et al.* [MiniBooNE Collaboration], arXiv:0806.4201 [hep-ex].
5. A. A. Aguilar-Arevalo *et al.* [MiniBooNE Collaboration], Phys. Rev. Lett. **100**, 032301 (2008) [arXiv:0706.0926 [hep-ex]].
6. A. A. Aguilar-Arevalo *et al.* [MiniBooNE Collaboration], Phys. Lett. B 664, **41** (2008) [arXiv:0803.3423 [hep-ex]].

SOME NEW IMPLICATIONS OF THE ANOMALOUS BARYON CURRENT IN THE STANDARD MODEL

RICHARD. J. HILL
Fermi National Accelerator Laboratory
P.O. Box 500, Batavia, Illinois 60510, USA

Phenomenological implications of the anomalous baryon current in the Standard Model are discussed, in particular neutrino-photon interactions at finite baryon density. A pedagogical derivation of the baryon current anomaly is given.

1 Introduction

The baryon current in the Standard Model is not conserved in the presence of electroweak gauge fields. Although classically we have

$$\partial_\mu J^\mu = \partial_\mu \left(\frac{1}{3} \sum_q \bar{q} \gamma^\mu q \right) = 0 \,, \tag{1}$$

the baryon current divergence acquires quantum corrections when gauge fields are coupled differently to left- and right-handed quarks. For the Standard Model electroweak gauge fields, we have [1]

$$\partial_\mu J^\mu = -\frac{1}{64\pi^2} \epsilon^{\mu\nu\rho\sigma} \left(g_2^2 F^a_{\mu\nu} F^a_{\rho\sigma} - g_1^2 F^Y_{\mu\nu} F^Y_{\rho\sigma} \right) \neq 0 \,, \tag{2}$$

where $F^a_{\mu\nu} = \partial_\mu W^a_\mu - \partial_\nu W^a_\mu + g_2 \epsilon^{abc} W^b_\mu W^c_\nu$ is the covariant $SU(2)_L$ field strength and $F^Y_{\mu\nu}$ is the weak hypercharge field strength. This curious fact may have profound cosmological implications through the generation of baryon number at the electroweak phase transition [2].

As discussed in Refs. [3,4] and reviewed in this talk, nonconservation of baryon number is connected to novel effects that can be observed in laboratory experiments, and that may have interesting astrophysical implications. This report begins with a theoretical review by analyzing the baryon number anomaly in analogy to the perhaps more familiar axial anomaly. Turning to

phenomenology, some observable consequences in neutrino scattering experiments are described, and several other directions to explore are mentioned.

2 Theoretical excursion

2.1 The axial current anomaly and $\pi^0 \to \gamma\gamma$

A famous implication of gauge anomalies is the necessity for a nonzero $\pi^0 \to \gamma\gamma$ amplitude due to the nonconservation of the iso-triplet axial-vector quark current,

$$J^{5\mu} = \frac{1}{2}(\bar{u}\gamma^\mu\gamma_5 u - \bar{d}\gamma^\mu\gamma_5 d)\,. \tag{3}$$

In the presence of electromagnetism we have [6,7]

$$\partial_\mu J^{5\mu} = \frac{e^2}{32\pi^2}\epsilon^{\mu\nu\rho\sigma}F_{\mu\nu}F_{\rho\sigma}\,. \tag{4}$$

If low-energy QCD is described by a theory of mesons, a nonzero $\pi^0 \to \gamma\gamma$ amplitude is necessary in order to reproduce this result.

Let us recall how this works explicitly, by considering the object:

$$\int d^4x\, e^{-iq\cdot x}\langle\gamma(p)\gamma(k)|J^{5\mu}(x)|0\rangle \equiv \Big[B_5(q,\mu)$$

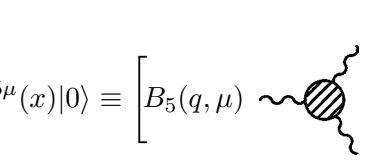

$$\Big] \times \epsilon^*_\nu(p)\epsilon^*_\rho(k)(2\pi)^4\delta^4(p+k-q)\,, \tag{5}$$

first at the quark level, and then at the meson level. The field B_5 denotes a background field coupled to $J^{5\mu}$, and A is the photon. At the quark level, after a proper definition of the relevant triangle diagram that ensures vector current conservation, a standard calculation [11] shows that in lowest order perturbation theory,

$$iq_\mu\Big[\quad B_5$$

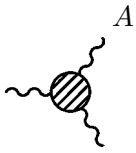

$$\Big] = \frac{e^2}{4\pi^2}\epsilon^{\nu\rho\alpha\beta}p_\alpha k_\beta\,, \tag{6}$$

consistent with (4). How is this result reproduced in terms of the low-energy effective action where the quarks are replaced by mesons? First, there is no gauge invariant operator connecting B_5 and two photons directly, so that

$$B_5$$

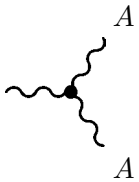

$$= 0\,. \tag{7}$$

A nonzero contribution is however obtained from the pion pole (consider the limit of vanishing quark masses),

$$B_5$$

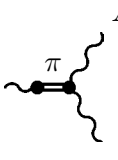

$$= -iC_1 q^\mu \times \frac{i}{q^2} \times (-iC_2)\frac{e^2}{4\pi^2}\epsilon^{\nu\rho\alpha\beta}p_\alpha k_\beta\,. \tag{8}$$

Here C_1 denotes the strength of the π coupling to the axial current, and C_2 is the strength of the pion-photon vertex. From the chiral lagrangian with Wess-Zumino-Witten term [9,10], we necessarily have $C_1 = f_\pi$, $C_2 = 1/f_\pi$. Contracting (8) with iq_μ reproduces (6) and hence (4). Phrased differently, if low-energy QCD is described by an effective theory of pions, then the process $\pi^0 \to \gamma\gamma$ occurs with a fixed strength.

2.2 The baryon current anomaly

The anomalous baryon current can be treated in close analogy to the anomalous axial-vector current above. We must however pay close attention to which currents are conserved, since in the present case it is no longer true that "vector currents are conserved, axial-vector currents are anomalous," as the usual intuition suggests. Suppose that we introduce a background field B_μ coupled to baryon number. Then the baryon current is defined by varying the action with respect to B_μ:

$$J^\mu = \frac{\delta S}{\delta B_\mu}\,, \tag{9}$$

and its divergence is read off from

$$\delta S = -\int d^4x\, \epsilon(x)\, \partial_\mu J^\mu\,, \tag{10}$$

where $\delta B_\mu = \partial_\mu \epsilon$. Thus the problem of calculating the anomalous divergence of the baryon current is reduced to the introduction of B_μ.

However, we must not be too naive in introducing B_μ; otherwise we may start with a gauge invariant theory, but end up with a non-gauge-invariant (i.e., nonsensical) theory. Varying the nonsensical theory would not give the correct symmetry current and its divergence. To be explicit, let us return to the example of the axial-vector current for a single fermion, and suppose that we add the perturbation

$$\bar\psi(i\partial\!\!\!/ + A\!\!\!/)\psi \to \bar\psi(i\partial\!\!\!/ + A\!\!\!/ + B\!\!\!/\gamma_5)\psi\,. \tag{11}$$

Then the theory naively remains invariant under electromagnetic gauge transformations,

$$\psi \to e^{i\epsilon}\psi\,, \quad A_\mu \to A_\mu + \partial_\mu\epsilon\,, \quad B_{5\mu} \to B_{5\mu}\,. \tag{12}$$

However, due to the effects of anomalies [a] the theory is in fact not gauge invariant. For a sensible theory, we must add at the same time as the perturbation (11), a counterterm:

$$\bar\psi(i\partial\!\!\!/ + A\!\!\!/)\psi \to \bar\psi(i\partial\!\!\!/ + A\!\!\!/ + B\!\!\!/\gamma_5)\psi + \mathcal{L}_{\rm ct}(A, B_5)\,, \tag{13}$$

where explicitly,

$$\mathcal{L}_{\rm ct}(A, B_5) = \frac{1}{6\pi^2}\epsilon^{\mu\nu\rho\sigma} B_\mu A_\nu \partial_\rho A_\sigma\,. \tag{14}$$

The results (4) and (6) have an implicit dependence on the choice of counterterm. [b] In particular, the "Bardeen" [8] form of the counterterm, of which (14) is an example, is employed to conserve vector currents in the presence of arbitrary background fields.

When nonvectorlike currents are gauged, a different counterterm must be employed. For the general case the explicit counterterm is given in Ref. [4]. Let us consider the baryon current for a single standard model generation, and for simplicity restrict attention to the neutral gauge bosons A and Z. The Bardeen counterterm is then

$$\mathcal{L}_{\rm Bardeen} = \frac{e g_2}{24\pi^2 \cos\theta_W}\epsilon^{\mu\nu\rho\sigma}(B_\mu Z_\nu \partial_\rho A_\sigma + A_\mu Z_\nu \partial_\rho B_\sigma)\,, \tag{15}$$

[a] That is, due to the effects of the fermion measure, in path integral language.

[b] The dependence can be made explicit by performing the calculation with Weyl fermions.

whereas the full counterterm is

$$\mathcal{L}_{\rm ct} = \frac{eg_2}{24\pi^2 c_W}\epsilon^{\mu\nu\rho\sigma}(-2B_\mu Z_\nu \partial_\rho A_\sigma + A_\mu Z_\nu \partial_\rho B_\sigma)\,. \tag{16}$$

If we now write

$$S = [S + S_{\rm Bardeen} - S_{\rm ct}] + S_{\rm ct} - S_{\rm Bardeen}\,, \tag{17}$$

then the variation (10) vanishes for the bracketed combination in (17), and from the remainder we can read off immediately using (15) and (16):

$$\partial_\mu J^\mu = -\frac{eg_2}{8\pi^2\cos\theta_W}\epsilon^{\mu\nu\rho\sigma}\partial_\mu A_\nu \partial_\rho Z_\sigma\,, \tag{18}$$

yielding the result (2).

In the language of chiral lagrangians, the new counterterm has the novel property that it leaves residual "pseudo-Chern Simons" terms in the action, i.e., terms involving the epsilon tensor, but having no pion fields. Such terms are subtracted if the Bardeen counterterm is used instead, since it can be shown that $\mathcal{L}_{\rm Bardeen} = -\mathcal{L}(\pi = 0)$. Equivalently, the counterterm requires a different boundary condition for "integrating the anomaly" to obtain the anomalous part of the chiral lagrangian [9]; this is again related to the statement that $\mathcal{L}(\pi = 0) \neq 0$.

2.3 Vector mesons

The preceding discussion shows how to incorporate spin-1 background fields into the chiral lagrangian without upsetting gauge invariance in the fundamental gauge fields. In particular, the $SU(2)_L \times U(1)_Y$ gauge anomaly cancellation between quark and lepton sectors is not upset when background fields are coupled to the quark flavor symmetries. With these background field probes in place, it is straightforward to derive properly defined (covariant) currents and the associated anomalous divergences, by an appropriate variation of the action.

The relevance of the background field discussion for vector mesons is twofold. First, since physical spin-1 mesons such as ρ and ω behave mathematically like these background fields, we have found the "slots" which these fields fit into when constructing our chiral lagrangian. Second, and relatedly, once we know that the vector mesons inhabit these slots, we find new physical effects related to the quark level anomalies, e.g. to the baryon current anomaly, These effects can be observed experimentally. For example, at the level of vector meson dominance, new effects will be described by the interaction

$$\mathcal{L} = \frac{eg_2}{8\pi^2\cos\theta_W}\epsilon^{\mu\nu\rho\sigma}\omega_\mu Z_\nu \partial_\rho A_\sigma\,. \tag{19}$$

This is in the same spirit as using $\pi^0 \to \gamma\gamma$ as a probe of the axial current anomaly.

The theoretical description can be refined at low energy by integrating out the vector mesons; the vector dominance assumption then translates into a prediction for the coefficients of certain $1/m_\omega^2$ suppressed operators.

3 Phenomenology

To see that the vector mesons are indeed described as part of the WZW term structure, we can verify that the same coupling strength is observed in accessible decay modes, such as $\omega \to 3\pi$ and $\omega \to \pi\gamma$. As depicted in the Fig. 1, these are all parts of the baryon current, expressed in terms of the fields, including nuclear sources, in the low-energy chiral lagrangian:

$$J^\mu = \bar{N}\gamma^\mu N + \frac{1}{4\pi^2}\epsilon^{\mu\nu\rho\sigma}\left(-\frac{2i}{f_\pi^3}\partial_\nu\pi^+\partial_\rho\pi^-\partial_\sigma\pi^0 - \frac{e}{f_\pi}\partial_\nu\pi^0\partial_\rho A_\sigma + \frac{eg_2}{2\cos\theta_W}Z_\nu\partial_\rho A_\sigma + \ldots\right)\,. \tag{20}$$

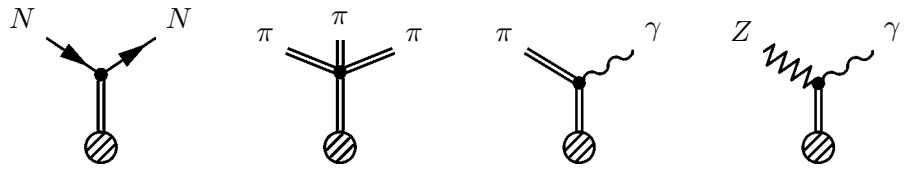

Figure 1: Different parts of the baryon current. The bottom leg denotes a field such as ω coupling to this current, and the blob denotes a source of baryon number, such as a nucleus.

For example,

$$\Gamma(\omega \to \pi\gamma) \approx \frac{3\alpha E_\gamma^3}{64\pi^4 f_\pi^2}\left(\frac{2}{3}g_\omega\right)^2 \approx 0.76\,\mathrm{MeV}\left(\frac{\frac{2}{3}g_\omega}{6}\right)^2 . \tag{21}$$

Similarly, $\frac{2}{3}g_\omega \approx 6$ is obtained for $\omega \to 3\pi$, including the $\omega \to \rho\pi \to 3\pi$ contributions. [c] A consistent, although somewhat uncertain, value of the ω coupling to the baryon current is also obtained for the first diagram in Fig. 1, using one-meson exchange models of the force between nucleons, and isolating the isoscalar $J^P = 1^-$ channel [12]. The effective coupling is expected to be somewhat larger in this case, since "ω" is actually representing a tower of resonances.

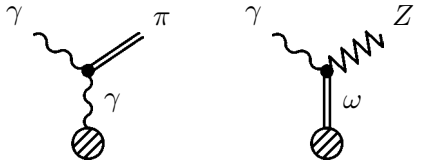

Figure 2: Analogy to the Primakoff effect: on the left, one of the photons in the $\pi\gamma\gamma$ vertex couples to electric charge; on the right, ω from the $\omega Z\gamma$ vertex couples to baryon number.

We wish to access the final diagram in Fig. 1, i.e., the pure gauge field part of the baryon current, that is most directly related to the baryon current anomaly. We expect ω to couple to this part of the current with the same strength as the other parts. Now, if the Z mass were small, [d] the Standard Model would predict a decay mode,

$$\Gamma(\omega \to Z\gamma) = \frac{3\alpha}{256\pi^4}\frac{E_\gamma^3}{m_Z^2}\frac{g_2^2}{\cos^2\theta_W}\left(\frac{2}{3}g_\omega\right)^2\left(1+\frac{m_Z^2}{m_\omega^2}\right) . \tag{22}$$

Of course, the decay $\omega \to Z\gamma$ is not physically allowed. Nevertheless, processes involving virtual Z^* are allowed, and can lead to interesting effects. Since there will be a weak suppression, we should focus on situations in which the Z is "useful", e.g. processes involving neutrinos or parity violation. We can also make the ω "useful", e.g., by utilizing its strong coupling to baryon number to look for enhanced rates when scattering off nuclei, rather than searching for the tiny branching fraction $\omega \to \gamma\nu\bar{\nu}$. As depicted in Fig 2, this is in analogy to probing the $\pi^0\gamma\gamma$ coupling via the Primakoff effect, where one of the photons couples coherently to the electric charge of the nucleus.

3.1 Neutrino scattering

The interaction (19) will induce neutrino-photon interactions in the presence of baryon number. For example, single photons are produced in neutrino-nucleus scattering, as depicted in Fig. 3.

[c] Note that $g_\omega = \frac{3}{2}g'$ in the conventions of Ref. [3,4].

[d] Consider the limit $m_{u,d} \to 0$, $g_2 \to 0$ with v fixed, so that $m_\pi^2 \ll m_Z^2 \ll m_\omega^2$. Then the Z will eat mostly Higgs field, and effects of $\pi - Z$ mixing can be ignored.

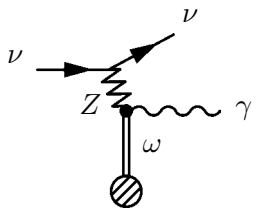

Figure 3: Photon production in neutrino scattering in the presence of baryon number.

In the approximation where the nuclear interactions are described by one-meson exchange, there will be competing contributions from virtual π^0 and ρ^0 exchange. However, π^0 exchange is suppressed by the accidental smallness of $1 - 4\sin^2\theta_W$ in the Standard Model, and the ρ^0 exchange diagram is suppressed in amplitude by $\sim (1+1-1)^2/(1+1+1)^2 = 1/9$ relative to ω, due to the fact that ω is isoscalar, whereas ω is isotriplet; this can be thougth of as a coherence effect at the nucleon level. Further enhancement of the ω exchange due to coherence over adjacent nucleons can occur in kinematics where small enough momentum is exchanged with the nucleus.

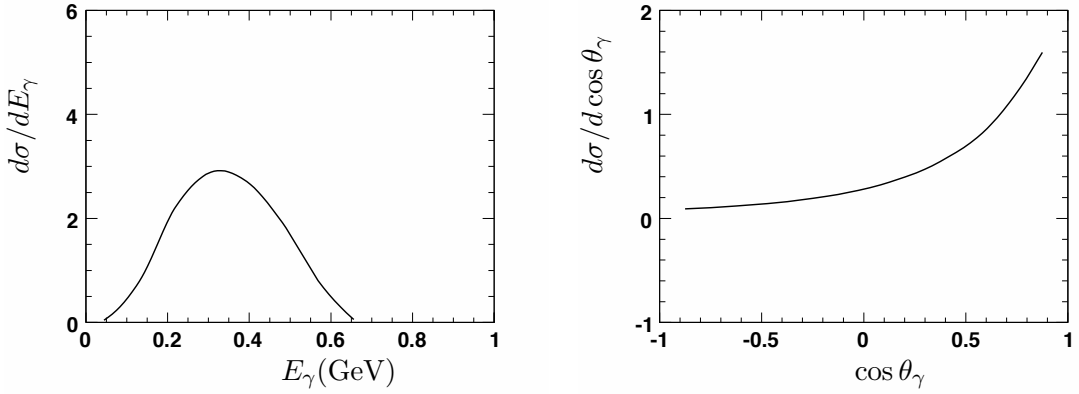

Figure 4: Photon energy distribution (left figure) and angular distribution (right figure), including nuclear recoil and $\omega(780)$ form factor, for 700 MeV neutrino incident on stationary nucleon (arbitrary normalization).

Neglecting effects such as coherence, form factors and recoil, the cross section for the process depicted in Fig. 3 for scattering off an isolated nucleon is [3]

$$\sigma \approx \frac{\alpha g_\omega^4 G_F^2}{480\pi^6 m_\omega^4} E_\nu^6 \approx 2.2 \times 10^{-41} (E_\nu/1\,\mathrm{GeV})^6 (g_\omega/10)^4\,\mathrm{cm}^2\,. \tag{23}$$

The photon energy distribution in this approximation is

$$\frac{d\sigma}{dE_\gamma} \propto E_\gamma^3 (E_\nu - E_\gamma)^2\,, \tag{24}$$

and the angular distributions is flat,

$$\frac{d\sigma}{d\cos\theta_\gamma} \propto \mathrm{constant}\,. \tag{25}$$

Form factors will suppress the cross section at large momentum exchange, pulling the angular distribution forward. As an illustration, the photon energy and angular distribution for a 700 MeV neutrino incident on an isolated nucleon, including nuclear recoil and the form factor

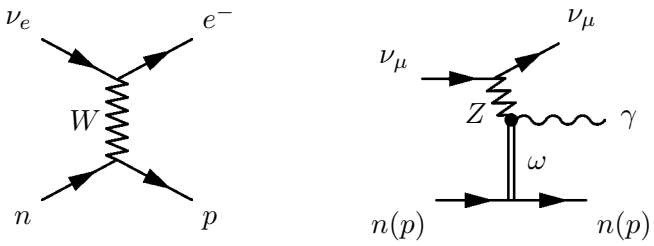

Figure 5: Photon showers from the anomaly-mediated neutral-current process (right), can be mistaken for electron showers from the charged current process (left). On the right, the nucleon can be either neutron or proton.

induced by $\omega(780)$ exchange, is depicted in Fig. 4. A more detailed analysis of single photon events will be presented elsewhere [5].

In the absence of large coherent enhancements, e.g. for scattering on small nuclei, we should ideally use relatively large incident neutrino energies, in order to overcome the mass of ω. Also, if it is not possible to distinguish photon showers from electron showers, a pure ν_μ beam should be used in order to avoid a background from charged-current scatters, $\nu_e + n \to e^- + p$. In fact, these requirements have overlap with experiments looking for ν_e appearance in a ν_μ beam. For example, MiniBooNE [13] and (in the future) T2K [14] have ν_μ beams with energy spectra of order several hundreds of MeV, but primarily $\lesssim 1\,\mathrm{GeV}$, largely within the range of a chiral lagrangian description. Single photons that are mistaken for electrons are a background to ν_e appearance searches, as depicted in Fig. 5. It is interesting that an excess of events observed by MiniBooNE is in the same order of magnitude as predicted by (23), and has similar characteristics to the distributions in Fig. 4. Experiments with higher energy neutrinos are also of interest, but pass beyond a simple chiral lagrangian description.

3.2 Neutrino pair production

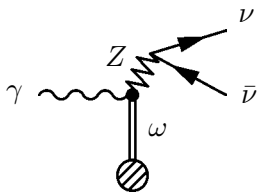

Figure 6: Photon conversion into neutrino pairs in the presence of baryon number.

Similar interactions can give rise to photon conversion into neutrino pairs in the presence of baryon number, as depicted in Fig. 6. A nonnegligible contribution to neutron star cooling via this mechanism was computed in Ref. [3]. Similar effects will occur in the hot and dense environment of a supernova core.

3.3 Parity violation

Besides neutrino interactions, we can use the Z to mediate parity violation. The interaction (19) will give rise to potentially interesting effects in various parity-violating observables. These will be investigated elsewhere [5].

4 Summary

This report began with a pedagogical derivation of the baryon current anomaly in the Standard Model. The counterterm structure in this derivation is interesting because it requires residual "pseudo-Chern-Simons" terms in the action when background vector fields are coupled to the

quark flavor symmetries. This exercise is significant for phenomenology because the same framework can be used to describe vector meson interactions in vector dominance approximation. The resulting extension of the QCD chiral lagrangian provides a useful guide to new effects, such as "baryon-catalyzed" neutrino-photon interactions and parity violation. Other applications of the formalism that have not been discussed here include a description of "natural parity violating" [e] QCD vector meson decays, such as $f_1 \to \rho\gamma$. It is also interesting to relate this framework to five-dimensional descriptions of QCD [15], both as a means of constraining "AdS-QCD" models, and potentially using such models to predict undetermined constants appearing in the chiral lagrangian.

Acknowledgments

The results reported here are based on Refs. [3,4] in collaboration with C.T. Hill and J.A. Harvey. Research supported by the U.S. Department of Energy grant DE-AC02-76CHO3000.

References

1. G. 't Hooft, Phys. Rev. Lett. **37**, 8 (1976). G. 't Hooft, Phys. Rev. D **14**, 3432 (1976) [Erratum-ibid. D **18**, 2199 (1978)].
2. V. A. Kuzmin, V. A. Rubakov and M. E. Shaposhnikov, Phys. Lett. B **155**, 36 (1985). N. S. Manton, Phys. Rev. D **28**, 2019 (1983). F. R. Klinkhamer and N. S. Manton, Phys. Rev. D **30**, 2212 (1984). P. Arnold and L. D. McLerran, Phys. Rev. D **36**, 581 (1987).
3. J. A. Harvey, C. T. Hill and R. J. Hill, Phys. Rev. Lett. **99**, 261601 (2007) [arXiv:0708.1281 [hep-ph]].
4. J. A. Harvey, C. T. Hill and R. J. Hill, Phys. Rev. D **77**, 085017 (2008) [arXiv:0712.1230 [hep-th]].
5. J. A. Harvey, C. T. Hill and R. J. Hill, work in progress.
6. J. S. Bell and R. Jackiw, Nuovo Cim. A **60**, 47 (1969).
7. S. L. Adler, Phys. Rev. **177**, 2426 (1969).
8. W. A. Bardeen, Phys. Rev. **184**, 1848 (1969).
9. J. Wess and B. Zumino, Phys. Lett. B **37**, 95 (1971).
10. E. Witten, Nucl. Phys. B **223**, 422 (1983).
11. See e.g. M. E. Peskin and D. V. Schroeder, *Reading, USA: Addison-Wesley (1995) 842 p*
12. R. Machleidt, K. Holinde and C. Elster, Phys. Rept. **149**, 1 (1987).
13. A. A. Aguilar-Arevalo *et al.* [The MiniBooNE Collaboration], Phys. Rev. Lett. **98**, 231801 (2007) [arXiv:0704.1500 [hep-ex]].
14. Y. Itow *et al.* [The T2K Collaboration], arXiv:hep-ex/0106019.
15. T. Sakai and S. Sugimoto, Prog. Theor. Phys. **113**, 843 (2005) [arXiv:hep-th/0412141]. J. Erlich, E. Katz, D. T. Son and M. A. Stephanov, Phys. Rev. Lett. **95**, 261602 (2005) [arXiv:hep-ph/0501128]. L. Da Rold and A. Pomarol, Nucl. Phys. B **721**, 79 (2005) [arXiv:hep-ph/0501218]. S. K. Domokos and J. A. Harvey, Phys. Rev. Lett. **99**, 141602 (2007) [arXiv:0704.1604 [hep-ph]].

THE LSND PUZZLE IN THE LIGHT OF MINIBOONE RESULTS

THOMAS SCHWETZ
Physics Department, Theory Division, CERN, CH–1211 Geneva 23, Switzerland

I give a brief overview over various attempts to reconcile the LSND evidence for oscillations with all other global neutrino data, including the results from MiniBooNE. I discuss the status of oscillation schemes with one or more sterile neutrinos and comment on various exotic proposals.

1 Introduction

Reconciling the LSND evidence [1] for $\bar{\nu}_\mu \to \bar{\nu}_e$ oscillations with the global neutrino data reporting evidence and bounds on oscillations remains a long-standing problem for neutrino phenomenology. Recently the MiniBooNE experiment [2,3] added more information to this question. This experiment searches for $\nu_\mu \to \nu_e$ appearance with a very similar L/E_ν range as LSND. No evidence for flavour transitions is found in the energy range where a signal from LSND oscillations is expected ($E > 475$ MeV), whereas an event excess is observed below 475 MeV at a significance of 3σ. Two-flavour oscillations cannot account for such an excess and currently the origin of this excess is under investigation [2], see also [4]. MiniBooNE results are inconsistent with a two-neutrino oscillation interpretation of LSND at 98% CL [3], see also [5]. The exclusion contour from MiniBooNE is shown in Fig. 1 (left) in comparison to the LSND allowed region and the previous bound from the KARMEN experiment [6], all in the framework of 2-flavour oscillations.

2 Sterile neutrino oscillations

The standard "solution" to the LSND problem is to introduce one or more sterile neutrinos at the eV scale in order to provide the required mass-squared difference to accommodate the LSND signal in addition to "solar" and "atmospheric" oscillations. However, in such schemes there is sever tension between the LSND signal and short-baseline disappearance experiments, most importantly Bugey [7] and CDHS [8], with some contribution also from atmospheric neutrino data [9].

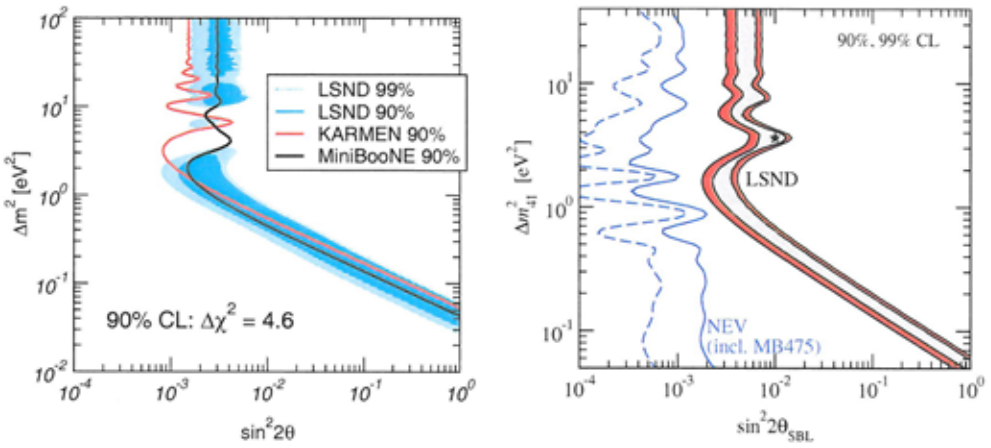

Figure 1: Left: Two-neutrino exclusion contours at 90% C.L. (2 d.o.f.) for MiniBooNE and KARMEN compared to the LSND allowed region at 90% and 99% C.L. For all three experiments the same $\Delta\chi^2$ cut has been used to define the 90% C.L. region. Right: Constraint on the LSND mixing angle in (3+1) schemes from no-evidence appearance and disappearance experiments (NEV) at 90% and 99% C.L. The shaded region corresponds to the allowed region from LSND decay-at-rest data.

I report here the results from a global analysis including MiniBooNE data within schemes with one, two and three sterile neutrinos [10].

Four-neutrino oscillations within so-called (3+1) schemes have been only marginally allowed before the recent MiniBooNE results [11,12,13], and become even more disfavored with the new data. We find that the LSND signal is disfavoured by all other null-result short-baseline appearance and disappearance experiments (including MiniBooNE) at the level of 4σ [10]. The corresponding upper bound on the effective LSND mixing angle is shown in Fig. 1 (right). Five-neutrino oscillations in (3+2) schemes [13] allow for the possibility of CP violation in short-baseline oscillations [14]. Using the fact that in LSND the signal is in anti-neutrinos, whereas present MiniBooNE data is based on neutrinos, these two experiments become fully compatible in (3+2) schemes [10]. Moreover, in principle there is enough freedom to obtain the low energy excess in MiniBooNE and being consistent at the same time with the null-result in the high energy part as well as with the LSND signal, see Fig. 2 (left, red histogram). However, in the global analysis the tension between appearance and disappearance experiments remains unexplained. This problem is illustrated in Fig. 2 (right) where sections through the allowed regions in the parameter space for appearance and disappearance experiments are shown. An opposite trend is clearly visible: while appearance data require non-zero values for the mixing of ν_e and ν_μ with the eV-scale mass states 4 and 5 in order to explain LSND, disappearance data provide an upper bound on this mixing. The allowed regions touch each other at $\Delta\chi^2 = 9.3$, and a consistency test between these two data samples yields a probability of only 0.18%, i.e., these models can be considered as disfavoured at the 3σ level [10]. Also, because of the constraint from disappearance experiments the low energy excess in MiniBooNE can not be explained in the global analysis, see Fig. 2 (left, blue histogram). Furthermore, when moving from 4 neutrinos to 5 neutrinos the fit improves only by 6.1 units in χ^2 by introducing 4 more parameters, showing that in (3+2) schemes the tension in the fit remains a sever problem. This is even true in the case of three sterile neutrinos, since adding one more neutrino to (3+2) cannot improve the situation [10].

3 Exotic proposals

Triggered by these problems many ideas have been presented in order to explain LSND, some of them involving very speculative physics, among them sterile neutrino decay [15,16], violation

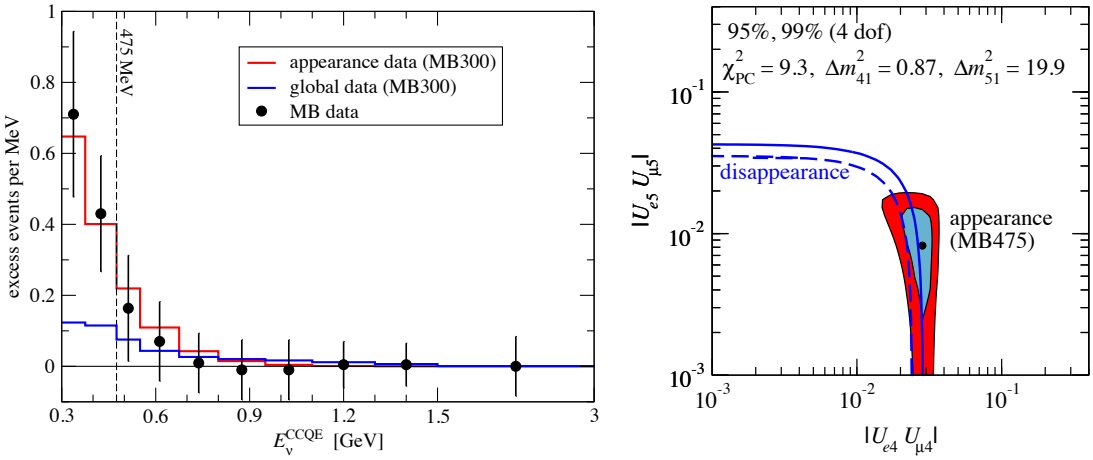

Figure 2: Left: Best fit spectra in (3+2) oscillations for MiniBooNE using appearance data only (MB, LSND, KARMEN, NOMAD) as well as in the global fit. Right: Section of the 4-dimensional volumes allowed at 95% and 99% CL in the (3+2) scheme from SBL appearance and disappearance experiments in the space of the parameters in common to these two data sets. The values of Δm^2_{41} and Δm^2_{51} of the displayed sections correspond to the point in parameter space where the two allowed regions touch each other (at a $\Delta\chi^2 = 9.3$).

of the CPT [17,12,18,19] and/or Lorentz [20] symmetries, quantum decoherence [21,22,23] mass-varying neutrinos [24], short-cuts of sterile neutrinos in extra dimensions [25], a non-standard energy dependence of sterile neutrinos [26], or sterile neutrinos interacting with a new gauge boson [27]. In the following I comment on a personal selection of these exotic proposals, without the ambition of being complete.

CPT violation. Triggered by the observation that the LSND signal is in anti-neutrinos, whereas their neutrino data is consistent with no oscillations, it was proposed [17] that neutrinos and anti-neutrinos have different masses and mixing angles, which violates the CPT symmetry. A first challenge to this idea has been the KamLAND reactor results, which require a Δm^2 at the solar scale for anti-neutrinos. Subsequently it has been shown that the oscillation signature in SuperK atmospheric neutrino data (which cannot distinguish between ν and $\bar{\nu}$ events) is strong enough to require a $\Delta m^2 \sim 2.5 \cdot 10^{-3}$ eV^2 for neutrinos as well as for anti-neutrinos [18], see [28] for an update. This rules out such an explanation of the LSND signal with three neutrinos at 4.6σ. However, introducing a sterile neutrino, and allowing for different masses and mixings for neutrinos and anti-neutrinos [19] is fully consistent with all data, including the MiniBooNE null-result in neutrinos. Such a model should lead to a positive signal in the MiniBooNE anti-neutrino run.

Sterile neutrino decay. Pre-MiniBooNE data can be fitted under the hypothesis [16] of a sterile neutrino, which is produced in pion and muon decays because of a small mixing with muon neutrinos, $|U_{\mu 4}| \simeq 0.04$, and then decays into an invisible scalar particle and a light neutrino, predominantly of the electron type. One needs values of $g m_4 \sim$ few eV, g being the neutrino–scalar coupling and m_4 the heavy neutrino mass, e.g. m_4 in the range from 1 keV to 1 MeV and $g \sim 10^{-6}$–10^{-3}. This minimal model is in conflict with the null-result of MiniBooNE. It is possible to save this idea by introducing a second sterile neutrino, such that the two heavy neutrinos are very degenerate in mass. If the mass difference is comparable to the decay width, CP violation can be introduced in the decay, and the null-result of MiniBooNE can be reconciled with the LSND signal [16].

Sterile neutrinos with an exotic energy dependence. Short-baseline data can be divided into low-energy (few MeV) reactor experiments, LSND and KARMEN around 40 MeV, and the high-energy (GeV range) experiments CDHS, MiniBooNE, NOMAD. Based on this observation it turns out that the problems of the fit in (3+1) schemes can be significantly alleviated if one

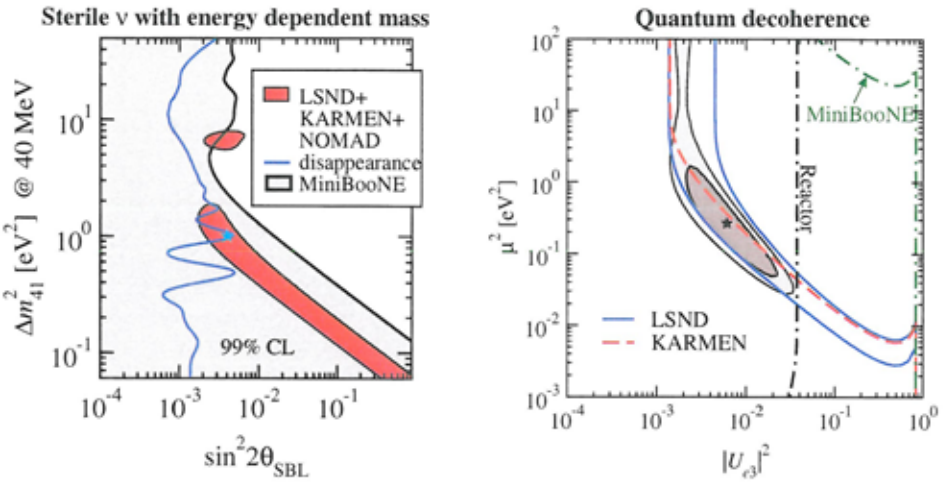

Figure 3: Left: Bounds from disappearance experiments and MiniBooNE compared to the LSND region for (3+1) oscillations when the sterile neutrino mass depends on energy as $m_4^2(E_\nu) \propto E_\nu^{-0.3}$. Right: Quantum decoherence in three-active neutrino oscillations. Lines correspond to 99% CL regions of individual experiments, shaded regions show the 90% and 99% CL region of the global analysis, and the star marks the best fit point. The parameter μ is defined by parameterizing the decoherence parameter γ as $\gamma = \mu^2/E_\nu\,(40\,\mathrm{MeV}/E_\nu)^3$.

assumes that the mass or the mixing of the sterile neutrino depend on its energy in an exotic way [26]. For example, assuming that $m_4^2(E_\nu) \propto E_\nu^{-r}$ one finds that for $r > 0$ the MiniBooNE exclusion curve is shifted to larger values of Δm^2, whereas the bound from disappearance experiments is moved towards larger values of the mixing angle, and hence the various data sets become consistent with LSND, compare Fig. 3 (left). At the best fit point with $r \simeq 0.3$ the global fit improves by 12.7 units in χ^2 with respect to the standard (3+1) fit. Similar improvement can be obtained if energy dependent mixing of the sterile neutrino is assumed.[26]

Let us note that this is a purely phenomenological observation, and it seems difficult to construct explicit models for such sterile neutrinos. There are models which effectively introduce a non-standard "matter effect" for sterile neutrinos, *e.g.* via exotic extra dimensions [25] or via postulating a new gauge interaction of the sterile neutrinos [27]. Similar as in the usual MSW case, the sterile neutrino encounters effective mass and mixing which depend on energy. However, in these approaches the matter effect felt by the sterile state has to be some orders of magnitude larger than the standard weak-force matter effect of active neutrinos, in order to be relevant for short-baseline experiments. In such a case, in general very large effects are expected for long-baseline experiments such as MINOS, atmospheric neutrinos, or KamLAND. Unfortunately an explicit demonstration that a successful description of all these data can be maintained in such models is still lacking.

Quantum decoherence. The possibility that the origin of the LSND signal might be quantum decoherence in neutrino oscillations has been considered in [21,22,23]. Such effects can be induced by interactions with a stochastic environment; a possible source for this kind of effect might be quantum gravity. The attempts to explain the LSND signal by quantum decoherence in [21,22] seem to be in conflict with present data. Both of these models are ruled out by the bound from NuTeV, $P_{\nu_\mu \to \nu_e}, P_{\bar\nu_\mu \to \bar\nu_e} < 5 \times 10^{-4}$ (90% C.L.) [29]. Furthermore, the model of [21] (where in addition to decoherence, CPT-violation is also introduced which results in a difference between the oscillation probabilities for neutrinos and anti-neutrinos) cannot account for the spectral distortion in the anti-neutrino signal observed by KamLAND, whereas the scenario of [22] is disfavored by the absence of a signal in KARMEN, NOMAD and MiniBooNE.

Recently we have revisited this idea [23] by introducing a different set of decoherence parameters. We assume that only the neutrino mass state ν_3 is affected by decoherence, whereas the 1-2

sector is completely unaffected, guaranteeing the standard explanation of solar and KamLAND data. Hence, denoting as γ_{ij} the parameter which controls the decohering of the mass states ν_i and ν_j, we have $\gamma_{12} = 0$ and $\gamma_{13} = \gamma_{23} \equiv \gamma$, where we have assumed that decoherence effects are diagonal in the mass basis. Furthermore, we assume that decoherence effects are suppressed for increasing neutrino energies, $\propto E_\nu^{-r}$ with $r \sim 4$. This makes sure that at short-baseline experiments with $E_\nu \gtrsim 1$ GeV such as MiniBooNE, CDHS, NOMAD, and NuTeV no signal is predicted, and at the same time maintains standard oscillations for atmospheric data and MINOS. In this way a satisfactory fit to the global data is obtained. Disappearance and appearance data become fully compatible with a probability of 74%, compared to 0.2% in the case of (3+2) oscillations. The LSND signal is linked to the mixing angle θ_{13}, see Fig. 3(right) and hence, this scenario can be tested at upcoming θ_{13} searches: while the comparison of near and far detector measurements at reactors should lead to a null-result because of strong damping at low energies, a positive signal for θ_{13} is expected in long-baseline accelerator experiments.

4 Outlook

Currently MiniBooNE is taking data with anti-neutrinos.[2] This measurement is of crucial importance to test scenarios involving CP (such as (3+2) oscillations) or even CPT violation to reconcile LSND and present MiniBooNE data. Therefore, despite the reduced flux and detection cross section of anti-neutrinos the hope is that enough data will be accumulated in order to achieve good sensitivity in the anti-neutrino mode. Furthermore, it is of high importance to settle the origin of the low energy excess in MiniBooNE. If this effect persists and does not find an "experimental" explanation such as an over-looked background, an explanation in terms of "new physics" seems to be extremely difficult. To the best of my knowledge, so-far no convincing model able to account for the sharp rise with energy while being consistent with global data has been provided yet.

The main goal of upcoming oscillation experiments like Double-Chooz, Daya Bay, T2K, NOνA is the search for the mixing angle θ_{13}, with typical sensitivities of[30] $\sin^2 2\theta_{13} \gtrsim 1\%$. This should be compared to the size of the appearance probability observed in LSND: $P_{\rm LSND} \approx 0.26\%$. Hence, if θ_{13} is large enough to be found in those experiments sterile neutrinos may introduce some sub-leading effect, but their presence cannot be confused with a non-zero θ_{13}. Nevertheless, I argue that it could be worth to look for sterile neutrino effects in the next generation of experiments. They would introduce (mostly energy averaged) effects, which could be visible as disappearance signals in the near detectors of these experiments. This has been discussed[31] for the Double-Chooz experiment, but also the near detectors at superbeam experiments should be explored. An interesting effect of (3+2) schemes has been pointed out recently for high energy atmospheric neutrinos in neutrino telescopes[32]. The crucial observation is that for $\Delta m^2 \sim 1$ eV^2 the MSW resonance occurs around TeV energies, which leads to large effects for atmospheric neutrinos in this energy range, potentially observable at neutrino telescopes. Another method to test sterile neutrino oscillations would be to put a radioactive source inside a detector with good spatial resolution, which would allow to observe the oscillation pattern within the detector[33]. I stress that in a given exotic scenario such as the examples discussed in sec. 3 signatures in up-coming experiments might be different than for "conventional" sterile neutrino oscillations.

For the subsequent generation of oscillation experiments aiming at sub-percent level precision to test CP violation and the neutrino mass hierarchy, the question of LSND sterile neutrinos is highly relevant[34,35]. They will lead to a miss-interpretation or (in the best case) to an inconsistency in the results. If eV scale steriles exist with mixing relevant for LSND the optimization in terms of baseline and E_ν of high precision experiments has to be significantly changed. Therefore, I argue that it is important to settle this question at high significance before decisions on high precision oscillation facilities are taken.

References

1. A. Aguilar *et al.* [LSND Coll.], Phys. Rev. D **64**, 112007 (2001) [hep-ex/0104049].
2. C. Polly, these proceedings.
3. A. A. Aguilar-Arevalo *et al.* [MiniBooNE Coll.], Phys. Rev. Lett. **98**, 231801 (2007).
4. R. Hill, these proceedings; J. A. Harvey, C. T. Hill and R. J. Hill, Phys. Rev. Lett. **99** (2007) 261601 [0708.1281].
5. A. A. Aguilar-Arevalo *et al.* [MiniBooNE Coll.], 0805.1764 [hep-ex].
6. B. Armbruster *et al.* [KARMEN Coll.], Phys. Rev. D **65**, 112001 (2002) [hep-ex/0203021].
7. Y. Declais *et al.*, Nucl. Phys. B **434**, 503 (1995).
8. F. Dydak *et al.*, Phys. Lett. B **134**, 281 (1984).
9. S. M. Bilenky, C. Giunti, W. Grimus and T. Schwetz, Phys. Rev. D **60**, 073007 (1999) [hep-ph/9903454].
10. M. Maltoni and T. Schwetz, Phys. Rev. D **76** (2007) 093005 [0705.0107].
11. M. Maltoni, T. Schwetz, M. A. Tortola and J. W. F. Valle, Nucl. Phys. B **643**, 321 (2002) [hep-ph/0207157].
12. A. Strumia, Phys. Lett. B **539**, 91 (2002) [hep-ph/0201134].
13. M. Sorel, J. M. Conrad and M. Shaevitz, Phys. Rev. D **70**, 073004 (2004) [hep-ph/0305255].
14. G. Karagiorgi *et al.*, Phys. Rev. D **75**, 013011 (2007) [hep-ph/0609177]; J. T. Goldman, G. J. . Stephenson and B. H. J. McKellar, Phys. Rev. D **75** (2007) 091301.
15. E. Ma, G. Rajasekaran and I. Stancu, Phys. Rev. D **61**, 071302 (2000) [hep-ph/9908489]; E. Ma and G. Rajasekaran, Phys. Rev. D **64**, 117303 (2001) [hep-ph/0107203].
16. S. Palomares-Ruiz, S. Pascoli and T. Schwetz, JHEP **0509**, 048 (2005) [hep-ph/0505216].
17. H. Murayama and T. Yanagida, Phys. Lett. B **520**, 263 (2001) [hep-ph/0010178]; G. Barenboim, L. Borissov and J. Lykken, hep-ph/0212116.
18. M. C. Gonzalez-Garcia, M. Maltoni and T. Schwetz, Phys. Rev. D **68**, 053007 (2003) [hep-ph/0306226].
19. V. Barger, D. Marfatia and K. Whisnant, Phys. Lett. B **576**, 303 (2003) [hep-ph/0308299].
20. V. A. Kostelecky and M. Mewes, Phys. Rev. D **70**, 076002 (2004) [hep-ph/0406255]; A. de Gouvea and Y. Grossman, Phys. Rev. D **74**, 093008 (2006) [hep-ph/0602237]; T. Katori, A. Kostelecky and R. Tayloe, Phys. Rev. D **74**, 105009 (2006) [hep-ph/0606154].
21. G. Barenboim and N. E. Mavromatos, JHEP **0501** (2005) 034 [hep-ph/0404014].
22. G. Barenboim, N. E. Mavromatos, S. Sarkar and A. Waldron-Lauda, Nucl. Phys. B **758** (2006) 90 [hep-ph/0603028].
23. Y. Farzan, T. Schwetz and A. Yu. Smirnov, 0805.2098 [hep-ph].
24. D. B. Kaplan, A. E. Nelson and N. Weiner, Phys. Rev. Lett. **93**, 091801 (2004) [hep-ph/0401099]; K. M. Zurek, JHEP **0410**, 058 (2004) [hep-ph/0405141]; V. Barger, D. Marfatia and K. Whisnant, Phys. Rev. D **73**, 013005 (2006) [hep-ph/0509163].
25. H. Pas, S. Pakvasa and T. J. Weiler, Phys. Rev. D **72**, 095017 (2005) [hep-ph/0504096].
26. T. Schwetz, JHEP **0802** (2008) 011 [0710.2985].
27. A. Nelson, these proceedings; A. E. Nelson and J. Walsh, 0711.1363 [hep-ph].
28. M. C. Gonzalez-Garcia and M. Maltoni, Phys. Rept. **460** (2008) 1 [0704.1800].
29. S. Avvakumov *et al.*, Phys. Rev. Lett. **89** (2002) 011804 [hep-ex/0203018].
30. P. Huber, M. Lindner, M. Rolinec, T. Schwetz and W. Winter, Phys. Rev. D **70** (2004) 073014 [hep-ph/0403068].
31. A. Bandyopadhyay and S. Choubey, 0707.2481 [hep-ph].
32. S. Choubey, JHEP **0712** (2007) 014 [0709.1937].
33. C. Grieb, J. Link and R. S. Raghavan, Phys. Rev. D **75**, 093006 (2007) [hep-ph/0611178].
34. A. Donini, M. Lusignoli and D. Meloni, Nucl. Phys. B **624** (2002) 405 [hep-ph/0107231].
35. A. Dighe and S. Ray, Phys. Rev. D **76** (2007) 113001 [0709.0383].

NEUTRINO CROSS SECTION MEASUREMENTS FOR LONG-BASELINE ACCELERATOR-BASED NEUTRINO OSCILLATION EXPERIMENTS

TEPPEI KATORI
Indiana University, Bloomington, Indiana, USA

Neutrino oscillations are clear evidence for physics beyond the standard model. The goal of next-generation neutrino oscillation experiments is to find a non-zero θ_{13}, the last mixing matrix element for which we only know an upper limit. For this, next-generation long-baseline neutrino oscillation experiments require an order of magnitude better sensitivities. In particular, accelerator-based experiments such as T2K and NOvA experiments need (1) good neutrino energy reconstruction for the precise measurement of Δm^2_{32} and $sin^2 2\theta_{23}$, and (2) good background prediction to measure ν_e appearance signals. Current and near future high statistics neutrino experiments, such as K2K, MiniBooNE, SciBooNE, MINOS, and MINERvA help both (1) and (2) by precise signal and background channel measurements.

1 next-generation long baseline accelerator-based neutrino oscillation experiments

The goal of next-generation long baseline accelerator-based neutrino oscillation experiments is to measure a non-zero θ_{13}, the last mixing matrix element. The value of θ_{13} is the important parameter to access beyond the standard model physics. Especially if it were non-zero, then we hope to measure leptonic CP violation which can help to understand leptogenesis, one of the candidate explanations of baryon asymmetry of the universe [1].

Currently two experiments are planned, the Tokai-to-Kamioka (T2K) experiment [2] ($\sim$ 800 MeV, $\sim$ 300 km) and the NuMI Off-axis ν_e Appearance (NOvA) experiment [3] ($\sim$ 2 GeV, $\sim$ 800 km). Both experiments use a ν_μ beam and search for ν_e appearance events to measure θ_{13} through the equation,

$$P(\nu_\mu \to \nu_e) = sin^2\theta_{23} sin^2 2\theta_{13} sin^2 \left(1.27 \frac{\Delta m^2_{32}(eV^2) L(km)}{E(GeV)}\right). \quad (1)$$

Since a small $P(\nu_\mu \to \nu_e)$ is proportional to $sin^2\theta_{23}$ and $sin^2\left(1.27\frac{\Delta m^2_{32} L}{E}\right)$, we also need accurate knowledge of these two quantities, and can achieve by the measurements of ν_μ disappearance

events,

$$P(\nu_\mu \to \nu_\mu) = 1 - sin^2 2\theta_{23} sin^2 \left(1.27 \frac{\Delta m^2_{32}(eV^2) L(km)}{E(GeV)}\right). \quad (2)$$

The oscillation parameters are extracted from the shape of $P(\nu_\mu \to \nu_\mu)$, a function of reconstructed neutrino energy. Therefore a good extraction of $sin^2\theta_{23}$ and Δm^2_{32} rely on good reconstruction of neutrino energy, which is based on better understanding of the signal (ν_μCCQE) and background interactions, mainly CC1π° interaction (Sec. 2).

The signal of ν_e appearance is an electron,

$$\nu_e + n \to p + e^-. \quad (3)$$

There are many kind of possible backgrounds for this signal, for example, sometimes ν_μ induced NCπ° production can mimic a ν_e event if one of the decay photons from π° decay is undetected. Therefore, it is critical to understand this background channel (Sec. 3).

It is important to perform these cross section measurements prior to oscillation experiments. Although all long baseline accelerator-based neutrino oscillation experiments have near detectors, they exist to constrain neutrino flux uncertainties, and this constraint relies on accurate knowledge of cross section measurements. Fig. 1 shows the world's data for charged current cross sections. As you can see, existing data are rather sparse and old. Since two experiments, T2K and NOvA, span different energy ranges, we need cross section measurements in both regions because the dominant interaction types will be different, and thus their energy reconstructions and backgrounds are different. Fortunately, we have a lot of new input from current and future neutrino cross section measurements: K2K near detector [5] ($\sim$ 1.2 GeV, completed), MiniBooNE [6] ($\sim$ 800 MeV, ongoing), SciBooNE [7] ($\sim$ 800 MeV, ongoing), MINOS near detector [8] ($\sim 2-20$ GeV, ongoing), and MINERvA [9] ($\sim 2-20$ GeV, approved). We would like to discuss the two main themes of cross section related issues impacting oscillation searches, (1) neutrino energy reconstruction (Sec. 2), and (2) background determination (Sec. 3).

2 Neutrino energy reconstruction

2.1 Neutrino energy reconstruction for T2K

At the T2K energy scale ($\sim$ 800 MeV), the dominant neutrino reactions are ν_μ charged current quasi-elastic (CCQE) interactions,

$$\nu_\mu + n \to p + \mu^-. \quad (4)$$

This channel is used to measure ν_μ disappearance, and thus the ν_μ energy reconstruction is critical. Since neutrino oscillation experiments use nuclear targets, understanding of this interaction is not trivial. Recently K2K [5,10] and MiniBooNE [6] have reported new measurements of the axial mass, M_A, which are higher than the historical value (Table 1).

In this energy range, the axial vector form factor is the dominant contribution to the cross section and controls the Q^2 dependence. Inconsistency of their results from the world average, and the consistency between K2K and MiniBooNE is best understood in terms of nuclear effects, because most of the past experiments used deuterium targets whereas K2K and MiniBooNE used oxygen and carbon. Instead of using the world average, both experiments employ their measured M_A values to better simulate CCQE events in their oscillation analyses. After the

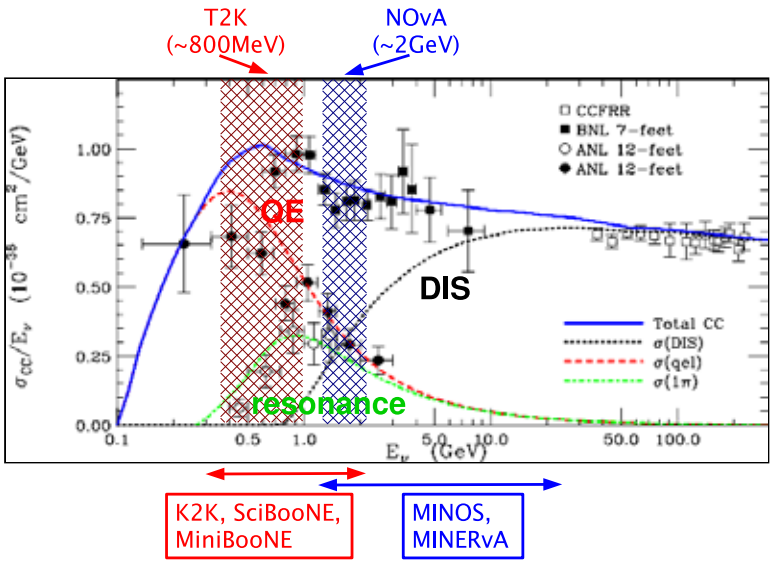

Figure 1: The world data for ν_μ charged current cross section divided by neutrino energy. The dominant interaction for T2K and NOvA are quasi-elastic (QE) and deep inelastic scattering (DIS) respectively. The existing data are rather sparse and old, but we have more new input from current and future experiments!

	M_A(GeV)	target
K2K (SciFi) [5]	1.20 ± 0.12	oxygen
K2K (SciBar) [10]	1.14 ± 0.11	carbon
MiniBooNE [6]	1.23 ± 0.20	carbon
world average [11]	1.026 ± 0.021	deuteron, etc

Table 1: The comparison of measured axial mass M_A.

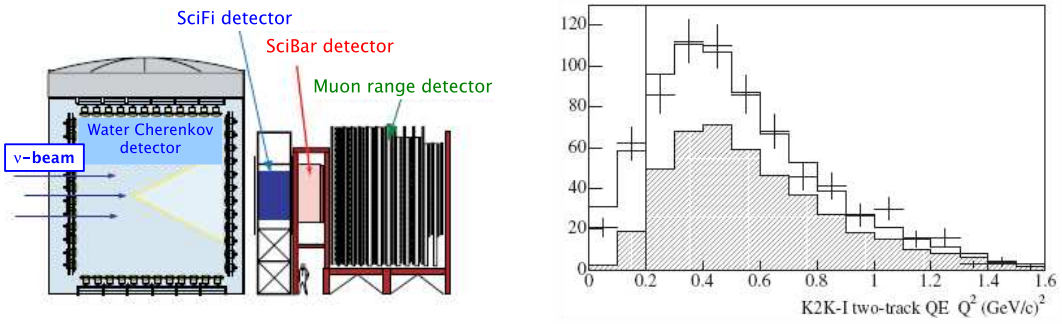

Figure 2: (Left) K2K near detector complex. From the left to right, 1 kiloton water Čerenkov detector "1KT", scintillation-fiber/water target tracker "SciFi", fully active plastic organic scintillation-bar tracker "SciBar", and muon range detector "MRD". (Right) reconstructed Q^2 plot for 2-track QE sample from K2K SciFi, data (crosses) and simulation with best-fit M_A (solid) agree well. The shaded region indicates the fraction of signal ($\nu_\mu CCQE$) events.

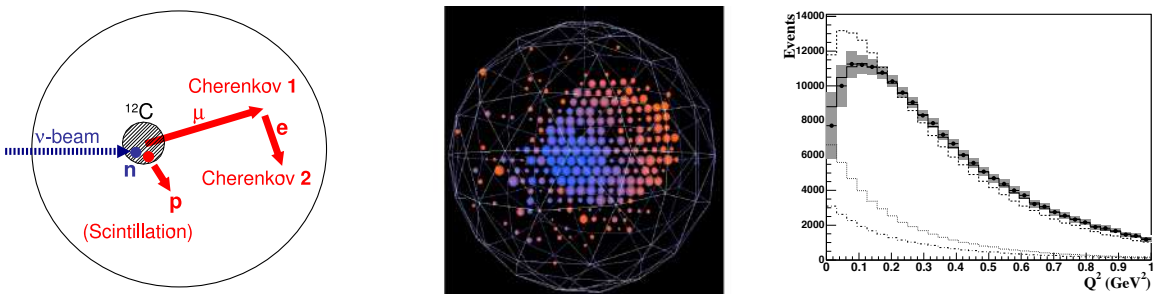

Figure 3: (Left) Schematic figure of a ν_μ CCQE interaction in MiniBooNE. The MiniBooNE detector is a Čerenkov detector filled with mineral oil surrounded by PMTs. The Čerenkov light from the muon (Cherenkov 1) and subsequent Čerenkov light from the decayed electron are used to tag the CCQE event. (Middle) Event display of a muon candidate event in MiniBooNE. Each sphere represents a hit on a PMT, and size and color show charge and time information respectively. Muons create shape-edged Čerenkov ring. The ring center will appear filled-in if the muon is stopping in the tank. (Right) Reconstructed Q^2 plot of MiniBooNE, data (dots), simulation before the fit (dashed), and after the fit with M_A and Pauli-blocking (solid). The dotted and dash-dotted lines indicate total background and irreducible background fraction respectively.

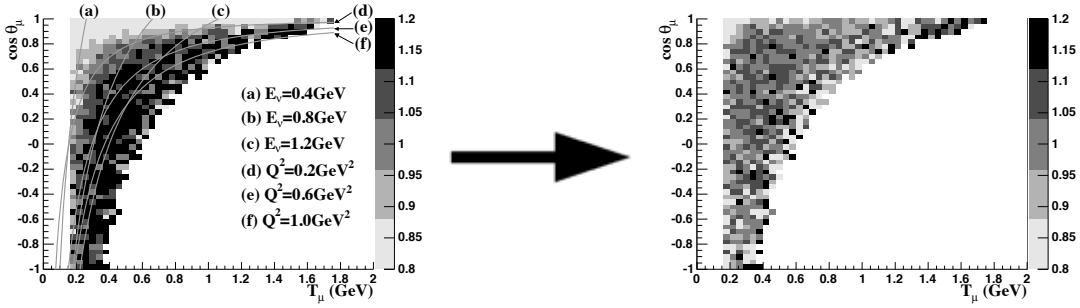

Figure 4: Ratio of MiniBooNE ν_μCCQE data-simulation in the 2-dimensional plane of muon kinetic energy vs. muon angle. If the prediction well-describes the data, then this plot should exhibit a uniform distribution centered on unity. (Left) before CCQE cross section model tuning, the light gray region shows an excess of predicted events, and the black region shows a deficit of predicted events. The auxiliary lines from (a) to (f) indicate lines of equal E_ν or Q^2. The data-simulation discrepancy follows line of constant Q^2, suggesting an incorrect cross section model in the simulation. (Right) after cross section model tuning, specifically adjustment of M_A and Pauli-blocking.

M_A adjustment, both experiments see good agreement between data and simulation (Fig 2 and 3).

We can only measure the interaction rate, which is the convolution of flux and cross section ($R = \int \Phi \times \sigma$). So, without knowing flux prediction is perfect, one cannot tune the cross section model from measured interaction rate. MiniBooNE carefully examined this, and showed that their observed data simulation mismatching is not the effect of mismodeling of neutrino flux, but is really a cross section model problem. Fig 4 shows the ratio of data-simulation in the 2-dimensional plane made in muon kinetic energy and angle; left plot is before any cross section model tuning, right plot is after. The key point is that left plot clearly shows that data-simulation disagreements follow equal Q^2 lines, not equal E_ν lines.

$$R = \int \Phi \times \sigma \;\rightarrow\; R[E_\nu, Q^2] = \int \Phi[E_\nu] \times \sigma[Q^2] \tag{5}$$

This is strong evidence that the MiniBooNE data suggests a problem with the cross section model, and not the beam model, because cross section is the function of Q^2, whereas neutrino beam is a function of E_ν.

It is not only important to understand the energy reconstruction of signal events (*i.e.*, CCQE interaction), but also for background channels. For Super-K, the neutrino energy is reconstructed

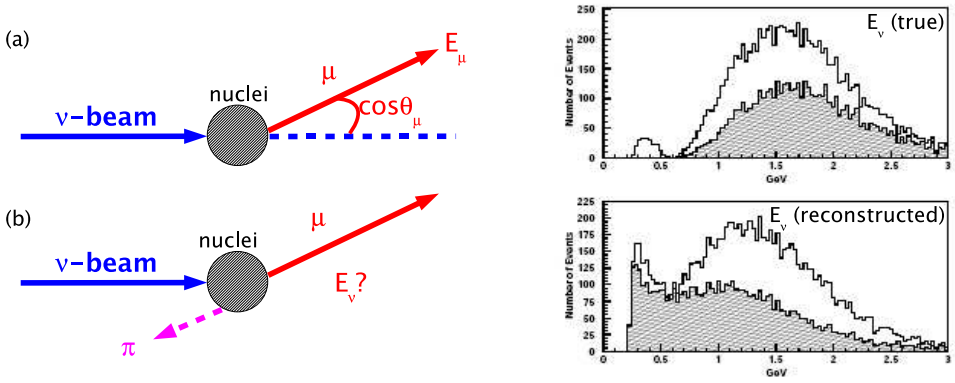

Figure 5: (Left) (a) CCQE interaction and (b) CC1π interaction. Eq. 6 correctly reconstructs neutrino energy only for (a). (b) can be distinguished from (a) by additional pion, however when pion is lost (by pion absorption for example), (b) becomes indistinguishable from intrinsic backgrounds. When (a) and (b) have the same muon kinematics, the reconstructed neutrino energies are the same, however the true neutrino energy for (b) is higher due to the creation of the pion in the event (neutrino energy mis-reconstruction). (Right) true and reconstructed neutrino energy distribution for Super-K predictions with neutrino oscillations. The shaded region is non-QE (mainly CC1π) channels. As can be seen from the bottom plot, CC1π background events are misreconstructed at lower neutrino energies and hence can fill out the dip created by neutrino oscillations.

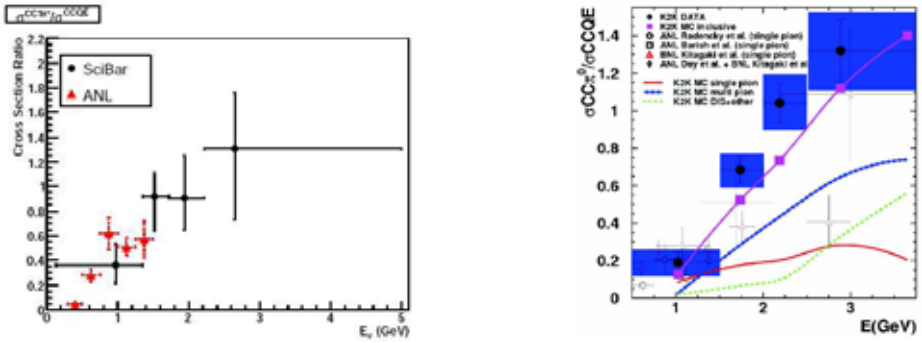

Figure 6: (Left) charged current 1π production to CCQE cross section ratio from K2K SciBar analysis. Their result is consistent with past ANL bubble chamber experiment. (Right) charged current inclusive 1π° production to CCQE cross section ratio from K2K SciBar analysis. Although the errors are large, the cross section obtained is significantly higher than the cross section model used in the K2K experiment.

from the measured muon energy E_μ and angle θ_μ, assuming a CCQE interaction,

$$E_\nu^{QE} \sim \frac{M_N E_\mu - \frac{1}{2}m_\mu^2}{M_N - E_\mu + \sqrt{E_\mu^2 - m_\mu^2}cos\theta_\mu}. \quad (6)$$

Here, M_N and m_μ are nucleon and muon masses. Since this formula assumes a 2-body interaction, any interaction involving more than two particles is a source of neutrino energy mis-reconstruction (Fig 5, left). The most notable channel contributing to this is charged current 1 π (CC1π) production. Especially when the detection of the outgoing pion fails for various reasons (pion absorption, detector effect, etc), CC1π events become an irreducible background, and thus they need to understand their relative contribution rather than rejecting them by cuts [4] (Fig. 5, right).

Although neutrino absolute cross sections are notoriously difficult to measure due to uncertainties in the incoming neutrino flux, here they only need to know the kinematic distribution of CC1π events compared with CCQE events. Such measurements were done in K2K (Fig. 6) [12,13] and MiniBooNE [14].

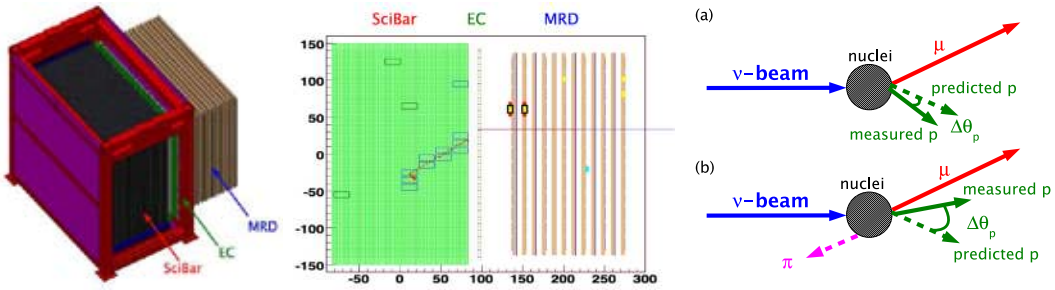

Figure 7: (Left) SciBooNE detector. It consists of 3 parts, organic plastic scintillation-bar tracker "SciBar", 11 radiation length lead electromagnetic calorimeter "EC", and muon range detector "MRD" which can range out muons up to 0.9 GeV. (Middle) SciBooNE event display for ν_μ CCQE candidate event. two tracks are seen in "SciBar", then the longer track (muon) produce hits in both "EC" and "MRD". (Right) Under the assumption of target nucleon at rest, muon energy and angle completely specify CCQE kinematics, *i.e.*, one can predict the angle of outgoing proton. $\Delta\theta_p$ is defined as an opening angle of this predicted proton track and measured proton track. (a) is the case of CCQE interaction, and $\Delta\theta_p$ is small. However, (b) CC1π interaction with invisible pion, $\Delta\theta_p$ is large because predicted track is based on the assumption of 2-body interaction but actual interaction is 3-body.

The SciBooNE experiment [7] at FNAL is particularly designed for this purpose (Fig. 7, left and middle). The SciBooNE vertex detector "SciBar", formerly used at K2K experiment and shipped from Japan to Fermilab, is a high resolution tracker consisting of X-Y plastic organic scintillators with wavelength shifting fibers through the middle of each bar. Since SciBar can reconstruct both proton and muon tracks in a ν_μ CCQE interaction (unlike Čerenkov detectors), so the opening angle of the measured proton and the expected outgoing proton (assuming CCQE kinematics) can be used to separate CCQE and CC1π events, even in cases where the pion is undetected (right plot of Fig. 7). The goal of the SciBooNE experiment is to measure non-QE to CCQE cross section ratio to 5%, making the non-QE mis-reconstruction uncertainty for T2K negligible [7].

2.2 Neutrino energy reconstruction for NOvA and MINOS

The situation is quite different for higher energy scales ($\sim$ 2 GeV). The CCQE assumption is no longer held and calorimetric energy reconstruction provides a much more efficient energy determination:

$$E_\nu \sim E_\mu + E_{showers} \tag{7}$$

Here, E_μ is the energy of muon, usually measured by a muon spectrometer which consists of a dense material to stop muons. $E_{showers}$ is the energy of both electromagnetic and hadronic showers measured in the calorimeter. This energy reconstruction method is successfully tested by the Main Injector Neutrino Oscillation Search (MINOS) experiment [8].

Neutrino energy misreconstruction happens, for example, when hadronic showers are absorbed by nuclei (Fig. 8, left). This is important for precise ν_μ disappearance measurements by MINOS, where steel is used as a target but no reliable pion absorption measurements are available. The future Main Injector Experiment for ν-A (MINERvA) has the ability to switch its target and they plan to study nuclear effects (Fig. 8, middle and left) as well as various physics topics from quasi-elastic to DIS [9]. Their measurements will significantly reduce the uncertainties on Δm^2_{23} coming from nuclear cross section modeling in MINOS [9].

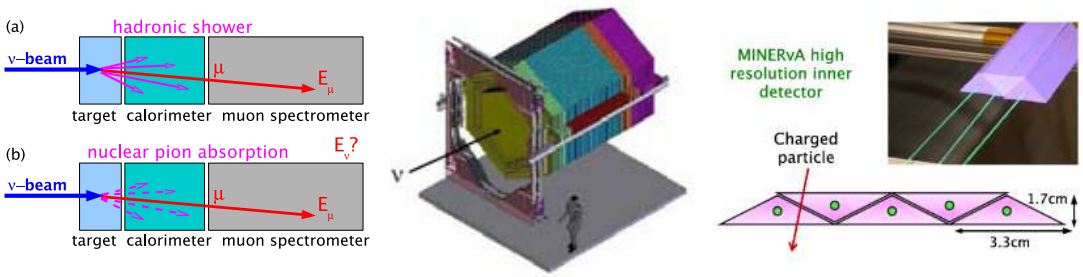

Figure 8: (Left) calorimetric energy reconstruction. The detector can be separated into 3 part, target, calorimeter, and muon spectrometer. (a) is the ideal situation, but often hadronic showers are missed, for example by nuclear pion absorption like (b), and give incorrect neutrino energy. (Middle) MINERvA detector. Front planes are target region, where MINERvA has ability to switch nuclear targets. The interior of the detector consists of a high resolution organic plastic scintillation tracker, and the outside is a magnetized calorimeter. (Right) picture of MINERvA inner detector scintillation-bar and schematic view. It consists of plastic organic scintillator with wavelength shifting fibers. The array of triangular bars have high resolution by the extraction of particle tracks from the amount of shared light by each scintillation-bar.

3 Background channel

Since T2K uses water Čerenkov detector "Super-K" as a far detector, the signal of θ_{13}, namely ν_e appearance is a single electron (Eq. 3) because outgoing protons are below Čerenkov threshold in most cases and therefore invisible.

The notorious background for this signal is the neutral current π° (NCπ°) interaction,

$$\nu_\mu + N \rightarrow \nu_\mu + N + \pi^o. \tag{8}$$

Although π° decays to two photons, there are various reasons to miss one of them, for example, two photons overlap, or one photon is boosted to low energy below threshold. The precise prediction of this channel is critical for any ν_e appearance experiments. K2K measured the NCπ° rate using 1KT detector [15].

Recently, the MiniBooNE experiment made an *in-situ* measurement of NCπ° production on mineral oil which was used to predict background processes more precisely for their ν_e appearance search [16]. Even though the underlying source of the π° may not be known, (*i.e.*, actual resonance model to create the π° is not clear), the difference between the observed and predicted kinematic distribution of π°'s can be used to correct the rate of π° events that are misclassified as ν_e signal events. Since the loss of a photon in the π° decay is mostly a kinematic effect, once correct π° production kinematics are obtained from the data, it is easy to calculate the distribution of π° where one photon is missed. Left plot of Fig. 9 shows data-simulation comparisons for pion mass peak. After the correction, their simulation precisely predicts all observed aspects of NCπ° events. The right plot of Fig. 9 shows a kinematic distribution.

This result triggered another interest. This plot clearly shows the existence of NC coherent pion production. However, the K2K experiment saw no evidence for CC coherent pion production at similar energies [12]. Since a coherently produced pion has very different kinematics, understanding of this rate is important. Again, further analysis of K2K, MiniBooNE, SciBooNE, MINOS, and MINERvA will shed light on this in the near future.

The fine-grained MINERvA detector will provide critical input for NOvA. Although high statistics data from K2K, MiniBooNE, and SciBooNE will be available, backgrounds of ν_e appearance search around $\sim$ 2 GeV is only effectively accessible by MINERvA experiments. We are expecting negligible cross section error on $sin^2 2\theta_{13}$ from NOvA after precise CC and NC measurements from MINERvA [9].

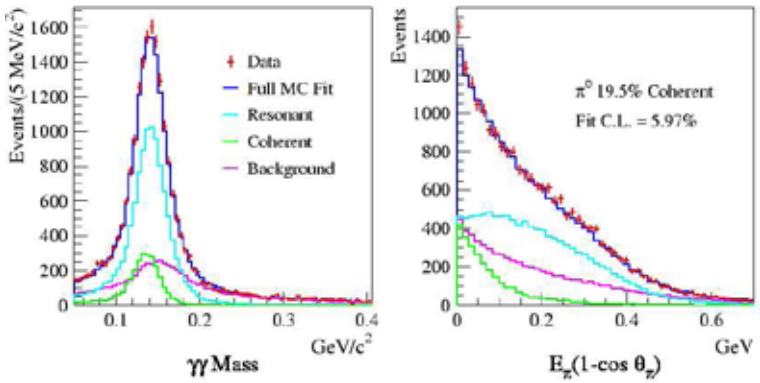

Figure 9: (Left) reconstructed π° mass peak for MiniBooNE after the correction of π° kinematics and coherent π° fraction. (Right) data-simulation comparison of one of kinematic variable. The template fit obtains a 19.5% coherent fraction (coherent events are sharply peaked in the forward direction, *i.e.*, low $E_\pi(1-cos\theta_\pi)$).

4 Conclusions

The goal of next-generation long baseline accelerator-based neutrino oscillation experiments is to measure a ν_e appearance signal. The cross section errors arise from (1) misreconstruction of neutrino energy and (2) incorrect background predictions. The inputs from current and future neutrino cross section measurements are critical to the success of future oscillation experiments, such as T2K and NOvA.

References

1. R. N. Mohapatra *et al.*, arXiv:hep-ph/0412099.
2. Y. Itow *et al.* [The T2K Collaboration], arXiv:hep-ex/0106019.
3. D. S. Ayres *et al.* [NOvA Collaboration], arXiv:hep-ex/0503053.
4. C. W. Walter, AIP Conf. Proc. **967**, 3 (2007).
5. R. Gran *et al.* [K2K Collaboration], *Phys. Rev.* D **74**, 052002 (2006).
6. A. A. Aguilar-Arevalo *et al.* [MiniBooNE Collaboration], *Phys. Rev. Lett.* **100**, 032301 (2008); Teppei Katori [MiniBooNE Collaboration], AIP Conf. Proc. **967**, 123 (2007).
7. A. A. Aguilar-Arevalo *et al.* [SciBooNE Collaboration], arXiv:hep-ex/0601022.
8. D. G. Michael *et al.* [MINOS Collaboration], *Phys. Rev. Lett.* **97**, 191801 (2006).
9. D. Drakoulakos *et al.* [MINERvA Collaboration], arXiv:hep-ex/0405002.
10. X. Espinal and F. Sanchez [K2K Collaboration], AIP Conf. Proc. **967**, 117 (2007).
11. V. Bernard *et al.*, J. Phys. **G28**, R1 (2002).
12. C. Mariani [K2K Collaboration], AIP Conf. Proc. **967**, 174 (2007).
13. A. Rodriguez, L. Whitehead, *et al* [K2K Collaboration], arXiv:0805.0186v1.
14. M. O. Wascko [MiniBooNE Collaboration], Nucl. Phys. Proc. Suppl. **159**, 50 (2006).
15. S. Nakayama *et al.* [K2K Collaboration], Phys. Lett. B **619**, 255 (2005).
16. A. A. Aguilar-Arevalo *et al.* [MiniBooNE Collaboration], arXiv:0803.3423v1.

HARP COLLABORATION RESULTS ON THE PROTON-NUCLEI INTERACTIONS AT FEW GEV ENERGIES

Roumen Tsenov
Department of Atomic Physics, Faculty of Physics,
St. Kliment Ohridski University of Sofia, Sofia, Bulgaria
(on behalf of the HARP Collaboration)

Recent results obtained by the HARP collaboration on the measurements of the double-differential production cross-section of positive and negative pions in proton interactions with nuclear targets from Beryllium to Lead are presented. They cover production at small angles (30-210 mrad) and relatively large momenta up to 8 GeV/c as well as large angles (0.35 - 2.15 rad) and small momenta (0.1 - 0.8 GeV/c). These results are relevant for a detailed understanding of neutrino fluxes in accelerator neutrino experiments, better prediction of atmospheric neutrino fluxes, optimization of a future neutrino factory design and for improvement of hadronic generators widely used by the HEP community in the simulation of hadronic interactions.

1 The HARP experiment

The HARP experiment [1,2] at the CERN PS was designed to make measurements of hadron yields from a large range of nuclear targets and for incident particle momenta from 1.5 GeV/c to 15 GeV/c. The main motivations are the measurement of pion yields for a quantitative design of the proton driver of a future neutrino factory, a substantial improvement in the calculation of the atmospheric neutrino flux and the measurement of particle yields as input for the flux calculation of accelerator neutrino experiments, such as K2K [3,4], MiniBooNE [5] and SciBooNE [6].

The experiment makes use of a large-acceptance spectrometer consisting of a forward and large-angle detection systems. A detailed description of the experimental apparatus can be found in Ref. [2]. The forward spectrometer – based on large area drift chambers and a dipole magnet complemented by a set of detectors for particle identification [8]: a time-of-flight wall, a large Cherenkov detector and an electromagnetic calorimeter – covers polar angles up to 250 mrad which is well matched to the angular range of interest for the conventional neutrino beams. The large-angle spectrometer – based on a Time Projection Chamber (TPC) and Resistive Plate Chambers (RPCs), located inside a solenoidal magnet – has a large acceptance in the momentum and angular range for the pions relevant to the production of the muons in a neutrino factory. It covers the large majority ($\sim 70\%$) of the pions accepted in the focusing system of a typical design.

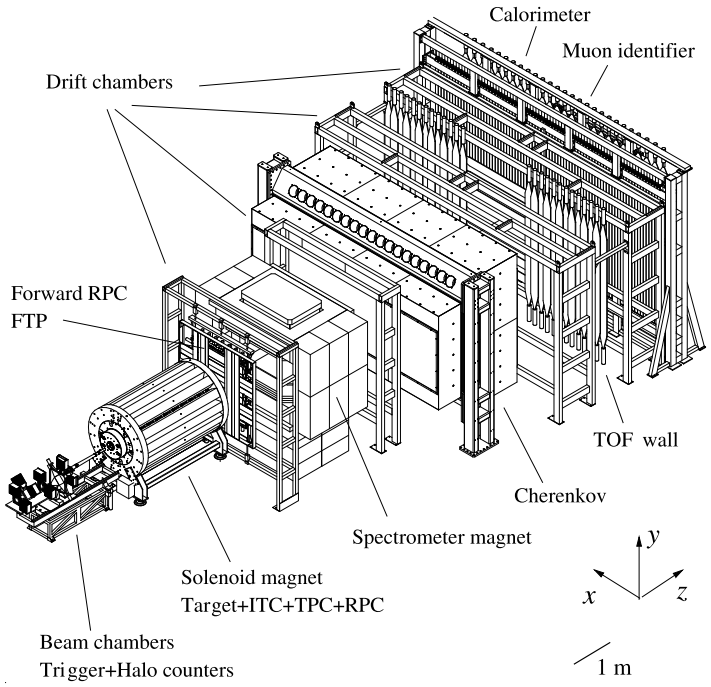

Figure 1: Overall mechanical layout of the HARP detector. The different sub-detectors are shown. The target is inserted inside the TPC.

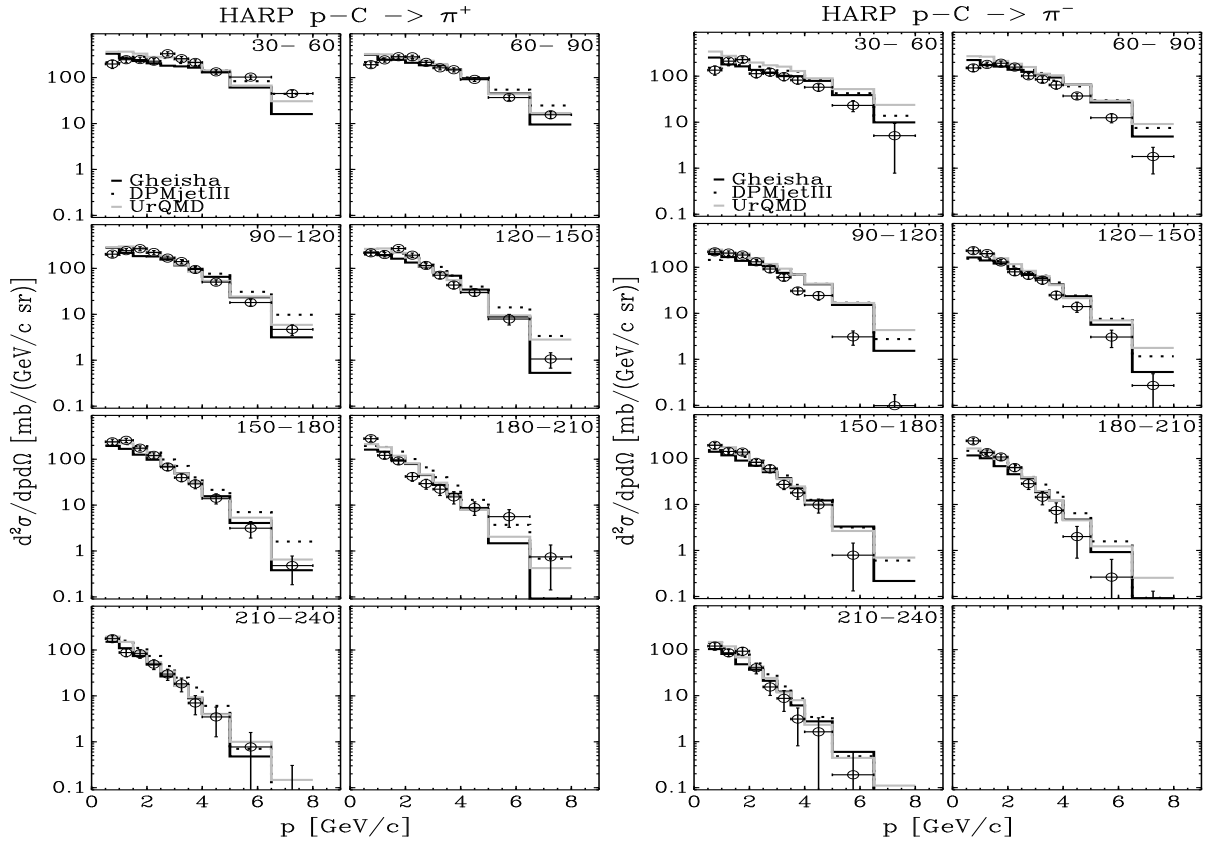

Figure 2: Double-differential production cross-section of π^+ and π^- in p–C reactions at 12 GeV/c (points with error bars) and comparison with model predictions.

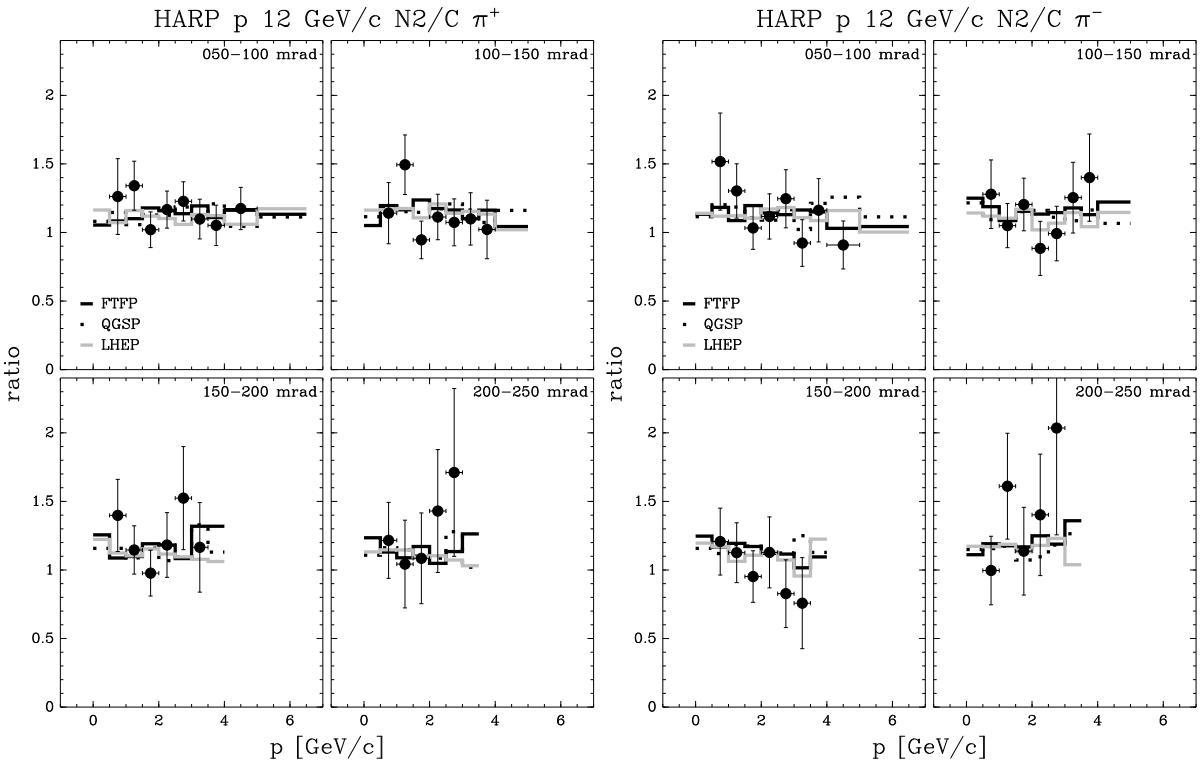

Figure 3: p–N_2 to p–C production ratio for π^+ and π^- at 12 GeV/c, compared with GEANT4 simulation predictions using different models. Only statistical errors are displayed, since most systematic ones cancel.

2 Results obtained with the HARP forward spectrometer

The first HARP physics publication [7] reported measurements of the π^+ production cross-section from an aluminum target at 12.9 GeV/c proton momentum for the K2K experiment at KEK PS. The results were subsequently applied to the final neutrino oscillation analysis of K2K [4], allowing a significant reduction of the dominant systematic error associated with the calculation of the so-called far-to-near ratio. Our next result [9] was the measurement of the π^+ cross-sections from a thin 5% λ_I beryllium target at 8.9 GeV/c proton momentum. It contributed to the understanding of the MiniBooNE and SciBooNE neutrino fluxes [10]. They are both produced by the Booster Neutrino Beam at Fermilab which originates from protons accelerated to 8.9 GeV/c by the booster before being collided against a beryllium target.

Further, measurements of the double-differential production cross-section of $\pi^\pm$ in the collision of 12 GeV/c protons and $\pi^\pm$ with thin 5% λ_I carbon target and liquid N_2 and O_2 targets were performed . These measurements are important for a precise calculation of the atmospheric neutrino flux and for a prediction of the development of extended air showers. The results for the pion production on the carbon target, the ratio N_2/Carbon, and comparison with models typically used in air shower simulations [11] are shown in Figs. 2 and 3 [12]. The conclusion of comparing the predictions of the models to the measured data is that they do predict the ratio of cross-sections and often fail in predicting the absolute rates, especially in certain regions of the phase space.

In practice production targets are not thin and cascade calculations or dedicated measurements with 'replica targets' are needed. HARP has taken, albeit with somewhat lower statistics, and analyzed p+A data at different beam momenta with 100% λ_I targets. They can be used for parametrizations or tuning of models. Preliminary spectra are available for p + Be, C, Al, Cu, Sn, Ta, Pb interactions at 3 – 12 GeV/c. The measurements are on the tapes and can be analyzed on demand.

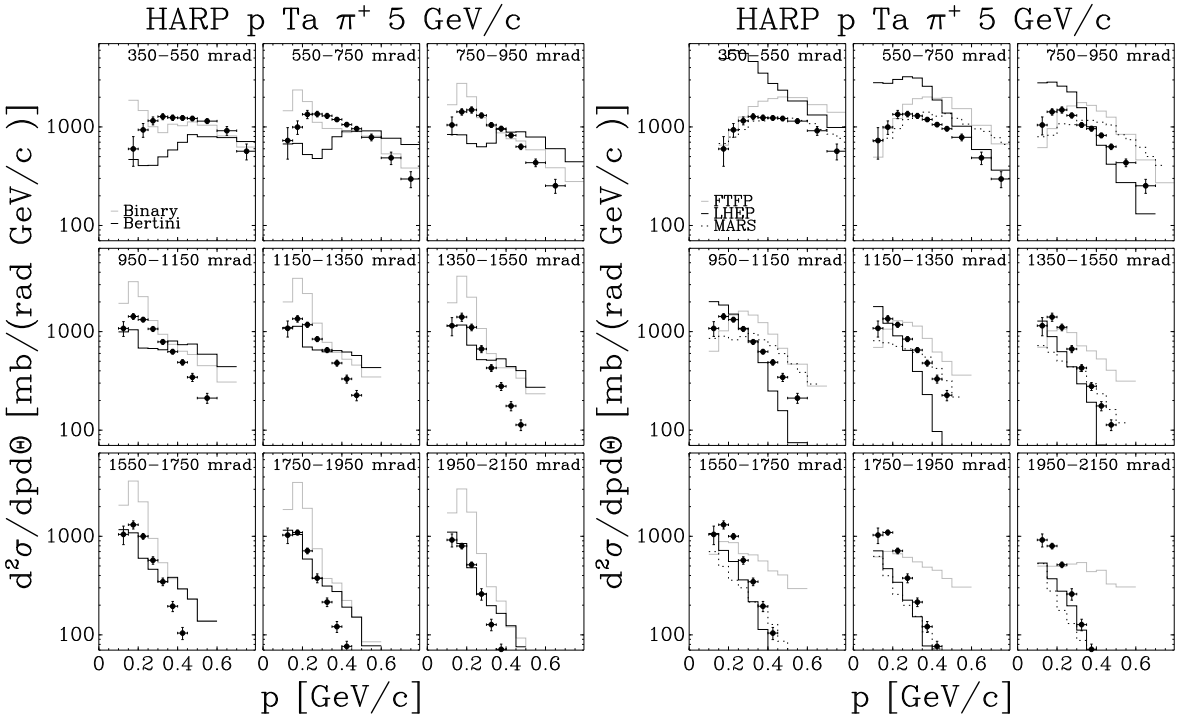

Figure 4: Double-differential π^+ production cross sections for p–Ta at 5 GeV/c and comparison with GEANT4 and MARS MC predictions, using several generator models.

3 Results obtained with the HARP large-angle spectrometer

The HARP TPC is the key detector for the analysis of tracks emerging from the target at large angles with respect to the incoming beam direction. It suffered from a number of shortcomings that were discovered during and after the data taking [2]. A description of the measures taken to correct for the effects of them is given in [2,15,16]. Wide range of experimental cross-checks has been employed to assess the momentum scale and momentum resolution in the HARP TPC, summarized in our recent paper [16].

A group of people formerly belonging to the HARP collaboration and subsequently detached themselves from it have been criticizing our methods of TPC and RPCs calibration [13]. Our arguments against this criticism and for the correctness of our results are presented in [14,16].

A first set of results on the production of pions at large angles have been published by the HARP collaboration in the papers [15,18], based on the analysis of the data in the beginning of each accelerator spill. Track recognition, momentum determination and particle identification were all performed based on the measurements made with the TPC. The reduction of the data set was necessary to avoid problems in the chamber responsible for dynamic distortions to the image of the particle trajectories as the ion charge was building up during each spill. Corrections for such distortions that allow the use of the full statistics have been developed [16] and applied in the analysis. The results exploiting the full spill data have been obtained recently [17]. They are fully compatible with the previous ones and cover pion production by proton beams in a momentum range from 3 GeV/c to 12 GeV/c hitting Be, C, Al, Cu, Sn, Ta and Pb targets with a thickness of 5% λ_{I} in the angular and momentum phase space 100 MeV/c $\leq p <$ 800 MeV/c and 0.35 rad $\leq \theta <$ 2.15 rad in the laboratory frame.

As an example we show in Fig. 4 the results for the double-differential cross-sections $\mathrm{d}^2\sigma/\mathrm{d}p\mathrm{d}\theta$ at 5 GeV/c incident proton beam momentum and Ta target compared to the respective predictions of several different generator models used in GEANT4 and MARS simulation packages. The comparison between data and models is reasonable, but some discrepancies are evident for

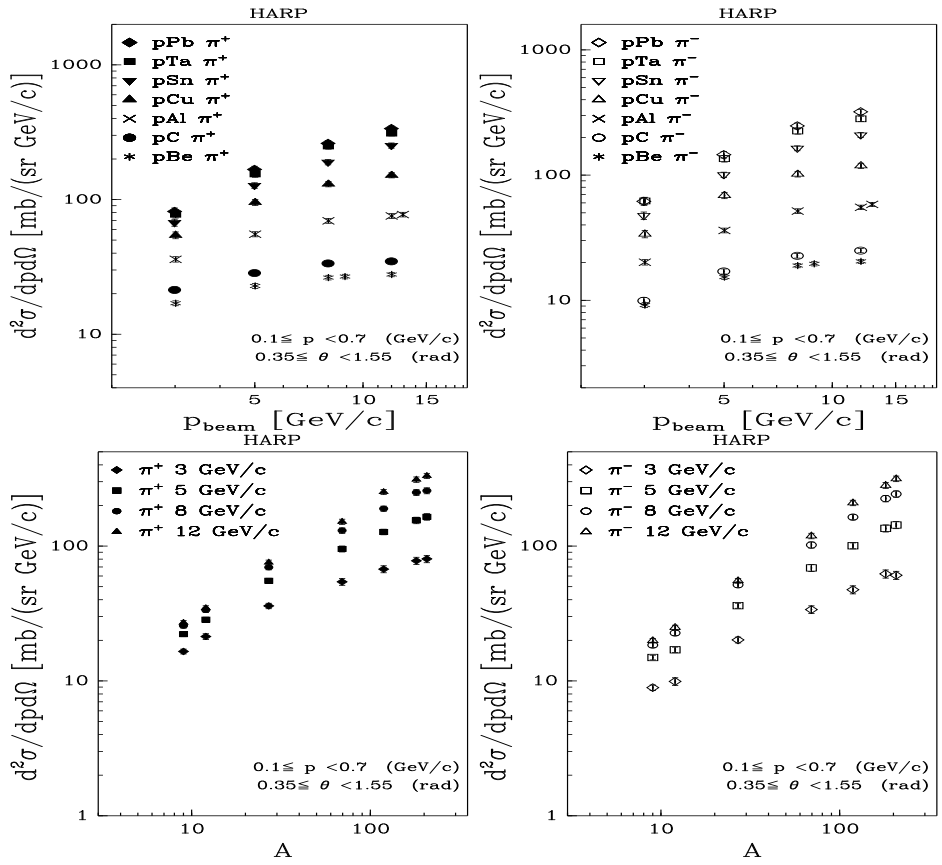

Figure 5: The dependence on the beam momentum and on the atomic number A of the π^- (right) and π^+ (left) production yields in p–Be, p–C, p–Al, p–Cu, p–Sn, p–Ta, p–Pb interactions averaged over the forward angular region (0.350 rad $\leq \theta <$ 1.550 rad) and momentum region 100 MeV/$c \leq p <$ 700 MeV/c. The results are given in arbitrary units, with a consistent scale for all panels.

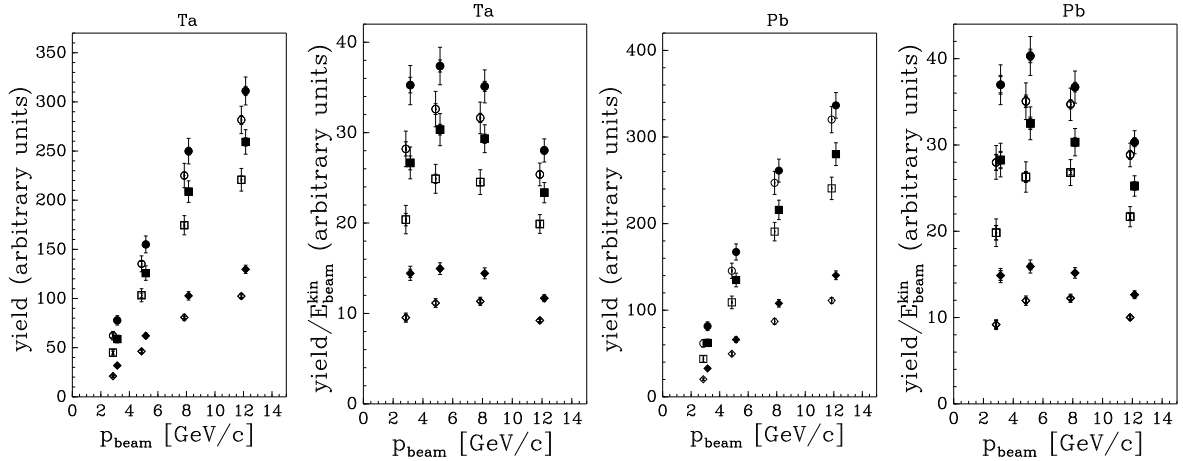

Figure 6: Predictions of the π^+ (closed symbols) and π^- (open symbols) yields for different designs of the neutrino factory focusing stage. Integrated yields and the integrated yields normalized to the kinetic energy of the proton for p–Ta and p–Pb interactions. The circles indicate the integral over the full HARP acceptance (100 MeV/$c <$ $p <$ 700 MeV/c and 0.35 rad $< \theta <$ 1.55 rad), the squares are integrated over 0.35 rad $< \theta <$ 0.95 rad, while the diamonds are calculated for the smaller angular range and 250 MeV/$c < p <$ 500 MeV/c. Although the units are indicated as "arbitrary", for the largest region the yield is expressed as $\mathrm{d}^2\sigma/\mathrm{d}p\mathrm{d}\Omega$ in mb/(GeV/c sr). For the other regions the same normalization is chosen, but now scaled with the relative bin size to show visually the correct ratio of number of pions produced in these kinematic regions.

some models. Discrepancies up to a factor of three are seen. For details see the full paper [17]. The dependence on the beam momentum and on the atomic number A of integrated yields are presented in Fig. 5. Predictions of the π^+ and π^- integrated yields relevant for the design of the neutrino factory focusing stage are given in Fig. 6.

4 Conclusions

The full set of HARP data is in process of publishing now, It covers the pion production by protons and pions on nuclear targets spanning the full periodic table of elements and large solid angle and momentum range in the difficult energy region between 3 and 15 GeV/c of incident momentum. HARP results fill in an essential gap in the available experimental information for soft hadron production and help in the understanding of neutrino fluxes in accelerator neutrino experiments, prediction of atmospheric neutrino fluxes, optimization of a future neutrino factory design and may be used for improvements of the event generators for simulation of hadronic interactions.

Acknowledgments

It is a pleasure to thank the organizers and INFN – Section Bari for the financial support which allowed me to participate in the conference and to present these results on behalf of the HARP Collaboration.

References

1. M.G. Catanesi *et al.* [HARP Collaboration], "Proposal to study hadron production for the neutrino factory and for the atmospheric neutrino flux", CERN-SPSC/99-35 (1999).
2. M.G. Catanesi *et al.* [HARP Collaboration], *Nucl. Instrum. Methods* A **571** (2007) 527.
3. M.H. Ahn *et al.* [K2K Collaboration], *Phys. Rev. Lett.* **90** (2003) 041801.
4. M. H. Ahn *et al.* [K2K Collaboration], *Phys. Rev.* D **74** (2006) 072003.
5. A. A. Aguilar-Arevalo *et al.* [The MiniBooNE Collaboration], arXiv:0704.1500. E. Church *et al.* [BooNE Collaboration], FERMILAB-PROPOSAL-0898, (1997).
6. A. A. Aguilar-Arevalo *et al.* [SciBooNE Collaboration], "Bringing the SciBar detector to the Booster neutrino beam", FERMILAB-PROPOSAL-0954, (2006), [hep-ex/0601022].
7. M. G. Catanesi *et al.* [HARP Collaboration], *Nucl. Phys.* B **732** (2006) 1.
8. M. G. Catanesi *et al.* [HARP Collaboration], *Nucl. Instrum. Methods* A **572** (2007) 899.
9. M. G. Catanesi *et al.* [HARP Collaboration], EPJC **52** (2007) 29.
10. A.A.Aguilar-Arevalo et al., *Phys. Rev. Lett.* **98** (2007) 231801.
11. H. Fesefeldt, report PITHA-85/02, RWTH Aachen, 1985. M. Bleicher *et al.*, J. Phys. G: Nucl. Part. Phys. **25** (1999) 1859. S. Roesler, R. Engel, and J. Ranft, in Proc. of Int. Conf. on Advanced Monte Carlo for Radiation Physics, Particle Transport Simulation and Applications (MC 2000), Lisbon, Portugal, 23-26 Oct 2000, A. Kling, F. Barao, M. Nakagawa, L. Tavora, P. Vaz eds., Springer-Verlag Berlin, p. 1033-1038 (2001).
12. M. G. Catanesi *et al.* [HARP Collaboration], DOI: 10.1016/j.astropartphys.2008.02.002.
13. V. Ammosov *et al.*, *Nucl. Instrum. Methods* A **571** (2007) 562.
    V. Ammosov *et al.* , *J. Inst.* **3** (2008) P01002.
14. M.G. Catanesi *et al.*, [HARP Collaboration]. *Nucl. Instrum. Methods* A **571** (2007) 564.
    A. Artamonov *et al.*, *J. Inst.* **2** (2007) P10004,
15. M.G. Catanesi *et al.*, [HARP Collaboration], *Eur. Phys. J.* C **51** (2007) 787.
16. M. G. Catanesi *et al.*, [HARP Collaboration]. *J. Inst.* **3** (2008) P04007.
17. M.G. Catanesi *et al.*, [HARP Collaboration], "Large-angle production of charged pions in the HARP experiment with incident protons on nuclear targets", *to be publ. in Phys.Rev.C.*
18. M.G. Catanesi *et al.*, [HARP Collaboration]. *Eur. Phys. J.* C **53** (2008) 177.
    M.G. Catanesi *et al.*, [HARP Collaboration]. *Eur. Phys. J.* C **54** (2008) 37.

LOW ENERGY EFFECTS OF SEESAW NEUTRINO MASS MODELS

T. HAMBYE
Service de Physique Théorique, Université Libre de Bruxelles, 1050 Brussels, Belgium

Seesaw models all lead to the same universal dimension 5 low-energy effective operator. As a result effects of this lepton number violating operator, including neutrino masses, cannot distinguish these models. However, effects of the dimension 6 operators, which conserve lepton number and differ for each model, could. For all seesaw models we perform a general analysis of the structure and phenomenology of dimension 6 operators. We discuss how the associated effects could be within experimental reach if a decoupling between dimension 5 and 6 operator coefficients occurs.

1 Introduction

The experimental observation of non-zero neutrino masses and mixings constitutes evidence for physics beyond the Standard Model (SM) and points to the existence of a new, yet unknown, physics scale. If this scale, M, is larger than the electroweak scale, the low energy effects of this new physics can be phrased in terms of a generic effective theory, order by order in $1/M$. At lowest order in this expansion, $\mathcal{O}(1/M)$, the symmetries and particle content of the standard model allow only one operator

$$\delta\mathcal{L}^{d=5} = \frac{1}{2}\, c_{\alpha\beta}^{d=5} \left(\overline{\ell_{L\alpha}^{c}}\tilde{\phi}^{*}\right)\left(\tilde{\phi}^{\dagger}\,\ell_{L\beta}\right) + \text{h.c.} \tag{1}$$

where ℓ_L stands for the lepton weak doublets, greek letters denote flavour indices and $\tilde{\phi}$ is related to the standard Brout-Englert-Higgs (Higgs for short) doublet $\phi \equiv (\phi^+, \phi^0)$ by $\tilde{\phi} = i\tau_2\phi^*$. This dimension 5 operator has the particularity to induce Majorana neutrino masses once the Higgs acquires a vacuum expectation value: $m_\nu = -\frac{v^2}{2}c^{d=5}$, with $\langle\phi^0\rangle = v/\sqrt{2} = 174$ GeV. This means that the neutrino masses, which constitute the first ever observed laboratory evidence for physics beyond the Standard Model, is nothing but the first evidence for physics beyond the Standard Model we could have expected in the $1/M$ expansion. Moreover in such a way

the smallness of the neutrino masses can find a nice explanation: the seesaw mechanism: the neutrino masses are suppressed by $1/M$, so are naturally small if M is large. These facts, as well as the absence of exotic experimental signals other than neutrino masses strongly point for such a heavy scale explanation of the neutrino masses. This leads to the question of how to generate the dimension 5 operator from explicit new physics models. From the tree level exchange of heavy particles there are only 3 basic ways to generate it: through right-handed neutrino exchange (type-I seesaw), scalar Higgs triplet exchange (type-II seesaw) or fermionic triplet exchange (type-III seesaw).[1]

However since the dimension 5 operator is unique, and since one can show that any of these 3 models could generate any flavour structure for the $c_{\alpha\beta}^{d=5}$ matrix, these models cannot be distinguished from it. To distinguish them one must therefore rely on possible effects at next order in the $1/M$ expansion, that is to say from dimension 6 operators, which turn out to be different in each model.

2 Determination of the dimension 6 operators

If the SM is augmented by right-handed neutrinos N_R, in full generality there are 3 new terms which can be written

$$\mathcal{L} \ni i\,\overline{N_R}\not{\partial} N_R - \overline{\ell_L}\,\widetilde{\phi}\,Y_N^\dagger\,N_R - \frac{1}{2}\,\overline{N_R}\,M_N\,{N_R}^c + \text{h.c.} \tag{2}$$

with Y_N the Yukawa interactions and M_N the Majorana mass term, i.e. the new physics scale(s). Flavour indices are implicit in these expressions and we will work in a basis in which M_N is a diagonal complex matrix.

Alternatively if the SM is augmented by a scalar triplet with hypercharge 2, $\overrightarrow{\Delta} = (\Delta_1, \Delta_2, \Delta_3)$ related to the charge eigenstates by $\Delta^{++} \equiv \frac{1}{\sqrt{2}}(\Delta^1 - i\Delta^2)$, $\Delta^{+} \equiv \Delta^3$, $\Delta^0 \equiv \frac{1}{\sqrt{2}}(\Delta^1 + i\Delta^2)$, there are 8 new terms which can be written

$$\begin{aligned}\mathcal{L}_\Delta &= \left(D_\mu\overrightarrow{\Delta}\right)^\dagger\left(D^\mu\overrightarrow{\Delta}\right) + \left(\overline{\widetilde{\ell_{\rm L}}}Y_\Delta(\overrightarrow{\tau}\cdot\overrightarrow{\Delta})\ell_{\rm L} + \mu_\Delta\widetilde{\phi}^\dagger(\overrightarrow{\tau}\cdot\overrightarrow{\Delta})^\dagger\phi + \text{h.c.}\right) \\ &- \left\{\overrightarrow{\Delta}^\dagger {M_\Delta}^2\overrightarrow{\Delta} + \frac{1}{2}\lambda_2\left(\overrightarrow{\Delta}^\dagger\overrightarrow{\Delta}\right)^2 + \lambda_3\left(\phi^\dagger\phi\right)\left(\overrightarrow{\Delta}^\dagger\overrightarrow{\Delta}\right) + \frac{\lambda_4}{2}\left(\overrightarrow{\Delta}^\dagger T^i\overrightarrow{\Delta}\right)^2 + \lambda_5\left(\overrightarrow{\Delta}^\dagger T^i\overrightarrow{\Delta}\right)\phi^\dagger\tau^i\phi\right\}\end{aligned} \tag{3}$$

where summation over the $SU(2)$ indices i and flavour indices is assumed, with T^i the 3 by 3 generators of $SU(2)_L$. Particularly important for the neutrino masses are the Y_Δ Yukawa interactions, and the μ_Δ trilinear scalar interaction, which together induce the dimension 5 operator from the exchange of the scalar triplet.

Alternatively if the SM is augmented by hypercharge 0 fermion triplets, $\vec{\Sigma} = (\Sigma^1, \Sigma^2, \Sigma^3)$, related to the charge components by $\Sigma^\pm \equiv \frac{\Sigma^1 \mp i\Sigma^2}{\sqrt{2}}$, $\Sigma^0 \equiv \Sigma^3$, there are 3 new terms which can be written:

$$\mathcal{L}_\Sigma \;=\; i\,\overline{\vec{\Sigma}_R}\not{D}\vec{\Sigma}_R - [\,\frac{1}{2}\overline{\vec{\Sigma}_R}M_\Sigma\vec{\Sigma}_R^c + \overline{\vec{\Sigma}_R}Y_\Sigma(\widetilde{\phi}^\dagger\vec{\tau}\ell_L) + \text{h.c.}\,]\,. \tag{4}$$

Integrating the heavy fields, using a standard procedure whose details can be found in [2], these three models generate the dimension 5 operator, as well as various dimension 6 operators. The structure of these operators as well the form of their coefficients as a function of the various couplings are given in Table 1.

The main features of the dimension 6 operators are the following. In the fermionic seesaw model, type-I and type-III, the (unique) dimension 6 operator is derivative and, once ϕ is replaced by its vev, induces a non flavour diagonal contribution to the kinetic terms of the light leptons. This requires to redefine the light lepton fields by a non-unitary transformation to

Table 1: Coefficients of the $d = 5$ operator, $c^{d=5}$, and $d = 6$ operators and their coefficients, $c^{d=6}$, in the three basic seesaw theories.

Model	Effective Lagrangian $\mathcal{L}_{eff} = c_i \mathcal{O}_i$		
	$c^{d=5}$	$c_i^{d=6}$	$\mathcal{O}_i^{d=6}$
Fermionic Singlet	$Y_N^T \frac{1}{M_N} Y_N$	$\left(Y_N^\dagger \frac{1}{M_N^\dagger} \frac{1}{M_N} Y_N \right)_{\alpha\beta}$	$\left(\overline{\ell_{L\alpha}} \widetilde{\phi} \right) i\not{\partial} \left(\widetilde{\phi}^\dagger \ell_{L\beta} \right)$
Scalar Triplet	$4 Y_\Delta \frac{\mu_\Delta}{M_\Delta^2}$	$\frac{1}{M_\Delta^2} Y_{\Delta\alpha\beta} Y_{\Delta\gamma\delta}^\dagger$	$\left(\overline{\widetilde{\ell_{L\alpha}}} \overrightarrow{\tau} \ell_{L\beta} \right) \left(\overline{\ell_{L\gamma}} \overrightarrow{\tau} \widetilde{\ell_{L\delta}} \right)$
		$\frac{\lvert\mu_\Delta\rvert^2}{M_\Delta^4}$	$\left(\phi^\dagger \overrightarrow{\tau} \widetilde{\phi} \right) \left(\overleftarrow{D_\mu} \overrightarrow{D^\mu} \right) \left(\widetilde{\phi}^\dagger \overrightarrow{\tau} \phi \right)$
		$-2 \left(\lambda_3 + \lambda_5 \right) \frac{\lvert\mu_\Delta\rvert^2}{M_\Delta^4}$	$\left(\phi^\dagger \phi \right)^3$
Fermionic Triplet	$Y_\Sigma^T \frac{1}{M_\Sigma} Y_\Sigma$	$\left(Y_\Sigma^\dagger \frac{1}{M_\Sigma^\dagger} \frac{1}{M_\Sigma} Y_\Sigma \right)_{\alpha\beta}$	$\left(\overline{\ell_{L\alpha}} \overrightarrow{\tau} \widetilde{\phi} \right) i\not{D} \left(\widetilde{\phi}^\dagger \overrightarrow{\tau} \ell_{L\beta} \right)$

get properly normalized and flavour diagonal kinetic terms. This redefinition applied to the gauge interaction terms leads to non flavour diagonal gauge interactions. In the type-I model, only the kinetic term of neutrinos is affected, which can be understood from the fact that only the neutrinos mix with the right-handed neutrinos. Therefore the gauge interactions affected by this redefinition are the ones involving a light neutrino, W-$\bar{l}_i$-ν_j interactions and Z-$\bar{\nu}_i$-ν_j interactions. For the type-III model both neutrino and charged lepton fields must be redefined, both kinetic terms are affected, because both neutrinos and charged leptons mix with the neutral and charged components of the fermion triplets respectively. Consequently non flavour diagonal Z-$\bar{l}_i$-l_j are induced too. This interaction is obtained, in other words, from a l_i-Σ^--l_j transition with the Z attached to any of these three particles. This leads to a very rich rare lepton process phenomenology, as discussed in section 4 below. For the type-II model since the heavy state is a scalar there is no fermion mixing induced, i.e. no non-unitarity effects, but alternatively a four-lepton interaction is induced through simple exchange of the scalar triplet. This also leads to a very rich phenomenology.

3 What about the size of dimension 6 operator effects?

In general, given the size of the neutrino masses, the magnitude of the dimension 6 operator effects is expected far below the sensitivity of present experiments. For example in the type-I model both dim-5 and dim-6 coefficients in Table 1 involve 2 Yukawa couplings so that one could in general expect that $c_{d=6} \simeq c_{d=5}/M_N \sim m_\nu/M_N v^2$ which even for M_N as low as 1 TeV is very suppressed ($m_\nu/M_N \sim 10^{-13}$ in this case). With such coefficient the observation of any rare lepton process is hopeless. However this naive estimate turns out not to be necessarily valid at all. While the dimension 5 operator breaks lepton number, the dimension 6 ones do not. This reflects itself in the fact that both coefficients do not involve the same combinations of the Yukawa couplings even if they both involve 2 Yukawa couplings, see Table 1. As a result there is no symmetry reason why, if the neutrino mass matrix entries, so $c_{d=5}$ coefficients, are suppressed, the $c_{d=6}$ coefficients should also be.

Any scenario which would proceed in the following 2 steps would result in unsuppressed $c_{d=6}$ coefficients even if the $c_{d=5}$ ones do are suppressed: first assume a scenario where lepton number

is conserved with not too large heavy state mass M and with large Yukawa couplings Y. In this case one gets $c_{d=6} \sim Y^2/M^2$ large and $m_\nu = 0$. Then introduce a small source of lepton number violation from a small perturbation parameter μ: this small perturbation will not affect much the dim-6 coefficients but will lead to dimension 5 coefficients naturally suppressed by an extra μ/M factor, one gets $c_{d=5} \sim f(Y)\mu/M^2$, i.e. $m_\nu \sim f(Y)v^2\mu/M^2$, with $f(Y)$ a function of the Yukawa couplings.

This mechanism which we call Direct Lepton number Violation (because the suppression of neutrino masses comes proportionally to a small entry in the numerator rather than from a large entry in the denominator), turns out to be possible in each of the 3 seesaw models. In the type-II model it is straigthforward. Since the neutrino mass and the dim-6 four lepton operator coefficients have already the DLV form from the beginning, see Table 1, the decoupling of both coefficients is automatic. Large dim-6 coefficients require large Y_Δ couplings with not too large scalar triplet mass, while the size of neutrino masses involve another parameter, μ_Δ, which can be taken small to have sufficiently suppressed neutrino masses. Lepton number is conserved if μ_Δ vanishes. In type-I and type-III scenarios the DLV scenario is much less automatic but turns out to be feasible too. For example for the simple case with one light neutrino ν and 2 right-handed neutrinos $N_{1,2}$, assume that the lepton number of these 3 particles is $1, -1, 1$ respectively. In this case lepton number conservation allows two heavy states in the N_1-N_2 sector, from the MN_1N_2 bilinear term, while it also allows a Yukawa interaction of the type $Y\nu N_1\phi$. These 2 terms lead to a non-vanishing dim-6 coefficient which can be large, $c_{d=6} \sim Y^2/M^2$, but they do not lead to any neutrino mass since lepton number is conserved, no matter the size of Y and M. Introduce now a small L violating term, for example of the form μN_2N_2: this leads to neutrino masses of the form $Y^2\mu v^2/M^2$ just as in the DLV framework above. This mechanism for the type-I model is known as the "inverse seesaw" mechanism.[3] It can be generalized to the 3 light neutrino plus 3 heavy neutrino case [4,5,2] and works also for the type-III model just in the same way [2] as in the type-I model. Of course it requires to give up one of the virtue of the canonical GUT seesaw mechanism which is that neutrino masses can be obtained with just enough suppression from assuming heavy states with mass not far from the GUT scale. But adopting a phenomenological point of view that any possible observable effects of the physics at the origin of the neutrino masses should be searched for, it is interesting to study this possibility in details.

4 Phenomenology of dimension 6 operators effects

There is a long list of rare processes which can be induced by dimension 6 operators: rare lepton decays: $\mu \to e\gamma$, $\tau \to \mu\gamma$, $\tau \to e\gamma$, $\mu \to eee$, $\tau \to 3l$,...; deviations to universality of gauge interactions in $W \to l\bar{\nu}$, $\tau \to l\nu\bar{\nu}$, $Z \to l\bar{l}$, $\pi \to l\bar{\nu}$,...; flavour changing Z decays: $Z \to l_i\bar{l}_j$; Z invisible width from $Z \to \nu\bar{\nu}$ decays; correction to the ρ parameter and W mass in type II model;... Since none of these effects has yet been observed this leads to upper bounds on the dim-6 coefficients, that is to say on combinations of Yukawa couplings and heavy state masses. For the type-I model, combining all constraints, we get the following bounds on the coefficients of the unique dim-6 operator in Table 1: [6,2]

$$\frac{v^2}{2}\,|c^{d=6}|_{\alpha\beta} \;=\; \frac{v^2}{2}\,|Y_N^\dagger \frac{1}{|M_N|^2} Y_N|_{\alpha\beta} < \begin{pmatrix} 10^{-2} & 7.0\cdot 10^{-5} & 1.6\cdot 10^{-2} \\ 7.0\cdot 10^{-5} & 10^{-2} & 1.0\cdot 10^{-2} \\ 1.6\cdot 10^{-2} & 1.0\cdot 10^{-2} & 10^{-2} \end{pmatrix} . \tag{5}$$

Similarly for type-III one obtains:

$$\frac{v^2}{2}\,|c^{d=6}|_{\alpha\beta} \;=\; \frac{v^2}{2}\,|Y_\Sigma^\dagger \frac{1}{M_\Sigma^\dagger} \frac{1}{M_\Sigma} Y_\Sigma|_{\alpha\beta} < \begin{pmatrix} 3\cdot 10^{-3} & 1.1\cdot 10^{-6} & 1.2\cdot 10^{-3} \\ 1.1\cdot 10^{-6} & 4\cdot 10^{-3} & 1.2\cdot 10^{-3} \\ 1.2\cdot 10^{-3} & 1.2\cdot 10^{-3} & 4\cdot 10^{-3} \end{pmatrix} . \tag{6}$$

Table 2: Bounds on $Y_{\Delta\, ij}$ from M_W, from tree level $\ell_1^- \to \ell_2^- \ell_3^+ \ell_4^-$ decays and from one loop $l_1 \to l_2 \gamma$ processes.

Process	Constraint on	Bound $\left(\times \left(\frac{M_\Delta}{1\,\mathrm{TeV}} \right)^2 \right)$
M_W	$\lvert Y_{\Delta \mu e} \rvert^2$	$< 7.3 \times 10^{-2}$
$\mu^- \to e^+ e^- e^-$	$\lvert Y_{\Delta \mu e} \rvert \lvert Y_{\Delta ee} \rvert$	$< 1.2 \times 10^{-5}$
$\tau^- \to e^+ e^- e^-$	$\lvert Y_{\Delta \tau e} \rvert \lvert Y_{\Delta ee} \rvert$	$< 1.3 \times 10^{-2}$
$\tau^- \to \mu^+ \mu^- \mu^-$	$\lvert Y_{\Delta \tau \mu} \rvert \lvert Y_{\Delta \mu\mu} \rvert$	$< 1.2 \times 10^{-2}$
$\tau^- \to \mu^+ e^- e^-$	$\lvert Y_{\Delta \tau \mu} \rvert \lvert Y_{\Delta ee} \rvert$	$< 9.3 \times 10^{-3}$
$\tau^- \to e^+ \mu^- \mu^-$	$\lvert Y_{\Delta \tau e} \rvert \lvert Y_{\Delta \mu\mu} \rvert$	$< 1.0 \times 10^{-2}$
$\tau^- \to \mu^+ \mu^- e^-$	$\lvert Y_{\Delta \tau \mu} \rvert \lvert Y_{\Delta \mu e} \rvert$	$< 1.8 \times 10^{-2}$
$\tau^- \to e^+ e^- \mu^-$	$\lvert Y_{\Delta \tau e} \rvert \lvert Y_{\Delta \mu e} \rvert$	$< 1.7 \times 10^{-2}$
$\mu \to e\gamma$	$\lvert \Sigma_{l=e,\mu,\tau} Y_{\Delta\, l\mu}^\dagger Y_{\Delta\, el} \rvert$	$< 4.7 \times 10^{-3}$
$\tau \to e\gamma$	$\lvert \Sigma_{l=e,\mu,\tau} Y_{\Delta\, l\tau}^\dagger Y_{\Delta\, el} \rvert$	< 1.05
$\tau \to \mu\gamma$	$\lvert \Sigma_{l=e,\mu,\tau} Y_{\Delta\, l\tau}^\dagger Y_{\Delta\, \mu l} \rvert$	$< 8.4 \times 10^{-1}$

The bounds in the type-III model are stronger than in the type-I model, especially for the off-diagonal entries. This is due to the fact that, as said above, in the type-III model, unlike in the type-I model, flavour changing processes with charged fermions are generated already at tree level through the Z-$\bar{l}_i$-l_j couplings. In particular the most stringent bound, which is in the μ-e channel, comes from $\mu \to eee$. It is induced at tree level in the type-III model from a μ-Σ^--e transition on a same fermionic line with emission of a Z which decays in an electron pair. In the type-I model this transition can be done only at the one-loop level and leads to a weaker bound than from $\mu \to e\gamma$ (also induced at one-loop). Similarly the two other off-diagonal constraints in Eq. (6) come from $\tau \to \mu^-\mu^+\mu^-$ and $\tau \to e^-e^+e^-$ in the same way, while for the type-I model in Eq. (5) they come from $\tau \to l\gamma$. As for the diagonal entries they come from universality tests. The constraints from $\mu \to e\gamma$ and $\tau \to l\gamma$ in the type-III model have been discussed in this conference by Florian Bonnet [7,8]. A very interesting feature of the type-III model is that it predicts fixed ratios between the $\mu \to eee$ and $\mu \to e\gamma$ rates and similarly for τ decays [7,8]. This offers the opportunity to test the model in a particularly clean way. An interesting bound also arises from μ to e conversion in atomic nuclei.[8] As for the effect of the type-III model to the $g-2$ of the muon, it turns out to be too small to be able to explain the discrepancy between theoretical expectations and experimental data.[9]

Similarly in the type-II model one gets a series of constraints whose most important ones are given in Table. 2. As in the type-III model, $\mu \to eee$ and $\tau \to 3l$ are induced at tree level (from the simple exchange of a scalar triplet) and give the best constraints on the off-diagonal elements.

The general trend for the bounds above is that the Yukawa couplings must be smaller than $\sim 10^{-1} \cdot (M/1\ \mathrm{TeV})$ or smaller in some cases. Note that these bounds already basically exclude the possibility to produce the heavy states at LHC through Yukawa driven processes even for mass below the LHC energies, see also the discussion by F. del Aguila in this conference [10,11]. Drell-Yan pair production of type-II and type-III heavy states is nevertheless perfectly possible

if they are light enough. If all couplings were of order unity the bounds above translate in a lower bound for the masses of the heavy states: $M_N > 21$ TeV, $M_\Delta > 294$ TeV and $M_\Sigma > 170$ TeV. More details can be found in [2,8].

5 Summary

Rare processes associated to dimension 6 operator effects present a unique opportunity for distinguishing seesaw neutrino mass models, especially if the heavy states are too heavy to be produced at colliders. Although in general these effects are expected to be far from being within experimental reach, it is not excluded that they might be large enough to be reachable soon in special cases. Such cases can be justified within the (common to all seesaw models) Direct Lepton number Violation theoretical framework, based on the assumption of approximate lepton number conservation. The associated phenomenology is very rich and leads, through a long series of processes, to the Yukawa couplings upper bounds given in section 4. This provides a strong motivation for the new generation of experiments aiming to measure rare leptonic processes.[12]

Acknowledgments

This work has been done in collaboration with A. Abada, F. Bonnet, C. Biggio and B. Gavela. We thank the FNRS-FRS, as well as the Comunidad Autónoma de Madrid through Proyecto HEPHACOS; P-ESP-00346, for support.

References

1. See references in [2].
2. A. Abada, C. Biggio, F. Bonnet, B. Gavela and T. Hambye, JHEP 0712 (2007) 061.
3. M. C. Gonzalez-Garcia and J. W. F. Valle, Phys. Lett. B **216** (1989) 360.
4. J. Kersten and A . Y. Smirnov, Phys. Rev. **D76** (2007) 073005.
5. J. Kersten, these proceedings.
6. S. Antusch, C. Biggio, E. Fernandez-Martinez, M. B. Gavela and J. Lopez-Pavon, JHEP **0610** (2006) 084 [arXiv:hep-ph/0607020].
7. F. Bonnet, these proceedings, arXiv:0805.2506 [hep-ph].
8. A. Abada, C. Biggio, F. Bonnet, B. Gavela and T. Hambye, arXiv:0803.0481 [hep-ph].
9. C. Biggio, arXiv:0806.2558 [hep-ph].
10. F. del Aguila, J. A. Aguilar-Saavedra and R. Pittau, J. Phys. Conf. Ser. **53**, 506 (2006) [arXiv:hep-ph/0606198].
11. F. del Aguila, J. A. Aguilar-Saavedra, J. de Blas and M. Perez-Victoria, these proceedings, arXiv:0806.1023 [hep-ph].
12. E.g. Stefan Ritt (for the MEG collaboration), Nucl. Phys. (Proc. Suppl) **B162** (2006) 279; A. J. Bevan, Nucl. Phys. Proc. Suppl. **170** (2007) 323 [arXiv:hep-ex/0611031]; A. G. Akeroyd *et al.* [SuperKEKB Physics Working Group], arXiv:hep-ex/0406071; M. Bona *et al.*, arXiv:0709.0451 [hep-ex]; The Prime working group, http://psux1.kek.jp/jhf-np/LOIlist/LOIlist.html

NEUTRINOLESS DOUBLE BETA DECAY SEARCH WITH CUORICINO AND CUORE EXPERIMENTS

M. VIGNATI
(for the CUORE and CUORICINO Collaborations)
University of Rome "La Sapienza" and Sezione di Roma dell' INFN
Roma I-00185, Italy.

CUORICINO is a bolometric experiment on Neutrinoless Double Beta Decay (0ν-DBD) . With its 40.7 kg mass of TeO_2 it is the most massive 0ν-DBD presently running and it has proven the feasibility of the CUORE experiment, whose aim is to be sensitive to the effective neutrino mass down to few tens of meV. We report here latest CUORICINO results and prospects for the future CUORE experiment.

1 Introduction

The positive results obtained in the last few years in neutrino oscillation experiments have given convincing and model indipendent evidences that neutrinos are massive and mixed particles. The obtained data are compatible with two possible mass patterns, or hierarchies, the normal: $m_1 < m_2 \ll m_3$, and the inverted hierarchy: $m_3 \ll m_1 < m_2$. Unfortunately oscillation experiments are only sensitive to neutrino mass squared differences and cannot give any information about neutrino nature (Dirac or Majorana particle) and absolute mass scale. Beta decay experiments are sensitive to the absolute mass scale but cannot determine neutrinos nature. Experiments looking for the Neutrinoless Double Beta Decay (0ν-DBD) of even-even nuclei have the highest sensitivity to the effective neutrino mass ($m_{\beta\beta}$) and to the neutrino nature. A positive signal would imply that neutrino are Majorana particles and can even lead to the measure of the absolute mass scale.

The use of the bolometric technique offers the unique possibility to investigate different 0ν-DBD candidates with a considerable high energy resolution, needed to separate the 2ν contribution from the 0ν peak. The CUORE experiment [1], to search 0ν-DBD of ^{130}Te, will start its assembling phase in 2008 and it aims to reach a sensitivity on $m_{\beta\beta}$ better than 50 meV.

CUORICINO [2] represent not only the first stage of CUORE, but also the most massive 0ν-DBD experiment presently running.

2 Bolometric Technique

Bolometers are sensitive calorimeters that measure the energy deposited by particle or photon interactions by measuring the corresponding rise in temperature. The CUORICINO bolometers are single crystals of TeO_2 that are dielectric and diamagnetic. In these materials the heat capacity is due almost exclusively to the lattice degrees of freedom and its value at 10 mK ($\sim 2 \times 10^{-9} \mathrm{J \cdot K^{-1}}$) has been extrapolated from the measured value at 232 K. With these values of the parameters, an energy deposition of a few keV will result in a measurable temperature increase of the crystal ($\sim$ 0.2 mK/MeV). In CUORICINO the crystal temperature variations are measured by thermistors glued to each crystal that, in order to obtain usable signals for such small temperature changes, have to be very sensitive.
The thermistors are heavily doped high-resistance germanium semiconductors with an impurity concentration slightly below the metal-insulator transition. High quality thermistors require a very homogeneous doping concentration: CUORICINO uses Neutron Transmutation Doped (NTD) germanium thermistors, this is achieved by means of uniform thermal neutron irradiation throughout the entire volume in a nuclear reactor. The electrical conductivity of these devices, which is due to variable range hopping (VHR) of the electrons, depends very sensitively on the temperature. The resistance varies with temperature according to $R = R_0 \exp(\frac{T_a}{T})^{\gamma}$, where R_0 and T_a depend on the doping concentration and $\gamma = 1/2$.

3 Cuoricino Setup

CUORICINO is an array of 62 crystals of TeO_2 with a total active mass of 40.7 kg, that corresponds to a mass of ^{130}Te of $\sim$ 11 kg. The tower is located inside the cryostat situated in the Hall A of Laboratori Nazionali del Gran Sasso (LNGS) of INFN. CUORICINO's 62 crystals are arranged in a tower made by 13 planes (Figure 1), 11 of them are filled with 4 cubes of 5 cm side while the other two with 9 crystals 3×3×6 cm^3 each. Four 3×3×6 cm^3 crystals are enriched, two of which in ^{128}Te, 82.3 % isotopic abundance, and the other two in ^{130}Te, isotopic abundance of 75 %.

All the materials composing the detector were selected to be low contaminated with radioactive isotopes. To avoid external vibrations to reach the detectors the tower is mechanically decoupled from the cryostat through a steel spring. In order to shield against the radioactive contaminants from the materials of the refrigerator, a 1.2 cm shield of Roman lead with ^{210}Pb activity less than mBq/kg is framed around the array to reduce the activity of the thermal shields. The cryostat is externally shielded by means of two layers of lead of 10 cm minimal thickness each. The background due to environmental neutrons is reduced by a layer of Borated Polyethylene of 10 cm minimum thickness. The refrigerator operates inside a Plexiglas anti-radon box flushed with clean N_2 and inside a Faraday cage to reduce electromagnetic interferences. CUORICINO is operated at a temperature of $\sim$ 8 mK with a spread of $\sim$ 1 mK. The energy calibration is performed before and after each subset of runs, which lasts about a month, by exposing the array to two thoriated tungsten wires inserted in immediate vicinity of the refrigerator.

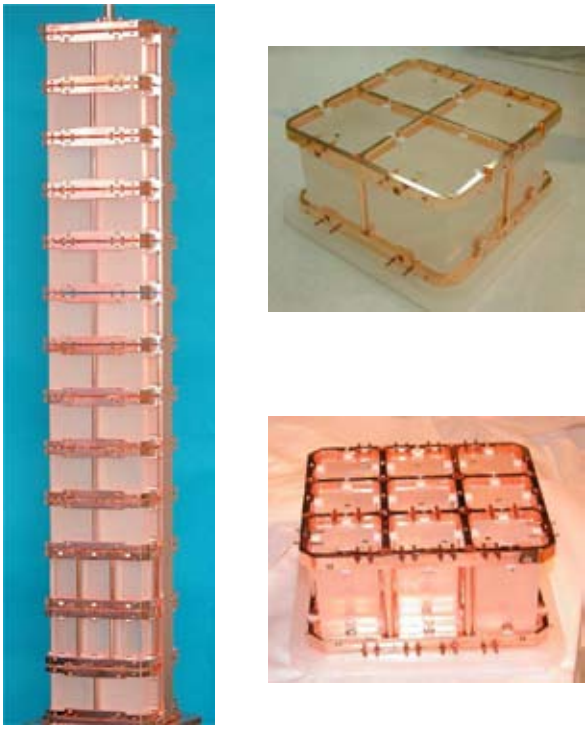

Figure 1: CUORICINO array (left) and details of the planes hosting the $5 \times 5 \times 5$ cm^3 crystals (top right) and $3 \times 3 \times 6$ cm^3 crystals (bottom right)

4 Cuoricino Results

CUORICINO first measurement started in March 2003 and ended in of October 2003. After a substantial operation of maintenance in April 2004 the second run of CUORICINO started. The average resolution FWHM is 7.5 ± 2.9 keV for the bigger size and of 9.6 ± 3.5 keV for the small size crystals. The duty cycle of the experiment, since August 2004 is ∼ 73 %. Discarding the time needed for energy calibration measurement (3 days every 3–4 weeks) the total live time is 63 %. The background spectra collected up to Aug 2007, corresponding to a total statistic of 15.53 kg (^{130}Te) ·year , is presented in figure 2. Apart the ^{60}Co sum line, no other unexpected peak is found near the 2530 keV 0νDBD region of ^{130}Te. The background level is 0.18 ± 0.01 c/keV/Kg/y and the corresponding lower limit on the 0νDBD of ^{130}Te is $3.1\times\ 10^{24}$ y (90% C.L.). This limit leads to a constraint on the electron neutrino effective Majorana mass ranging from 0.20 to 0.68 eV, depending on the nuclear matrix elements considered in the computation.

5 The Cuore Experiment

The CUORE detector will consist of an array of 988 TeO_2 bolometers arranged in a cylindrical configuration of 19 towers containing 52 crystals each (Figure 3), for a total mass of ∼741 kg. Each of these towers is a CUORICINO-like detector consisting of 13 modules, 4 detectors each. Assuming a background of B=0.01 c/keV/kg/y, achievable with a slight improvement of the current available material selection and cleaning techniques, and an energy resolution Γ(2.5 MeV)=5 keV, we get a sensitivity $S_{0\nu}$ on the half life (90 % C.L.) of $5.8\cdot\ 10^{25}\sqrt{t}$ years ($4.1\cdot\ 10^{25}\sqrt{t}$ years for Γ=10 keV), which in 5 years of statistics would provide $m_{\beta\beta}$ bounds in the range 0.024–0.13 eV. However, the R&D to be carried out in CUORE, if successful, would provide a value of B∼ 0.001 c/keV/kg/y, i.e. a detection sensitivity of $S_{0\nu}\sim\ 1.86\cdot\ 10^{26}\sqrt{t}$ years

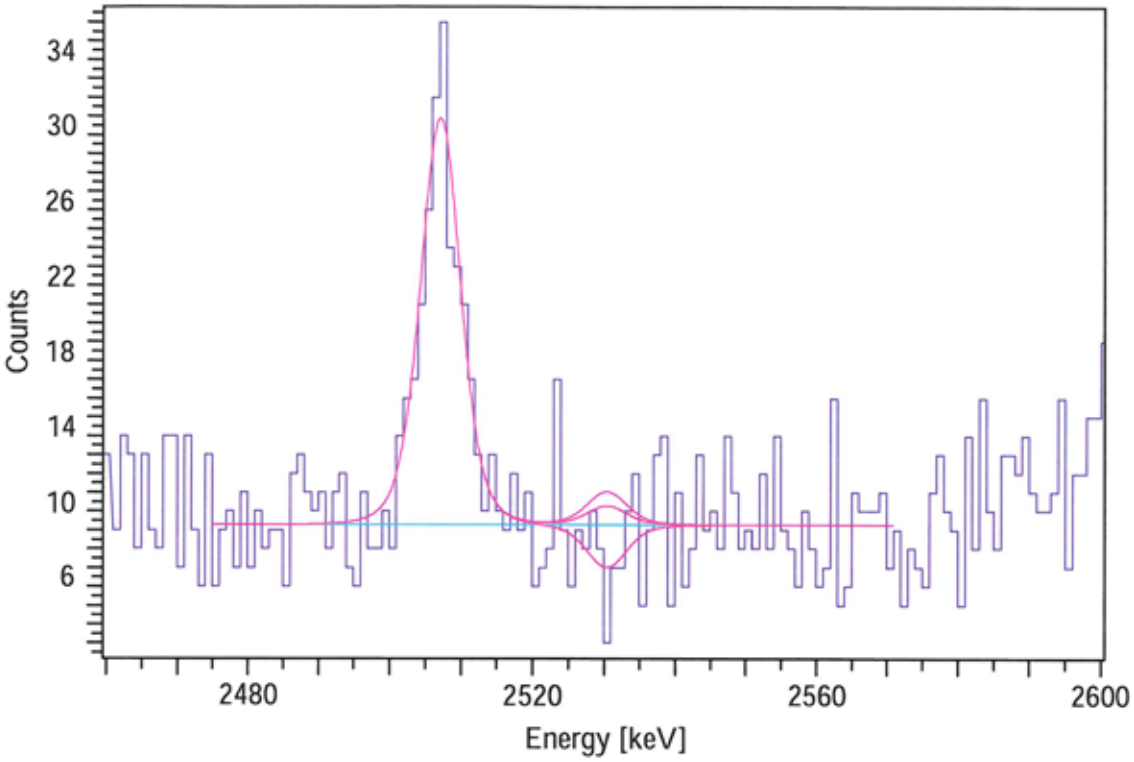

Figure 2: CUORICINO spectrum in the $0\nu\beta\beta$ region

(1.2· $10^{26}\sqrt{t}$ years for Γ=10 keV), or $m_{\beta\beta}$ bounds in the range ∼ 0.016–0.085 eV in 5 years. TeO_2 crystals made with ^{130}Te enriched material have been already operated in MiDBD and CUORICINO, making an enriched CUORE a feasible option. Assuming a 95% enrichment in ^{130}Te and a background level of B=0.001 c/keV/kg/y, the sensitivity would become $S_{0\nu}\sim 8.32\cdot10^{26}\sqrt{t}$ years. For an exposure of 5 years, the corresponding $m_{\beta\beta}$ bounds would range from 8 meV to 45 meV depending on the nuclear matrix element calculations.

References

1. C. Arnaboldi *et al.*, Nucl. Instrum. Meth. A **518** (2004) 775
2. C. Arnaboldi *et al.*, Submitted to Phys. Rev. C, arXiv:0802.3439 [hep-ex].

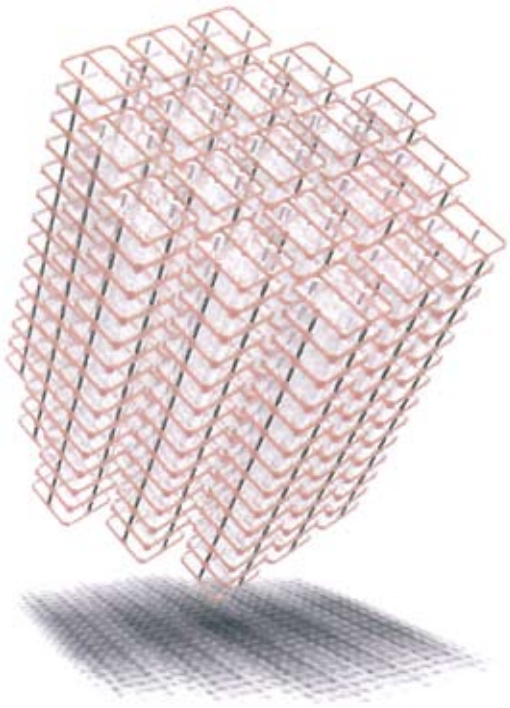

Figure 3: CUORE detector: the bolometers array is made of 19 CUORICINO like towers

SEARCH FOR NEUTRINOLESS DOUBLE BETA DECAY IN ^{150}Nd WITH THE NEMO3 EXPERIMENT

GWENAELLE BROUDIN-BAY ON BEHALF OF THE NEMO COLLABORATION
Laboratoire de l'Accélérateur Linéaire,
Université Paris-Sud 11, CNRS/IN2P3, Bâtiment 200,
91898 Orsay cedex, France

The double beta decay experiment NEMO3 has been taking data since February 2003. The aim of the experiment is to search for neutrinoless double beta decay with 10 kg of enriched isotopes. Using 939 days of data, a preliminary result was obtained for ^{150}Nd: $T^{2\nu}_{1/2} = (9.20^{+0.25}_{-0.22}(stat.) \pm 0.62(syst.)) \times 10^{18}$ y. No neutrinoless double beta decay signal was observed and a limit on the half-life of the process was set to $T^{0\nu}_{1/2} > 1.8 \times 10^{22}$ y at 90% confidence level. An overview of the results previously obtained for other isotopes is also given.

1 Introduction

Neutrinoless double beta decay ($0\nu\beta\beta$) for a nucleus of atomic number A and charge Z is the process: $(A, Z) \rightarrow (A, Z+2) + 2e^-$. The process belongs to physics beyond the Standard Model as it violates the conservation of the total lepton number. Its observation would prove that the neutrino is a Majorana particle. Neutrinoless double beta decay may occur through several mechanisms, among which the decay with light neutrino exchange that would grant access to the mass scale. The half-life of the $0\nu\beta\beta$ process is then given by:

$$(T^{0\nu}_{1/2})^{-1} = |M^{0\nu}(A, Z)|^2 G^{0\nu}(Q, Z) \langle m_\nu \rangle^2 \quad (1)$$

with $M^{0\nu}(A, Z)$ a nuclear matrix element (NME) obtained from theoretical calculations, $G^{0\nu}(Q, Z)$ a phase space factor depending on the Q value of the process, and $\langle m_\nu \rangle$ the effective mass of the neutrino. This effective mass is given by $\langle m_\nu \rangle = \sum_{i=1}^{3} U^2_{ei} m_i$ where U_{ei} stands for the squared elements of the PMNS matrix and m_i the mass associated to the mass eigenstate i.

2 The NEMO3 experiment

2.1 The NEMO3 detector

The NEMO3 experiment has been taking data since February 2003. The detector is located in the Modane Underground Laboratory (LSM) under a rock cover of 4800 m water equivalent. It accommodates 10 kg of double beta emitter foils. With its cylindrical geometry, the NEMO3 detector is divided into 20 sectors in the middle of which the foils were installed. The main isotopes used for the search of the neutrinoless double beta decay are ^{100}Mo (~7 kg) and ^{82}Se (~1 kg). Smaller amount of other isotopes are also used to study the two-neutrino double beta

Table 1: Isotopes in the NEMO3 detector.

	^{100}Mo	^{82}Se	^{116}Cd	^{150}Nd	^{96}Zr	^{48}Ca	^{130}Te	^{nat}Te	Cu
Mass (g)	6914	932	405	36.6	9.4	7.0	454	491	621
$Q_{\beta\beta}(keV)$	3034	2995	2805	3367	3350	4772	2529		

decay ($2\nu\beta\beta$) process. The sectors containing the natural tellurium and the copper foils are dedicated to the background measurement. The mass of each isotope within the detector is summarized in Table 1.

The principle of the NEMO3 detector is the identification of the electrons in a double beta decay process and the measurement of their individual energy. Therefore, a tracking chamber is associated to a calorimeter. The tracking volume consists of 6180 drift cells operated in Geiger mode. It allows the reconstruction of the trajectory of charged particles and the determination of the position of the vertex with a resolution of 5 mm tranversely to the source foil plane and 8 mm longitudinally. A 25 Gauss magnetic field is generated by a coil surrounding the detector and allows the identification of the charge of the particles. The drift gas inside the tracking volume is helium with added ethyl alcohol (4%), argon (1%) and water (0.1%). The calorimeter consists of 1940 photomultiplier tubes associated to plastic scintillator blocks. The energy resolution ranges from 14.1% to 17.7% for 1 MeV electrons. The time resolution is 250 ps. The tracker - calorimeter association allows to identify electrons, positrons, gammas and alpha particles as well as to measure their time of flight. The detector is protected from gammas by an iron shielding, and from neutrons present inside the laboratory by wood and a borated water shielding. A tent coupled to a radon-free air factory surrounds the detector. A detailed description of the detector was published in [1].

2.2 Background model

The background sources can be classified into three groups: the external background from incoming γ, the radon present inside the tracker volume and the internal background from radioactive contamination of the sources. The activities of theses background sources can be obtained through the use of a set of control channels corresponding to different event topologies on the NEMO3 data. These measured activities were compared to measurements performed with HPGe and radon detectors.

At the beginning of the experiment, the radon inside the tracking chamber, and more precisely the decay product ^{214}Bi present in its radioactive chain, was found to be the predominant background source. Radon is present in the air of the laboratory as it originates from the rock surrounding it and can penetrate inside the detector through small leaks. A tent coupled to radon-free air factory was then installed around the detector in October 2004 in order to decrease the presence of radon inside the tracker. The data taken before that date are referred to as Phase I data. After October 2004, the data are Phase II data.

3 NEMO3 results

3.1 $2\nu\beta\beta$ decay of ^{150}Nd

Measurements of the $2\nu\beta\beta$ half-life can be performed for 7 isotopes in the NEMO3 experiment. This process is the following: $(A, Z) \rightarrow (A, Z+2) + 2e^- + 2\bar{\nu}_e$. It constitutes the ultimate background in the $0\nu\beta\beta$ search because of the energy resolution of the detector.

The $\beta\beta$ type events are selected by requiring two tracks with a curvature compatible with a negative charge. Each track is associated to a separate energy deposit in the calorimeter greater

than 200 keV. Both track should originate from a common vertex located inside the source foil. The time of flight measurement for both electrons must be consistent with the hypothesis that they were emitted from the foil.

A preliminary measurement of the half-life of ^{150}Nd was obtained for a 36.6 g sample from data collected between February 2003 and December 2006, corresponding to 939 days of data taken during the Phases I and II of the experiment. A total of 2828 $\beta\beta$ type events were observed with a signal-over-background ratio of 2.7. The distribution of the energy sum of the electrons in $\beta\beta$ type events and the angle between them are shown in Fig. 1. The background substracted data and the $2\nu\beta\beta$ signal expectation obtained from Monte-Carlo are in good agreement. The $2\nu\beta\beta$ selection efficiency is 7.2%. The measured half-life is $T^{2\nu}_{1/2} = (9.20^{+0.25}_{-0.22}(stat.) \pm 0.62(syst.)) \times 10^{18} y$. This value is in between two previous results obtained from experiments led using time projection chambers [2,3].

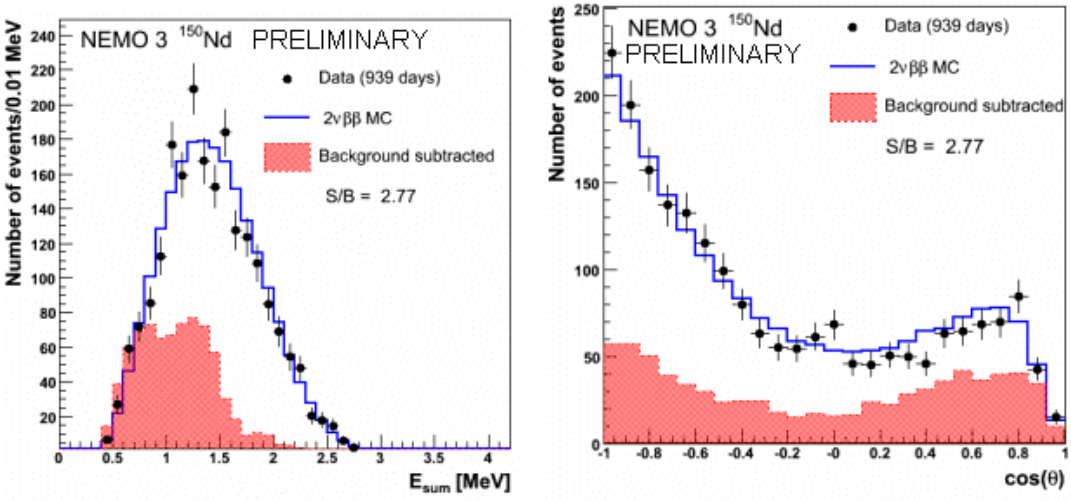

Figure 1: Distribution of the energy sum of the two electrons E_{sum} (left graph) and the angle between the two electrons $cos\theta$ (right graph), background substracted. The data are shown as points and the substracted background as a red histogram.

3.2 $2\nu\beta\beta$ decay of other isotopes

The half-life of the $2\nu\beta\beta$ process for the other isotopes inside NEMO3 was measured using the data from Phase I or combined Phases I and II and the preliminary results are given in Table 2. These results are important for nuclear theory as they help constrain the nuclear models and thus improve the NME calculations. The NME are a source of uncertainty when translating the half-lives of the $0\nu\beta\beta$ into effective neutrino masses.

3.3 Search for neutrinoless double beta decay of ^{150}Nd

A $0\nu\beta\beta$ decay signal would correspond to an excess of $\beta\beta$ type events around the energy of the transition $Q_{\beta\beta}$ in the distribution of the energy sum of the electrons. Indeed, the theoretical peak at $Q_{\beta\beta}$ would be smeared out by the energy resolution of the calorimeter. For ^{150}Nd, the $Q_{\beta\beta}$ value is 3.367 MeV. Fig. 2 shows that no excess of events in the distribution of the energy sum of the electrons for the $\beta\beta$ type events originating from the ^{150}Nd sample is observed for 939 days of data collection. A limit on the half-life of the $0\nu\beta\beta$ process was subsenquently set using the CL_s method [5] for $E_{sum} > 2.5$ MeV. The corresponding $0\nu\beta\beta$ selection efficiency is 19%. The limit on the half-life obtained is $T^{0\nu}_{1/2} > 1.8 \times 10^{22}$ years at 90% confidence level (CL), which translates into an upper limit on the effective Majorana mass of the neutrino in the range

Table 2: Half-lives of $2\nu\beta\beta$ processes measured using Phase I data (360 days). The ^{130}Te results use Phases I and II data (534 days).

Isotope	Signal/Background	$T_{1/2}$ [10^{19} years]
^{100}Mo	40	$0.711 \pm 0.002(stat.) \pm 0.054(syst.)$ [4]
^{82}Se	4	$9.6 \pm 0.3(stat.) \pm 1.0(syst.)$ [4]
^{116}Cd	7.5	$2.8 \pm 0.1(stat.) \pm 0.3(syst.)$
^{96}Zr	1	$2.0 \pm 0.3(stat.) \pm 0.2(syst.)$
^{48}Ca	~ 10	$3.9 \pm 0.7(stat.) \pm 0.6(syst.)$
^{130}Te	0.25	$76 \pm 15(stat.) \pm 8(syst.)$

$\langle m_\nu \rangle < 1.9 - 2.7$ eV according to the NME calculations in [7] and $\langle m_\nu \rangle < 5.4 - 8.5$ eV according to [8]. The limit on the half-life was improved by one order of magnitude compared to the previous result, $T^{0\nu}_{1/2} > 1.7 \times 10^{21}$ years at 90% CL [6].

Along with the light neutrino exchange, other mechanisms can mediate $0\nu\beta\beta$ decay. Among those can be found the models with Majoron emission characterized by a spectral index n and the model with a right-handed (V+A) contribution in the Lagrangian. In the assumption of a $0\nu\beta\beta$ process involving right currents (V+A), the limit on the half-life was found to be $T^{0\nu}_{1/2} > 1.27 \times 10^{22}$ years at 90% confidence level. For a $0\nu\beta\beta$ process with the emission of a Majoron (spectral index $n = 1$) the limit obtained is $T^{0\nu}_{1/2} > 1.55 \times 10^{21}$years at 95% CL.

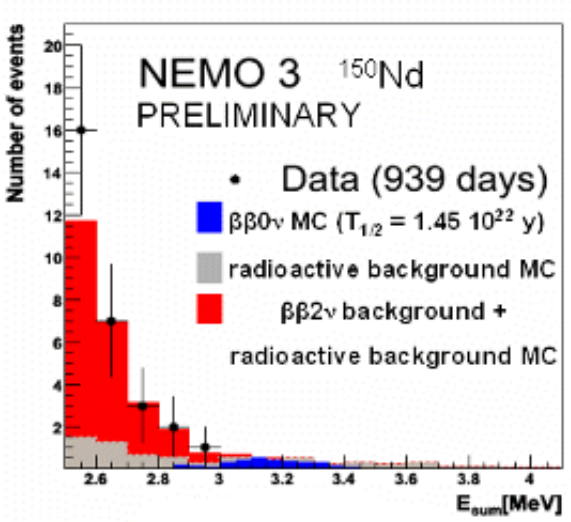

Figure 2: Distribution of the energy sum of the two electrons E_{sum} for $E_{sum} > 2.5$ MeV for data (points) compared to the total background (in red) consisting of the radioactive background (in grey) plus the $2\nu\beta\beta$. A MC simulation of a $0\nu\beta\beta$ signal with a half-life of 1.45×10^{22} years is shown in blue.

3.4 Search for $0\nu\beta\beta$ of ^{100}Mo and ^{82}Se

^{100}Mo and ^{82}Se are the main isotopes in the NEMO3 detector used for the search for neutrinoless double beta decay. For both isotopes, 639 days of data spread over the two phases of the experiment were analyzed. For ^{100}Mo the $Q_{\beta\beta}$ value is 3.034 MeV. No excess of events was found in the $2.8 < E_{sum} < 3.2$ MeV energy window, as 12.1 events are expected from Monte Carlo and 11 were observed. The $0\nu\beta\beta$ selection efficiency is 8.2%, which leads to a limit on the

Table 3: Constraints on $T_{1/2}$ in years (90% CL) for (V+A) and Majoron emission processes from NEMO3 data. λ is a (V+A) Lagrangian parameter and g is a Majoron to neutrino coupling strength.

$0\nu\beta\beta$ process	^{100}Mo	^{82}Se
(V+A) current	$> 3.2 \times 10^{23}$ $\lambda < 1.8 \times 10^{-6}$	$> 1.2 \times 10^{23}$ $\lambda < 2.8 \times 10^{-6}$
$n = 1$	$> 2.7 \times 10^{22}$ $g < (0.4 - 1.8) \times 10^{-4}$	$> 1.5 \times 10^{22}$ $g < (0.7 - 1.9) \times 10^{-4}$
$n = 3$	$> 1.7 \times 10^{22}$	$> 6.0 \times 10^{21}$
$n = 5$	$> 1.0 \times 10^{22}$	$> 3.1 \times 10^{21}$
$n = 7$	$> 7.0 \times 10^{19}$	$> 5.0 \times 10^{20}$

half-life of the $0\nu\beta\beta$ process $T^{0\nu}_{1/2} > 5.8 \times 10^{23}$ years at 90% CL. This translates into an upper limit on the neutrino mass of $\langle m_\nu \rangle < 0.8 - 1.3$ eV using the values of the NME in [9]. The $Q_{\beta\beta}$ value for ^{82}Se is 2.995 MeV. As for ^{100}Mo, no excess of events was found around the $Q_{\beta\beta}$ value in the distribution of the energy sum of the electrons. In the $2.65 < E_{sum} < 3.20$ MeV energy window, 7 events were observed for 6.4 estimated by Monte Carlo simulations. With a 14.4% $0\nu\beta\beta$ selection efficiency, the obtained limit on the half-life is $T^{0\nu}_{1/2} > 2.1 \times 10^{23}$ years at 90% CL. The corresponding upper limit on the mass of the neutrino using [10] is then $\langle m_\nu \rangle < 1.4 - 2.2$ eV. The results obtained for the half-life of the $0\nu\beta\beta$ process of ^{100}Mo and ^{82}Se through the (V+A) and the Majoron mechanisms [11] are summarized in Table 3.

4 Summary

The NEMO3 experiment allows the measurement of $2\nu\beta\beta$ decays with very high statistics. A preliminary result was obtained for the $2\nu\beta\beta$ half-life of ^{150}Nd for a 36.6 g sample: $T^{2\nu}_{1/2} = (9.20^{+0.25}_{-0.22}(stat.) \pm 0.62(syst.)) \times 10^{18}$ years. A limit on the the $0\nu\beta\beta$ half-life of $T^{0\nu}_{1/2} > 1.8 \times 10^{22}$ years was estimated at 90 % confidence level. The $Q_{\beta\beta}$ value of ^{150}Nd is one of the highest among $\beta\beta$ emitters and lies above the typical energies of many background sources. Also, that isotope has a large phase space factor. These characteristics make ^{150}Nd a promising candidate for the SuperNEMO experiment aiming at a sensivity of 50 meV on the Majorana neutrino mass with 100 kg of enriched isotopes. The enrichment process is currently under study by the Nd-150 collaboration for the SuperNEMO and SNO++ projects.

References

1. R. Arnold et al., Nucl. Instr. Meth. A 536 (2005) 79.
2. V. Artemiev et al., Phys. Let. B, 345, (1995), 564.
3. A. De Silva et al., Phys. Rev. C 56 (1997) 2451.
4. R. Arnold et al., Phys. Rev. Lett. 95 182302 (2005).
5. W. Fisher, FERMILAB-TM 2386-E (2007).
6. A. A. Klimenko et al., Nucl. Instr. Meth. B17 (1986) 445.
7. V. A. Rodin et al., Nucl. Phys. A 793 (2007) 231.
8. J. G. Hirsch et al., Nucl. Phys. A 582 (1995) 124.
9. V. A. Rodin et al., Nucl. Phys. A 793, (2007) 213; F. Simkovic et al., Phys. Rev. C 60, 055502 (1999) ; M. Aunola et al., Nucl. Phys. A 643, 207 (1998) ; J. Suhonen et al., Nucl. Phys. A 273, 271 (2003) ; S. Stoica et al., Nucl. Phys. A 694, 269 (2001).
10. V. A. Rodin et al., Nucl. Phys. A 793, (2007) 213; M. Kortelainen and J. Suhonen, Phys.

Rev. C 75, (2007) 051303(R); M. Kortelainen and J. Suhonen, Phys. Rev. C 75, (2007) 024315.
11. R. Arnold et al., Nucl. Phys. A 765 (2006) 483.

LHC TEST OF THE SEE-SAW [a]

J. KERSTEN
The Abdus Salam ICTP, Strada Costiera 11, 34014 Trieste, Italy

We discuss the prospects for detecting right-handed neutrinos which are introduced in the see-saw mechanism at future colliders. This requires a very accurate cancellation between contributions from different right-handed neutrinos to the light neutrino mass matrix. We search for possible symmetries behind this cancellation and find that they have to include lepton number conservation. Light neutrino masses can be generated as a result of small symmetry-breaking perturbations. The impact of these perturbations on LHC physics is negligible, so that the mechanism of neutrino mass generation and LHC physics are decoupled in general. In constrained cases, accelerator observables and neutrino masses and mixings can be correlated.

1 Introduction

The (type-I) see-saw mechanism [2,3,4,5,6] generates small neutrino masses in a natural way, introducing right-handed (RH) neutrinos that are singlets under the Standard Model (SM) gauge group and can therefore have large Majorana masses. The light neutrino mass matrix is approximately given by

$$m_\nu = -m_{\rm D} m_{\rm R}^{-1} m_{\rm D}^T \,, \tag{1}$$

where $m_{\rm D}$ is the Dirac mass matrix and $m_{\rm R}$ is the Majorana mass matrix of the heavy singlets. A direct test of the see-saw mechanism requires the detection of these heavy neutrinos and the measurement of their Yukawa couplings. Using Eq. (1) in the case of only one generation and $m_\nu \sim 0.1$ eV, we obtain the estimate $m_{\rm R} \sim 10^{14}$ GeV, if the Dirac neutrino masses are close to the electroweak scale. The singlets may have masses as small as 100 GeV, within the energy reach of the LHC and other future colliders, if the Dirac masses are a bit smaller than the electron mass, which does not appear completely unreasonable either. However, the RH

[a] Talk presented at the XLIIIrd Rencontres de Moriond, March 1–8, 2008, La Thuile, Italy. Based on work done in collaboration with Alexei Smirnov [1].

neutrinos interact with the SM particles only via Yukawa couplings,[b] which are tiny in this case. Thus, we expect the RH neutrinos to be either way too heavy or way too weakly coupled to be observable at colliders.

However, this conclusion can be avoided provided that there are two or more RH neutrinos [7,8,9,10,11,12,13,14,15,16,17,18,19,1,20]. Their contributions to the light neutrino masses can cancel, opening up the possibility of rather light singlets with large Yukawa couplings but exactly vanishing light neutrino masses. Non-vanishing masses are generated by small perturbations of the cancellation structure. In this setup, the RH neutrinos may be observable in future collider experiments. This possibility has attracted renewed interest recently, see e.g. [21,22,23,24,25,26,20].

In the following, we will discuss the prospects for discovering RH neutrinos at colliders from the point of view of theory. We will consider the cancellation of contributions to the light neutrino mass matrix and possible underlying symmetries in the next section. After briefly discussing small perturbations of the leading-order mass matrices that yield viable masses for the light neutrinos, we will turn to consequences for signatures at colliders. Within the setups relying on a symmetry, lepton number violation is unobservable, while lepton-flavour-violating processes can have sizable amplitudes. Finally, we will comment on the implications a detection of RH neutrinos would have for our understanding of the mechanism of neutrino mass generation.

2 Cancellations and Symmetries

2.1 Vanishing Light Masses

For three generations of left- and right-handed neutrinos, the contributions of the RH neutrinos to the light mass matrix cancel exactly, if and only if [10,13,14,1,27] the Dirac mass matrix has rank 1,

$$m_{\rm D} = m \begin{pmatrix} y_1 & y_2 & y_3 \\ \alpha y_1 & \alpha y_2 & \alpha y_3 \\ \beta y_1 & \beta y_2 & \beta y_3 \end{pmatrix} , \tag{2}$$

and if

$$\frac{y_1^2}{M_1} + \frac{y_2^2}{M_2} + \frac{y_3^2}{M_3} = 0 \, , \tag{3}$$

where M_i are the singlet masses. The mass parameters are defined in the basis where the singlet mass matrix is diagonal. The case of two RH neutrinos is analogous [9,11,12], while for four or more RH neutrinos there are additional possibilities. The cancellation is valid to all orders in $m_{\rm D} m_{\rm R}^{-1}$. The overall scale of the Yukawa couplings is not restricted by the cancellation condition (3) and hence allowed to be large enough to make the detection of RH neutrinos possible. The only relevant constraint is the experimental bound on the mixing

$$V = m_{\rm D} m_{\rm R}^{-1} \tag{4}$$

between active and singlet neutrinos, [28]

$$\sum_i |V_{\alpha i}|^2 \lesssim 10^{-2} \quad (\alpha = e, \mu, \tau) \, . \tag{5}$$

2.2 Underlying Symmetries

Without a symmetry motivation, the cancellation condition (3) amounts to severe fine-tuning and is unstable against radiative corrections. Let us therefore discuss symmetries leading to the

[b] This is the case in the minimal extension of the SM we consider here. Of course, the situation is very different if the RH neutrinos have additional interactions, for example with TeV-scale $\mathrm{SU}(2)_{\rm R}$ gauge bosons.

cancellation. We will restrict ourselves to the case of three singlets. A well-known possibility is imposing lepton number conservation [7,8,15,17,18]. The assignment $L(\nu_{\rm L}) = L(\nu_{\rm R}^1) = -L(\nu_{\rm R}^2) = 1$, $L(\nu_{\rm R}^3) = 0$ implies

$$m_{\rm R} = \begin{pmatrix} 0 & M & 0 \\ M & 0 & 0 \\ 0 & 0 & M_3 \end{pmatrix} \quad , \quad m_{\rm D} = m \begin{pmatrix} a & 0 & 0 \\ b & 0 & 0 \\ c & 0 & 0 \end{pmatrix} . \tag{6}$$

Two singlets form a Dirac neutrino with mass M, while the third one decouples.

An important question is whether lepton number conservation is also a necessary condition for the cancellation of light neutrino masses, i.e. whether the cancellation can result from a symmetry that does not contain L conservation. One can show that there is always a conserved lepton number, if the cancellation occurs and if all three singlets have equal masses [1]. Let us therefore consider the case where the singlets involved in the cancellation, say $\nu_{\rm R}^1$ and $\nu_{\rm R}^2$, have different masses and where the condition (3) is imposed by a symmetry at the energy scale M_2. Below this scale, the symmetry is broken. The neutrino masses change due to the renormalisation group running. The contributions from the two singlets to m_ν run differently between M_1 and M_2 in the SM [29], so that the cancellation is destroyed. A rough estimate yields

$$m_\nu(M_1) \sim 10^{-4}\ {\rm GeV}\ \ln \frac{M_2}{M_1} \tag{7}$$

at M_1, which is unacceptable unless $\nu_{\rm R}^1$ and $\nu_{\rm R}^2$ are degenerate. Of course, this problem persists if also the third singlet contributes to the cancellation.

Thus, the cancellation of light neutrino masses can only be realised without fine-tuning, if the RH neutrinos involved in the cancellation have equal masses, which implies lepton number conservation. Therefore, any symmetry leading to vanishing neutrino masses via this cancellation has to contain the corresponding $\mathrm{U}(1)_L$ as a subgroup or accidental symmetry.

2.3 Small Perturbations

Non-zero masses for the light neutrinos are obtained by introducing small lepton-number-violating entries in the mass matrices (6). In the most general case,

$$m_{\rm R} = \begin{pmatrix} \epsilon_1 M & M & \epsilon_{13} M \\ M & \epsilon_2 M & \epsilon_{23} M \\ \epsilon_{13} M & \epsilon_{23} M & M_3 \end{pmatrix} \quad , \quad m_{\rm D} = m \begin{pmatrix} a & \delta_a & \epsilon_a \\ b & \delta_b & \epsilon_b \\ c & \delta_c & \epsilon_c \end{pmatrix} . \tag{8}$$

The smallness of the observed neutrino masses leads to the restriction

$$\epsilon_2\ ,\ \delta_{a,b,c} \lesssim 10^{-10} \tag{9}$$

for $\max(a,b,c) \sim 1$, $m/M \sim 0.1$, $M \sim 100$ GeV (as required by observability of RH neutrinos at LHC [21,22,24,26]), provided that there are no special relations between the small parameters causing additional cancellations. The perturbations ϵ_{23} and $\epsilon_{a,b,c}$ appear quadratically in m_ν and are correspondingly less severely constrained. Finally, ϵ_1 and ϵ_{13} do not lead to neutrino masses at the tree level at all but do contribute via loop diagrams [12], so that they are only slightly less constrained than the other parameters.

The most general mass matrices of Eq. (8) contain many free parameters, so that there is no clear imprint of the considered setup in the light neutrino mass matrix. A more interesting phenomenology is possible in constrained cases, some of which have been considered earlier in the context of leptogenesis [30,18]. For example, if all small parameters are of the same order of magnitude,

$$m_\nu \approx \frac{m^2}{M} \left[\epsilon_2\, v v^T - (v v_\delta^T + v_\delta v^T) \right] , \tag{10}$$

where we have abbreviated the first and second column of $m_{\rm D}$ by v and v_δ, respectively. The light neutrino masses are strongly hierarchical, since m_ν has rank 2 and hence one vanishing eigenvalue. The large Yukawa couplings a, b, c are determined by the light neutrino masses and mixing parameters, which leads to predictions for correlations between the branching ratios of different lepton-flavour-violating decays in supersymmetric see-saw models [30]. Likewise, the amplitudes of LFV processes at colliders are correlated, as we will discuss shortly.

3 Signals at Colliders

A striking signature of RH neutrinos at colliders would be lepton-number-violating (LNV) processes with like-sign charged leptons in the final state [31]. However, we have argued that all symmetries guaranteeing the required suppression of the light neutrino masses lead to the conservation of lepton number, so that the amplitudes of such processes vanish. Any L violation is severely restricted by the smallness of neutrino masses and can therefore not lead to sizable amplitudes. Consequently, in the absence of fine-tuning, LNV signals are expected be unobservable.

Another option are events with different leptons such as $\mu^-\tau^+$ in the final state, since these have a relatively small SM background as well. Such signals are unlikely to be observable at LHC, however [26]. In the considered scenarios, the mechanism leading to the cancellation of neutrino masses causes the terms in the corresponding amplitudes to add up constructively, leading to

$$A_{\alpha\beta} \propto \frac{m^2}{M^2}(a,b,c)_\alpha (a^*,b^*,c^*)_\beta \tag{11}$$

for the mass matrices of Eq. (8), where $\alpha \neq \beta$ denote the flavours of the charged leptons. If the cross sections are large enough for a detection at colliders, flavour-violating decays of charged leptons mediated by the RH neutrinos should be observable in upcoming experiments as well, since their amplitudes depend on the same combination of parameters. In the constrained case that yields Eq. (10), a, b, c can be determined from the light neutrino mass parameters, as mentioned above, so that the ratios $A_{e\mu}/A_{e\tau}$ and $A_{e\mu}/A_{\mu\tau}$ are predicted.

At the ILC, the resonant production of RH neutrinos is possible for $|V|_{ei} \gtrsim 0.01$ [32,22]. By observing the branching ratios for the subsequent decays into charged leptons, one could then determine the mixings of the heavy neutrinos with the different left-handed doublets directly.

4 Summary and Discussion

We have discussed the prospects for testing the see-saw mechanism of neutrino mass generation in collider experiments. We have assumed the existence of right-handed neutrinos with masses close to the electroweak scale (but no other new particles or interactions). The couplings of these neutrinos to the SM particles can only be large enough to make their observation at colliders possible, if different contributions to the light neutrino masses nearly cancel. This cancellation is then the main reason for the smallness of the observed neutrino masses, while the see-saw mechanism plays only a minor role. Therefore, we have to conclude that a direct test of the see-saw mechanism at the LHC or the ILC is not possible.

If one defines the leading-order mass matrices in such a way that they correspond to exactly vanishing light neutrino masses, non-zero masses appear as a result of small perturbations of this structure. One may then ask whether these perturbations could have consequences for signals at colliders and thus allow for a test of the mechanism of neutrino mass generation. Unfortunately, the smallness of the light neutrino masses immediately tells us that all perturbations are tiny and therefore irrelevant for collider signatures. Thus, the answer to this second question is

negative, too. Collider experiments are only sensitive to the leading-order mass matrices which do not lead to neutrino masses.

As a consequence, a connection between collider physics and neutrino masses can only be established, if the perturbations are introduced in such a way that the leading-order parameters are related to the light neutrino masses and mixings. In the most general case, this is not possible because there are too many free parameters. Then collider physics decouples completely from the light neutrino masses and their generation. However, the situation is better in constrained setups where only some of the perturbations are present or dominant. In the cases we discussed, a strong mass hierarchy is expected. To the extent that the leading-order Yukawa couplings are fixed by the measured neutrino masses and mixings, correlations between the branching ratios of lepton-flavour-violating processes can be obtained. This applies both to reactions at colliders and to LFV decays of charged leptons. Finally, e^+e^- colliders may be able to determine the mixings of RH neutrinos with the different flavours directly. Pursuing all these experimental options provides a chance to test constrained setups of the kind we have described. Of course, even in this optimistic case it is impossible to exclude the existence of additional, very heavy RH neutrinos contributing to neutrino masses via the standard see-saw mechanism.

Without an underlying symmetry, the described cancellation of the light neutrino masses amounts to severe fine-tuning. We have therefore discussed symmetry motivations. We have argued that every symmetry realising the cancellation has to include lepton number conservation. Otherwise, the cancellation is unstable against radiative corrections, so that fine-tuning is still required. Thus, both lepton number violation and light neutrino masses arise due to small perturbations of the leading-order mass matrices, and their magnitudes are related. Therefore, we expect lepton-number-violating signals at colliders to be unobservable in untuned scenarios. The cross sections for lepton-flavour-violating processes are not suppressed, so that LHC experiments might be able to observe such reactions. If this is the case, lepton flavour violation should also be observable in decays of charged leptons in the near future.

For completeness, let us briefly consider different see-saw scenarios as well, where the particles responsible for generating neutrino masses are not gauge singlets. In such a case, they can be produced by gauge interactions. Consequently, large Yukawa couplings and thus the discussed cancellation of light neutrino masses are no longer required. Neither is it necessary to impose lepton number conservation in order to motivate this cancellation by a symmetry. Therefore, lepton-number-violating processes can be detectable via their signature of like-sign charged leptons. One example for such a scenario is left-right symmetry close to the TeV scale. Here the right-handed neutrinos can be produced via interactions with the new gauge bosons W_R and Z' [31]. In the type-II see-saw setup, where neutrino masses arise from the vacuum expectation value of a scalar triplet Δ, the new particles can be produced in reactions like $q\bar{q} \to \gamma, Z \to \Delta^{++}\Delta^{--}$ [33]. Precise measurements of the decay rates $\Gamma(\Delta^{++} \to l^+_\alpha l^+_\beta)$ may even allow to probe the Majorana phases in the lepton mixing matrix [34,35,36]. In the type-III see-saw mechanism, fermionic triplets T are responsible for neutrino masses. Again, they may be detected by observing like-sign charged leptons, for instance in the process $q\bar{q} \to W^+ \to T^+T^0 \to l^+_\alpha l^+_\beta$ + jets, where the couplings relevant for the triplet decays are related to the light neutrino masses [37].

Acknowledgements

I'd like to thank Alexei Smirnov for the collaboration on [1], on which this talk was based.

References

1. J. Kersten and A. Yu. Smirnov, *Phys. Rev.* D **76**, 073005 (2007), arXiv:0705.3221.
2. P. Minkowski, *Phys. Lett.* B **67**, 421 (1977).

3. T. Yanagida in *Proceedings of the Workshop on Unified Theories and Baryon Number in the Universe*, eds. O. Sawada and A. Sugamoto (KEK, Tsukuba, Japan, 1979).
4. S. L. Glashow in *Proceedings of the 1979 Cargèse Summer Institute on Quarks and Leptons*, eds. M. Lévy, J.-L. Basdevant, D. Speiser, J. Weyers, R. Gastmans, and M. Jacob (Plenum Press, New York, 1980).
5. M. Gell-Mann, P. Ramond, and R. Slansky in *Supergravity*, eds. P. van Nieuwenhuizen and D. Z. Freedman (North Holland, Amsterdam, 1979).
6. R. N. Mohapatra and G. Senjanović, *Phys. Rev. Lett.* **44**, 912 (1980).
7. D. Wyler and L. Wolfenstein, *Nucl. Phys.* B **218**, 205 (1983).
8. J. Bernabéu, A. Santamaria, J. Vidal, A. Mendez, and J. W. F. Valle, *Phys. Lett.* B **187**, 303 (1987).
9. W. Buchmüller and D. Wyler, *Phys. Lett.* B **249**, 458 (1990).
10. W. Buchmüller and C. Greub, *Nucl. Phys.* B **363**, 345 (1991).
11. A. Datta and A. Pilaftsis, *Phys. Lett.* B **278**, 162 (1992).
12. A. Pilaftsis, *Z. Phys.* C **55**, 275 (1992), `hep-ph/9901206`.
13. G. Ingelman and J. Rathsman, *Z. Phys.* C **60**, 243 (1993).
14. C. A. Heusch and P. Minkowski, *Nucl. Phys.* B **416**, 3 (1994).
15. D. Tommasini, G. Barenboim, J. Bernabéu, and C. Jarlskog, Nucl. Phys. **B444**, 451 (1995), `hep-ph/9503228`.
16. J. Gluza, *Acta Phys. Polon.* B **33**, 1735 (2002), `hep-ph/0201002`.
17. A. Pilaftsis, *Phys. Rev. Lett.* **95**, 081602 (2005), `hep-ph/0408103`.
18. A. Pilaftsis and T. E. J. Underwood, *Phys. Rev.* D **72**, 113001 (2005), `hep-ph/0506107`.
19. E. K. Akhmedov and M. Frigerio, *JHEP* **01**, 043 (2007), `hep-ph/0609046`.
20. A. de Gouvêa, `arXiv:0706.1732`.
21. T. Han and B. Zhang, *Phys. Rev. Lett.* **97**, 171804 (2006), `hep-ph/0604064`.
22. F. del Aguila, J. A. Aguilar-Saavedra, and R. Pittau, *J. Phys. Conf. Ser.* **53**, 506 (2006), `hep-ph/0606198`.
23. D. Atwood, S. Bar-Shalom, and A. Soni, *Phys. Rev.* D **76**, 033004 (2007), `hep-ph/0701005`.
24. S. Bray, J. S. Lee, and A. Pilaftsis, *Nucl. Phys.* B **786**, 95 (2007), `hep-ph/0702294`.
25. F. M. L. de Almeida Jr., Y. A. Coutinho, J. A. M. Simoes, A. J. Ramalho, S. Wulck, and M. A. B. do Vale, *Phys. Rev.* D **75**, 075002 (2007), `hep-ph/0703094`.
26. F. del Aguila, J. A. Aguilar-Saavedra, and R. Pittau, *JHEP* **10**, 047 (2007), `hep-ph/0703261`.
27. W. Chao, S. Luo, Z.-z. Xing, and S. Zhou, *Phys. Rev.* D **77**, 016001 (2008), `arXiv:0709.1069`.
28. F. del Aguila, J. de Blas, and M. Perez-Victoria, `arXiv:0803.4008` (see also F. del Aguila, these proceedings).
29. S. Antusch, J. Kersten, M. Lindner, M. Ratz, and M. A. Schmidt, *JHEP* **03**, 024 (2005), `hep-ph/0501272`.
30. M. Raidal, A. Strumia, and K. Turzyński, *Phys. Lett.* B **609**, 351 (2005), Erratum *ibid.* **632**, 752 (2006), `hep-ph/0408015`.
31. W.-Y. Keung and G. Senjanović, *Phys. Rev. Lett.* **50**, 1427 (1983).
32. F. del Aguila, J. A. Aguilar-Saavedra, A. Martínez de la Ossa, and D. Meloni, *Phys. Lett.* B **613**, 170 (2005), `hep-ph/0502189`.
33. J. F. Gunion, R. Vega, and J. Wudka, *Phys. Rev.* D **42**, 1673 (1990).
34. J. Garayoa and T. Schwetz, *JHEP* **03**, 009 (2008), `arXiv:0712.1453`.
35. M. Kadastik, M. Raidal, and L. Rebane, `arXiv:0712.3912`.
36. A. G. Akeroyd, M. Aoki, and H. Sugiyama, *Phys. Rev.* D **77**, 075010 (2008), `arXiv:0712.4019`.
37. B. Bajc and G. Senjanović, *JHEP* **08**, 014 (2007), `hep-ph/0612029`.

Neutrinos: astrophysics and astroparticle aspects

NEUTRINO PRODUCTION IN NUCLEONIC INTERACTIONS IN GAMMA-RAY BURSTERS

HYLKE B. J. KOERS
Service de Physique Théorique, Université Libre de Bruxelles (U.L.B.), CP225, Bld. du Triomphe, B-1050 Bruxelles, Belgium

Neutrinos produced in gamma-ray bursters (GRBers) may provide a unique probe for the physics of these extreme astrophysical systems. Here we discuss neutrino production in inelastic neutron-proton collisions within the relativistic outflows associated with GRBers. We consider both the widely used fireball model and a recently proposed magneto-hydrodynamic (MHD) model for the GRB outflow.

1 Introduction

Gamma-ray bursts (GRBs) are short and energetic flashes of gamma rays (~ 100 keV), reaching Earth from apparently random direction at a rate of a few per day (see Ref.[1] for a review). The luminosity of these bursts may be very large, sufficient to temporarily outshine all other gamma-ray sources combined. Following their accidental discovery in 1967, the origin of these remarkable events has puzzled astronomers for three decades. In particular, the question whether gamma-ray bursts were produced by sources within our galaxy or at cosmological distances has remained under debate until the 1990s.

In the last decade there has been tremendous progress in our understanding of GRBs. This is largely due to observations of GRB afterglows – periods of prolonged broad-band electromagnetic emission following the actual burst – that were first discovered in 1997. The cosmological distance scale has been established by redshift measurements of the afterglow, and in some cases afterglow observations have allowed for identification of the host galaxy, providing further clues as to the nature of gamma-ray bursters (GBRers). There is presently compelling evidence that long-duration GRBs (the subclass of GRBs lasting more than 2 sec) are ultimately caused by core-collapse of massive stars[2], although the situation for short-duration GRBs (lasting less than 2 sec) is less clear.

One can easily estimate that the energy released in a stellar core-collapse matches that required to power a GRB, but the mechanism responsible for the energy transfer is far from obvious. The widely accepted framework to describe this is divided into four phases. In the *initial phase*, core-collapse of the massive star results in a black hole-accretion disk system. This launches a jet, a collimated outflow of plasma that contains a small baryonic component. In the *accelerating phase*, this plasma accelerates to a velocity close to that of light (Lorentz factor $\sim$ 300). In this acceleration process, the initial energy of the plasma is transfered to bulk kinetic energy of the baryons that are contained in the plasma. In the *coasting phase*, the outflow moves with a fixed velocity through the pre-burst stellar environment. Here dissipation of the kinetic energy in the flow, most likely as synchrotron emission of shock-accelerated electrons, gives rise to the actual GRB. Finally, the afterglow is attributed to the interaction of the outflow with the external medium during the *afterglow phase*.

Although the framework described above successfully explains the general features of the observations, many questions remain. Arguably one of the most important issues is the nature of the relativistic outflow. Within the widely used fireball model, it is understood that the plasma is initially dominated by thermal energy. Alternatively, the energy may be predominantly in electromagnetic form. Such outflows are expected naturally when a magnetized accretion disk is surrounding the central black hole.[3,4,5] Further questions concern for example the initial collimation of the flow, where magnetic fields may also play an important dynamical role, and the details of the energy dissipation process, which is likely to involve some particle acceleration mechanism such as shock acceleration.

Besides the intrinsic motivation to better understand the physics of GRBers, further motivation is provided by the connection to other fields of physics. Since GRBers are believed to be efficient astrophysical particle accelerators, they are candidate sources of high-energy neutrinos and cosmic rays and provide a laboratory to study the acceleration mechanism. Furthermore, it has been proposed to use GRBs as standard candles to constrain the evolution of the universe.[6] Finally, there are more speculative proposals, e.g. to use the arrival times of low- and high-energy emission to constrain Lorentz violating interactions.[7]

Neutrinos are promising probes of the environment of GRB sources. Neutrino emission is complementary to the electromagnetic emission in two respects. First, neutrinos mostly trace the hadronic component of GRB outflows whereas electromagnetic radiation mostly traces the leptonic component. Second, neutrinos can leave the GRB source when it is still optically thick. Substantial neutrino production may be expected in various phases of a developing GRB. In the initial phase, neutrino emission can constrain the formation of GRB fireballs. Within the fireball model, the dominant neutrino production process in this phase is electron-positron annihilation (providing a counterexample to the mostly hadronic production mechanisms). Under favorable circumstances, this may give rise to copious neutrino production. However, this mechanism is not sufficiently efficient to carry away the bulk of the fireball energy or to qualitatively modify the dynamical behavior of the fireball.[8] In both the coasting and afterglow phases of a developing GRB, it is believed that kinetic energy is dissipated through shock acceleration of electrons. These shocks will likely also accelerate any protons contained in the fireball. Interactions of these high-energy protons with target nucleons or photons give rise to a flux of high-energy neutrinos that offers good detection prospects with the upcoming km^3 neutrino detectors such as IceCube.[9,10] These neutrinos provide information on the nature of the flow, in particular the strength of the hadronic component, and on the energy dissipation process.

Here we report on a different mechanism to create neutrinos in GRBers, namely inelastic neutron-proton (np) collisions that occur during the accelerating phase. We compare the typical neutrino emission through this mechanism for two competing models: the fireball model and the recently proposed 'AC' model[5,11], which assumes that the energy in the outflow is predominantly electromagnetic. The motivation of this work is to estimate the detection prospects of this

neutrino emission and to investigate whether it can be used to differentiate between the fireball model and the AC model. The *np* mechanism has been considered within the fireball model before.[12,13] Our estimates are more pessimistic than existing ones, which can be traced to the more accurate modeling of the inelastic *np* cross section adopted in our work. For the AC model, the mechanism was first considered in Ref.[14], which forms the basis of the present discussion.

In the following section we discuss the dynamics of GRB outflows containing neutrons and protons, both within the fireball model and within the AC model. We then discuss neutrino production through *np* interactions, and finally we present our conclusions.

2 Dynamics

2.1 Acceleration in the fireball model and the AC model

A striking feature of GRB models is the bulk relativistic motion. This ingredient is motivated by an observational paradox: the short timescales and large energies suggest a huge energy density and thus an optically thick source. This then implies that the photon spectrum should be quasi-thermal, while observations show that it is not. Relativistic motion solves this problem by increasing the physical timescale compared to that inferred from observations, and by decreasing the photon energy in the source compared to the observed energy. The mechanism to accelerate the flow to relativistic velocities differs between models. In the fireball model, acceleration results from the pressure that photons exert on the optically thick fireball. In this case the dynamics of the flow may be approximated with[15]

$$\Gamma \propto r\,, \tag{1}$$

where Γ is the Lorentz factor of the flow, and r the radius of the flow (i.e., the distance from the central black hole). In the AC model, the energy to accelerate the outflow is provided by magnetic reconnection, a mechanism that converts electromagnetic energy into heat and bulk motion. When the magnetic field lines predominantly change polarity in the flow direction, as we will assume, the dynamics of the flow may be approximated with[16]

$$\Gamma \propto r^{1/3}\,. \tag{2}$$

Comparison with eq. (1) shows that the acceleration of the flow is much more gradual in the AC model than in the fireball model. As we will see, this directly affects the neutrino flux from *np* collisions.

In both the fireball model and the AC model, acceleration of the flow stops when there is no more energy available to further accelerate the baryons. In the fireball model, the acceleration of the flow can also be terminated when the flow, whose energy density decreases with increasing radius, becomes optically thin.

2.2 Neutron-richness

Since the baryons that are contained in the flow are to be accelerated to high Lorentz factors, the initial baryon density cannot be too large. This requirement is generally stated in terms of a dimensionless *baryon loading parameter*

$$\eta \equiv L/\dot{M}c^2 \sim 10^3\,, \tag{3}$$

where L denotes the total luminosity of the flow and $\dot{M}$ the mass flux. Near the central black hole, the typical energy density is larger than nuclear binding energies so that the baryonic component will consist predominantly of free protons and neutrons. The ratio of neutrons to

protons at the base of the outflow is determined by the competition of electron capture on protons and positron capture on neutrons. Recent studies[17] favor a neutron-rich environment, so that we expect that the outflow associated with a developing GRB is initially also neutron-rich. The neutron-to-proton ratio is parameterized with

$$\xi \equiv \dot{M}_n/\dot{M}_p \sim 1\,, \tag{4}$$

where $\dot{M}_{n(p)}$ denotes the neutron (proton) mass flux. At larger radii, where the energy densities are smaller, nucleosynthesizing reactions reduce the number of free neutrons. However, a significant amount of neutrons is expected in the flow up to the radius where neutron decay becomes important. This radius is much larger than the radii relevant to *np* collisions and thus neutron decay is not important for the mechanism considered in this work.

2.3 Neutron decoupling and pion production

Eqs. (1) and (2) are idealized approximations that are only valid when the baryons contained in the plasma play no dynamical role. Detailed numerical studies[14,18] indicate that a reasonably strong baryonic component affects the dynamics. However, eqs. (1) and (2) provide a reasonable approximation to the full dynamical behavior that captures the properties which are essential to the particle production problem discussed here. We will thus neglect the dynamical importance of nucleons in this section.

Regardless of the mechanism that accelerates the flow, protons are strongly coupled to the other plasma components by electromagnetic interactions and follow the dynamics of the flow. The neutrons, on the other hand, are only coupled to the plasma through inelastic *np* collisions. The nucleon number densities are initially very large so that the *np* interaction timescale is much shorter than the dynamical timescale. In this regime, the neutrons and protons essentially behave as a single fluid. As the outflow expands, the number densities decrease and the scattering timescale increases. When the *np* scattering timescale becomes smaller than the dynamical timescale, the neutrons effectively decouple from the plasma and coast with a certain terminal velocity.

When the flow is still in the accelerating phase at *np* decoupling, the protons are accelerated further and consequently a bulk velocity difference develops between protons and neutrons. If this velocity becomes sufficiently large, pions can be created in inelastic *np* collisions. The threshold condition to produce pions may be expressed as $\chi \equiv \Gamma_p/\Gamma_n > \chi_\pi \equiv 2.15$, where $\Gamma_{p(n)}$ denotes the proton (neutron) Lorentz factor. Approximating the dynamics of the outflow with $\Gamma \propto r^p$ (where $p = 1$ corresponds to the fireball model and $p = 1/3$ to the AC model), we observe that the radius where pion production occurs r_π and the decoupling radius r_{np} are related through $r_\pi \simeq r_{np}\chi_\pi^{1/p}$. Hence, in the fireball model the pion production radius is roughly twice the decoupling radius, while in the AC model it is an order of magnitude larger.

If the outflow contains many baryons, the available amount of energy per baryon is relatively small. In this case the acceleration of the flow may saturate before *np* decoupling, thus preventing inelastic collisions. Hence a sufficiently 'pure' flow ($\eta \gtrsim 500$ for the fireball model, or $\eta \gtrsim 200$ for the AC model) is required for particle production in inelastic *np* collisions.

3 Particle production in neutron-proton collisions

3.1 Interaction probability

The probability $d\tau$ for a neutron moving with dimensionless velocity β_n to interact with a proton population moving with dimensionless velocity β_p, within an infinitesimal radius $r \ldots r + dr$ is[14]

$$d\tau = \sigma\Gamma_p n'_p \left(\frac{\beta_p - \beta_n}{\beta_n}\right) dr \simeq \frac{\sigma n'_p}{2\Gamma_n}\left(\chi - \frac{1}{\chi}\right) dr\,, \tag{5}$$

where n'_p denotes the comoving proton density, σ is the inelastic np cross section[a], and we have assumed that $\beta_n \simeq 1$ and $\beta_p \simeq 1$ in the second equality. For outflows that follow an acceleration profile $\Gamma \propto r^p$ up to infinity, integrating eq. (5) gives the probability τ for an inelastic np collision to occur somewhere between the pion production radius and infinity. The result is independent of any model parameters except the index p. Performing this integral, we find that $\tau \simeq 0.2$ for the fireball model ($p = 1$) and $\tau \simeq 0.008$ for the AC model ($p = 1/3$). A comparison of these estimates with numerical results[14] shows that the estimate on τ is fairly accurate for the AC model over a large range of parameters. For the fireball model, however, this procedure tends to overestimate the optical depth. The reason for this is that, for a large range of model parameters, the flow becomes optically thin shortly after pion production becomes possible. This prevents further acceleration of the flow. Hence the acceleration profile $\Gamma \propto r$ does not hold up to large radii and the above estimate is not very accurate. Numerical results indicate that a typical value for the fireball model is $\tau^{\rm FB} \simeq 0.05$, while for the AC model $\tau^{\rm AC} \simeq 0.01$. Qualitatively, this difference can directly be understood from the dynamics: in the AC model, pion production is only possible at radii an order of magnitude larger than the np decoupling radius. This implies that the number density of target protons has decreased significantly since decoupling, leading to a small interaction probability. For the fireball model, pion production occurs closer to the decoupling radius, where the dilution of target protons is not so strong.

3.2 Neutrino emission

The neutrino fluence from a single GRB source at proper distance D_p can be expressed as $\Phi_\nu \simeq 1.5 N_n \tau / 4\pi D_p^2$, where N_n denotes the isotropic-equivalent number of neutrons in the flow, τ is the np interaction probability, and we have taken the average number of neutrinos (adding flavors and antiparticles) per np scattering equal to 1.5.[14] Using $N_n \simeq \xi_0/(1+\xi_0) \times E/(\eta m_n c^2)$, where ξ_0 is the initial neutron-to-proton flux ratio (cf. eq. (4)), E is the total isotropic-equivalent burst energy, η is the baryon loading parameter (cf. eq. (3)), and m_n the neutron mass, we find the following neutrino fluences for a burst at redshift $z = 1$ for the fireball model and the AC model, respectively:

$$\Phi_\nu^{\rm FB} \simeq 10^{-4}\,{\rm cm}^{-2} \left(\frac{\tau}{0.05}\right) \left(\frac{2\xi_0}{1+\xi_0}\right) \left(\frac{E}{10^{53}{\rm erg}}\right) \left(\frac{\eta}{10^3}\right)^{-1} ; \tag{6}$$

$$\Phi_\nu^{\rm AC} \simeq 2 \times 10^{-5}\,{\rm cm}^{-2} \left(\frac{\tau}{0.01}\right) \left(\frac{2\xi_0}{1+\xi_0}\right) \left(\frac{E}{10^{53}{\rm erg}}\right) \left(\frac{\eta}{10^3}\right)^{-1} . \tag{7}$$

Using the fact that pions are created near threshold, and assuming a roughly isotropic distribution in the center-of-mass frame, one finds that the typical observed neutrino energy is $\sim$50 GeV for the fireball model and $\sim$70 GeV for the AC model.[14] The typical energy for the AC model is slightly higher because charged pions will be accelerated by the plasma before decay.

For the fireball model, the flux estimate (6) is roughly an order of magnitude below previous estimates[13]. This difference can be attributed to a more accurate treatment of the np interaction (in Ref.[13] it is assumed that $\tau \simeq 1$). For the AC model, the interaction probability is smaller by another factor $\sim$5. This difference results from the more gradual acceleration of the flow and is thus directly linked to its nature. Unfortunately, the detection prospects with the upcoming km^3 neutrino detectors such as IceCube are very poor due to the relatively low neutrino energy: for reference values of the parameters we expect less than 1 event per year for a combined, diffuse flux of 1000 GRBers per year for either model. This GRB rate is rather optimistic if one takes into account that np decoupling only occurs for sufficiently pure (high-η) GRBers. We thus conclude that realistic detection prospects for the neutrino flux studied here requires a detector with larger effective area at sub-100 GeV energies than the upcoming km^3 detectors.

[a] We refer the reader to Ref.[14] for the adopted approximation for σ.

4 Discussion

Neutrino emission offers a promising way to further our understanding of gamma-ray bursters. Neutrinos carry information that is complementary to electromagnetic emission because they can escape from optically thick regions and because they predominantly trace the hadronic component of GRB sources. This offers a unique way to constrain the nature of the relativistic outflow associated with GRBs. However, due to their feeble interactions in detectors at Earth, it remains a challenging task to identify concrete realizations of this potential.

Here we have discussed neutrino production in inelastic neutron-proton collisions that occur when neutrons have decoupled from the outflow associated with GRBs. We have estimated the characteristic neutrino flux within the widely used fireball model and the more recently introduced AC model. The characteristic neutrino fluxes and energies are distinctively different for the two models, directly reflecting the dynamics and hence the nature of the flow. Unfortunately, the relatively low neutrino energy precludes any realistic detection prospects with the upcoming km^3 detectors such as IceCube.

Apart from neutrino production through charged pion decay, one also expects the production of gamma rays through the decay of neutral pions produced in np interactions. The plasma is optically thick to these gamma rays, and hence they cannot directly leave the plasma. In fact, the energy that is injected in the flow through this mechanism is reprocessed (through synchrotron radiation, pair production, and Inverse Compton scattering) and emitted in a different energy band. The typical energy of this reprocessed emission is $\sim$10 GeV for the fireball model and $\sim$100 keV for the AC model, and the expected fluence is detectable up to large redshifts with the GLAST satellite.[14] Detection of this emission would favor the fireball model, and constrain the baryon loading of the flow.

Acknowledgments

It is a pleasure to thank Dimitrios Giannios for a very enjoyable collaboration and for useful comments on the present manuscript, and Asaf Pe'er and Ralph Wijers for many valuable discussions on GRB physics. H.K. is supported by Belgian Science Policy under IUAP VI/11 and by IISN.

1. P. Mészáros, Rep. Prog. Phys. **69**, 2259 (2006)
2. S. E. Woosley and J. S. Bloom, ARA&A **44**, 507 (2006)
3. C. Thompson, MNRAS **270**, 480 (1994)
4. P. Mészáros and M. J. Rees, ApJ **482**, L29 (1997)
5. H. C. Spruit, F. Daigne, and G. Drenkhahn, A&A **369**, 694 (2001)
6. G. Ghirlanda, G. Ghisellini, and C. Firmani, New J. Phys **8**, 123 (2006)
7. G. Amelino-Camelia *et al.*, Nature **393**, 763 (1998)
8. H. B. J. Koers and R. A. M. J. Wijers, MNRAS **364**, 934 (2005)
9. E. Waxman and J. N. Bahcall, PRL **78**, 2292 (1997)
10. E. Waxman and J. N. Bahcall, ApJ **541**, 707 (2000)
11. D. Giannios and H. C. Spruit, A&A **430**, 1 (2005)
12. E. V. Derishev, V. V. Kocharovksy, and Vl. V. Kocharovksy, ApJ **521**, 640 (1999)
13. J. N. Bahcall and P. Mészáros, PRL **85**, 1362 (2000)
14. H. B. J. Koers and D. Giannios, A&A **471**, 395 (2007)
15. B. Paczyński, ApJ **308**, L43 (1986)
16. G. Drenkhahn, A&A **387**, 714 (2002)
17. W. X. Chen and A. M. Beloborodov, ApJ **657**, 383 (2007)
18. E. M. Rossi, A. M. Beloborodov, and M. J. Rees, MNRAS **369**, 1797 (2006)

HIGH ENERGY NEUTRINOS FROM THE COLD: STATUS AND PROSPECTS OF THE ICECUBE EXPERIMENT

C. Portello-Roucelle, for the IceCube collaboration
Lawrence Berkeley National Laboratory, One Cyclotron Road, Berkeley, CA 94720

The primary motivation for building neutrino telescopes is to open the road for neutrino astronomy, and to offer another observational window for the study of cosmic ray origins. Other physics topics, such as the search for WIMPs, can also be developed with neutrino telescope. As of March 2008, the IceCube detector, with half of its strings deployed, is the world largest neutrino telescope taking data to date and it will reach its completion in 2011. Data taken with the growing detector are being analyzed. The results of some of these works are summarized here. AMANDA has been successfully integrated into IceCube data acquisition system and continues to accumulate data. Results obtained using only AMANDA data taken between the years 2000 and 2006 are also presented. The future of IceCube and the extensions in both low and high energy regions will finally be discussed in the last section.

1 Motivations for neutrino astronomy with IceCube

We expect the acceleration of cosmic rays in astrophysical objects to be accompanied by the production of high energy neutrinos via pp or $p\gamma$ interactions at the acceleration site [1]. The detection of these neutrinos could provide us with fundamental information about these sources of cosmic rays, the most violent objects in the universe. The preferred candidates for astro-accelerators are expected to have large-scale strong shocks and/or strong magnetic field, such as active galactic nuclei (AGN), supernovae remnants, microquasars or gamma ray bursts. The study of such objects is on-going in gamma ray astronomy which has produced an impressive harvest of results in the last few years. Moreover, the recent announcement of the Auger collaboration of a possible correlation between the arrival direction of cosmic rays with energies in excess of 6×10^{19} eV and AGN [2] reinforces the interest in the studies on bottom-up processes for cosmic rays production and multi-messenger studies. For instance, if an AGN origin of the highest energy cosmic rays were to be confirmed, the neutrino flux from those objects could be within reach of a kilometer scale detector such as IceCube within a few years [3].

Neutrinos are a completely unique tool for the study of the cosmic ray sources. Charged protons below $10^{18.5}$ eV are bent by the inter-galactic magnetic fields and no longer point back to their sources thus making proton astronomy impossible at low energies. As for neutral messengers, the gamma rays are strongly attenuated above 50 TeV because of their interaction with the infrared background, reaching us only from galactic sources at high energies. The neutrinos, with their weak interaction cross section, are the only particles that allow us to explore the non thermic universe at cosmological distances and at all energies. Nevertheless, if this very small cross section is an advantage for the propagation from the source, the detection of neutrinos from astronomical events requires a very large detection volume. A kilometer cube scale is

needed to allow the detection of a measurable number of events in one year from the expected diffuse neutrino flux at the Waxman-Bahcall bound [4]. Several large scale neutrino telescopes are currently taking data or under development using either water (Baikal, ANTARES, NEMO, NESTOR and the future kilometer scale KM3Net) or ice as a detection medium (IceCube and its sub-detector AMANDA). The sensitivity of IceCube to astrophysical neutrino sources is given in a previous article [5]. We will give here a brief overview of the results of AMANDA for neutrino astrophysics in section 4, and will present the first point source search with a partial configuration of IceCube in section 5. In addition to these analyses, IceCube will also look for high energy neutrinos that are expected to be created by interaction of the cosmic ray protons with the background radiation [6]. More specific studies done with IceCube for supernovae detection [8] and GRB searches [9] can also be found in the literature.

2 Other physics potential of the experiment

In addition to high energy neutrino astronomy, IceCube's scientific reach extends to particle physics by looking for neutrino from annihilation of weakly interacting massive particles (WIMP), like the neutralino. These dark matter candidates are expected to accumulate in gravitational potential wells such as the Earth or Sun. If the annihilation products of two trapped neutralinos include neutrinos, a neutrino flux excess may be observed in the direction of the center of the Earth or Sun. As a consequence, neutrino telescopes like IceCube, IceCube DeepCore (see section 6.2) and AMANDA aim at the indirect detection of dark matter with the Sun or the Earth as effective neutrino sources [10]. The results obtained with AMANDA are presented in section 4.
Other topics of particle physics can also be adressed but will not be discussed here, like the search for magnetic monopoles [11], strange quark matter or SUSY Q-balls [12].

3 The IceCube detector

IceCube is located at the geographic South Pole. Neutrinos are detected through their charged current interactions in the ice of the detector volume (or in the ice surrounding the detector for muon and tau neutrinos). The Cherenkov light produced by the charged lepton resulting from this interaction travels through the transparent ice and is collected by the digital optical modules [17] (DOMs) of IceCube.

The current IceCube design [13] consists of 80 strings, each bearing 60 DOMs. They are deployed at depths between 1450 and 2450 m below the surface of the ice, forming the in-ice part of the detector. The DOMs have a spacing of 17m on each string and the strings form a triangular grid pattern with an inter-string spacing of 125 m, providing a 1 km^3 instrumented volume. The buried detector is topped on the surface by an array of 80 stations called IceTop [14] for the study of extensive air showers (see fig.1). Each IceTop station, located above an IceCube string, consists of two tanks filled with ice. Each of those tanks contains two DOMs of same design as the one used for the in-ice part of the detector. The surface array can be operated looking for anti-coincidence with the in-ice events to reject downgoing muons or in coincidence, to provide a usefull tool for cosmic ray composition studies [15,16].

Each DOM used by IceCube comprises a 10" Hamamatsu R7081-02 photomultiplier tube (PMT) housed in a glass pressure vessel and in situ data acquisition electronics. This electronics is the heart of the IceCube data acquisition system: it reads out, digitizes, processes and buffers the signals from the PMT. When the individual trigger conditions are met at the DOM, it reports fully digitized waveforms to a software-based trigger and event builder on the surface. The electronics acquires in parallel on Analog Transcient Waveform Digitizers (ATWDs) at 300 megasamples per second (MSPS) sampling over a 425 ns window. In addition the electronics

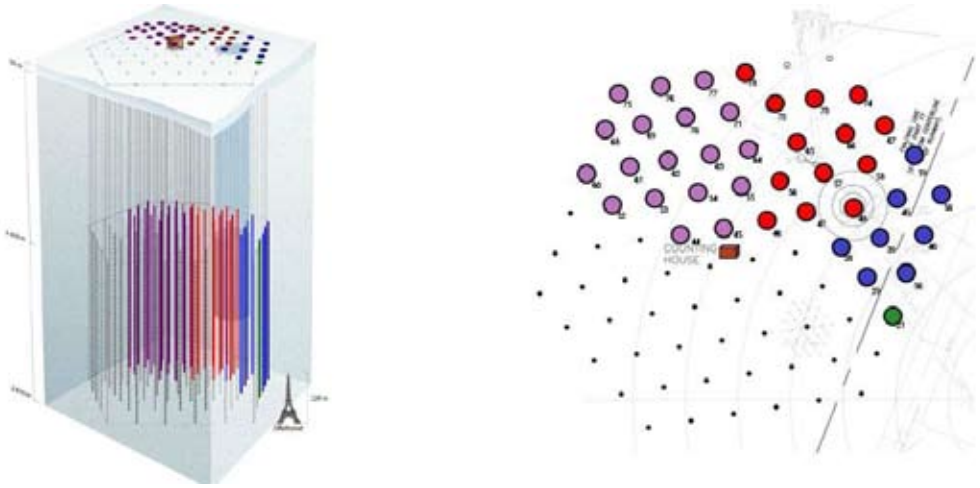

Figure 1: The IceCube detector side view (*on the left*) and top view (*on the right*). Currently installed lines (40) in ice are indicated. Current in-ice strings include: one string (in green) deployed in 2005, eight (in blue) in 2006, 13 (in red) in 2006 and 22 (in purple) in 2007. The AMANDA detector appears in the right part of in-ice. The IceTop surface array is also shown.

also records the signal with a coarser 40 MSPS sampling over a 6.4 μs window to catch the late part of the signals. Two parallel sets of ATWDs on each DOM operate in alternation so that one is active and ready to acquire while the other is read out. This design greatly reduces the dead-time of an individual DOM. The time calibration yields a timing resolution with a RMS narrower than 2ns for the signal sent by the DOM to the surface [7]. The noise rate due to random hits observed for in-ice DOMs is of the order of 300 Hz. This very low value gives us the possibility to monitor the DOM hit rates and to use it to have a sensitivity to low energy (MeV) neutrinos from supernova core collapse throughout the Milky Way and out to the Large Magellanic Cloud [8].

IceCube has also integrated its predecessor, the AMANDA detector, as it is now surrounded by IceCube (see fig. 1). AMANDA consists in 677 analog optical modules distributed on 19 strings with a much denser configuration than IceCube (string spacing of approximately 40m), giving it a lower energy threshold. The AMANDA optical modules are less sophisticated than the IceCube DOMs. The pulse processing electronics and data acquisition system is on the surface and the signal from AMANDA OMs has to be transmitted over roughly 1 km before being treated. Roughly half of the 677 AMANDA OMs transmit their signals to the surface over optical fibers, which allows for a timing accuracy of 2 to 3 ns, comparable to the one of the DOMs, although with greatly reduced dynamic range. The other half of the OMs are connected to the surface only by electrical cables, which stretch the pulses substantially thus separation of successive pulses is prevented. For relatively low energy events, the dense configuration of AMANDA gives it a considerable advantage over IceCube. Moreover, IceCube strings surrounding AMANDA can be used as an active veto against cosmic ray muons, making the combined IceCube + AMANDA detector considerably more effective for low energy studies than AMANDA alone. The DeepCore upgrade, whose construction will start next austral summer, will provide IceCube with a dense subdetector using DOM technology. This upgrade will open many possibilities in the low energy region and WIMPs studies as discussed in section 6.2.

The data taking with the partially finished IceCube detector is running smoothly and the detector is operating as expected. The detector began taking data in 2006 with a nine strings configuration (IC-9) and with a 22 strings configuration in 2007 (IC-22). The data acquisition with AMANDA also continues, enabling analyses done with more than 7 years of accumulated

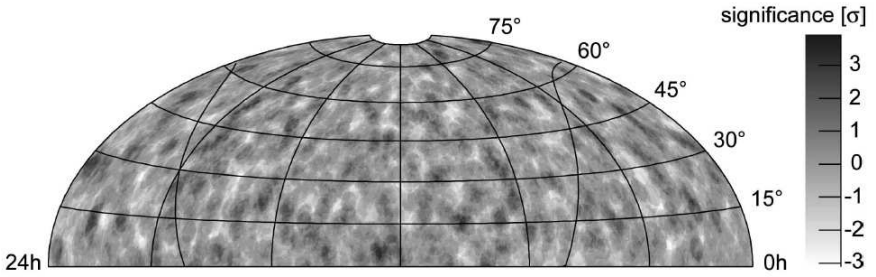

Figure 2: Significance map for the Northern hemisphere sky obtained for the 2000-2004 AMANDA II data analysis. The result obtained is compatible with random fluctuations.

data. The analysis of the IC-9 configuration of IceCube has already lead to first results with atmospheric neutrinos which are detailed in section 5. The analysis of IC-22 data is on-going and will be finished during the summer 2008.

4 Summary of current AMANDA results

4.1 Search for astrophysical sources

Between 2000 and 2004, AMANDA-II, the final configuration of the AMANDA detector as an independent entity, has been taking data. Results on the 5 years of the dataset have been reported. This subset yields 4282 up-going neutrino candidates with an estimated background contamination of approximately 5%. The analysis for point sources in the Northern hemisphere sky [18] for this dataset yielded no statistically significant point source of neutrinos as can be seen in Fig. 2. The highest positive deviation corresponds to about 3.7σ. The probability of such a deviation or higher due to background, estimated with 100 equivalent sky surveys of events with randomized right ascension, is 69%. Based on these studies, an upper limit has been placed on a reference E^{-2} point source flux of muon neutrinos averaged over declination in the Northern hemisphere sky at 90 % confidence level: $E^2 d\phi/dE < 5.5 \times 10^{-8} \mathrm{GeVcm}^{-2}\mathrm{s}^{-1}$ in the energy range of 1.6 TeV to 2.5 TeV.
Over the same period of time, a search for neutrino emission from 32 specific candidate sources chosen based on observations at various wavelengths in the electromagnetic spectrum has been performed [18]. No statistically significant evidence for neutrino emission was found from any of the candidate sources. The highest observed significance, with 8 observed events compared to 4.7 expected background events (1.2σ), is at the location of the GeV blazar 3C273. The second highest excess (1.1σ) is from the direction of the Crab Nebula, with 10 observed events compared to 6.7 expected background events.

In addition to searches for individual sources of neutrinos, AMANDA data taken between 2000 and 2003 have been used to set a limit on possible diffuse fluxes of neutrinos. Populations of distant sources could lead to such a diffuse flux that would clearly prove the acceleration of hadrons in astrophysical sources even if the sources cannot be resolved. This diffuse flux can be distinguished from the background of atmospheric neutrinos due to its harder spectra, expected from most astrophysical sources. This study relies on the the number of triggered OMs which serve as an energy estimator for AMANDA. A limit of $E^2 d\phi/dE < 7.4 \times 10^{-8}$ $\mathrm{GeVcm}^{-2}\mathrm{s}^{-1}\mathrm{sr}^{-1}$ is placed on the diffuse muon neutrino flux in the energy range from 16 TeV to 2.5 PeV at 90% confidence level [19]. Additionally, AMANDA has searched for an all-flavour diffuse flux from the Southern sky, a work on these three years of data places a limit of $E^2 d\phi/dE < 2.7 \times 10^{-7}$ $\mathrm{GeVcm}^{-2}\mathrm{s}^{-1}\mathrm{sr}^{-1}$, in the energy range of 2×10^5 to 10^9 GeV [23].

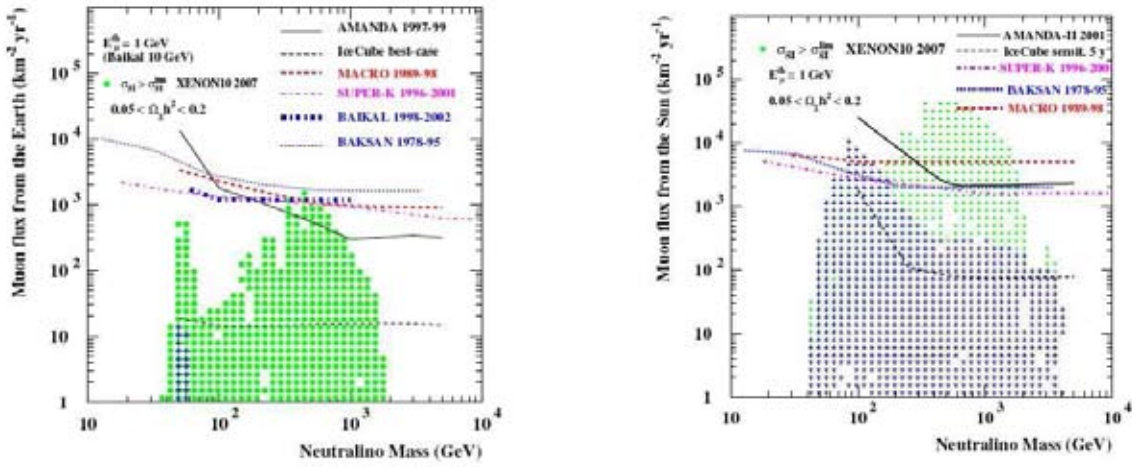

Figure 3: 90% CL upper limit on the muon flux from neutralino annihilations in the center of the Earth (left) and from the Sun (right). Markers show predictions for cosmologically relevant MSSM models, the dots representing models excluded by XENON10

4.2 Searches for neutralino dark matter

AMANDA can be used to search for neutralino dark matter by looking for a neutrino flux excess from the center of the Earth [20] or from the Sun [21]. The respective limits obtained with the 2001-2003 dataset for the Earth and the 2001 dataset for the Sun are given in Fig. 3. The figures show the muon flux limit from neutralino annihilations, along with the results from other indirect searches and predictions from theoretical models. Disfavoured models by recent direct searches with the XENON 10 experiment [22] are shown as green dots.

5 First results from the IceCube 9 strings configuration

The IC-9 dataset has a total livetime of 137.4 days taken between June and November 2006. 234 neutrino candidates were identified on this data sample with 211±76 (syst.) ± 14 (stat.) events expected from atmospheric neutrinos and less than 10% pollution by the background of down-going muons [24].

The zenith and azimuth angle distributions of these neutrino candidates are shown on Fig. 4. The agreement with simulation is good except for a discrepancy near the horizon due to a residual contamination of down going muons. This discrepancy would disappear with tighter event selection. One can notice the 2 strong peaks in the azimuth angle distribution (entry on the right in Fig. 4 on the right), due to the very asymetric configuration of the detector and corresponding to the long axis of IC-9 .

These data have been used to search for a possible accumulation of events in the sky [25]. The resulting sky-average point-source sensitivity for a source with an E^{-2} spectrum is $E^2 d\phi/dE = 12 \times 10^{-8}$ GeVcm^{-2}s^{-1} which is already comparable with what was obtained with the 5 years of AMANDA II data presented in section 4. The events were treated with a likelihood based analysis that makes use of the angular distribution of the background with a source hypothesis compared to a background only hypothesis obtained by scrambling the data in right ascension. The first significance map obtained with IceCube for the Northern hemisphere sky is shown on fig. 5. This map doesn't show any significant deviation from uniformity. The most significant excess, with a 3.3 σ significance is at r.a. $= 276.6°$, dec.$= 20.4°$. This is comparable with a

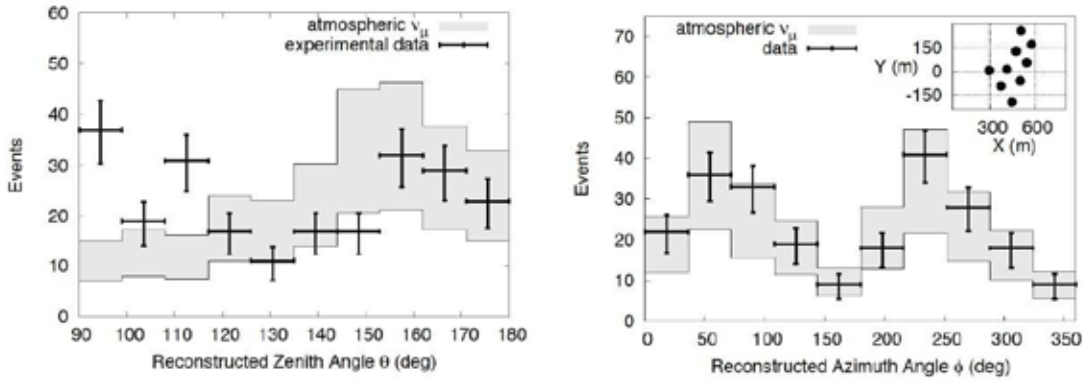

Figure 4: Zenith angle distribution (on the left) and azimuth angle distribution (on the right) for the final sample of IC-9 events. A zenith angle of 90 degrees corresponds to an horizontal event; a straight up-going event has a zenith angle of 180 degrees. The shadowed area indicates the simulation expectations with systematic errors. The error bars are statistical only. The configuration of the IceCube string seen from the top is also plotted on the right. The prefered axis of this configuration explains the features observed in the azimuth angle distribution.

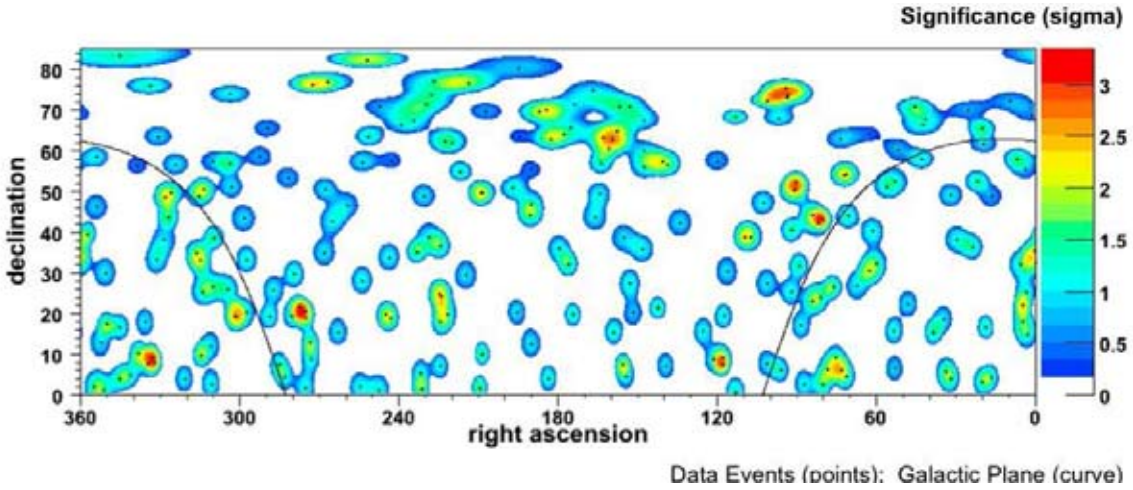

Figure 5: Significance map of the Northern hemisphere sky obtained with IC-9. The excesses observed are consistent with random fluctuations of an uniform background.

random fluctuation of a uniform background as 60% of the datasets scrambled in right ascension show an excess of 3.3 σ or higher somewhere in the sky. A search for neutrinos coming from 26 galactic and extragalactic preselected objects has also been performed on this dataset. In addition, the most significant excess over the expected background on these sources was found at the Crab nebula with 1.77σ, which again is consistent with random fluctuations.
Like in AMANDA, IceCube data can be used to probe the diffuse flux of neutrino from an unresolved population of astrophysical sources[26]. The sensitivity of IC-9 is 1.4×10^{-7} GeVcm^{-2}s^{-1}sr^{-1} which is only a factor of 2 above the AMANDA-II sensitivity despite the much shorter integrated exposure time. Large improvements can be expected from both longer operation of IceCube with even more strings and refinement of analysis techniques.

6 Conclusion : The future of IceCube

6.1 The next years of IceCube

The accumulated exposure of the IceCube 9 strings configuration does not allow us yet to reach the integrated exposure level required to probe astrophysical neutrino signals. Nevertheless,

various analyses are developing and are very promising [24]. These results confirm the stability of data taking, the good quality of the data recorded and experiment simulation. During the coming years, IceCube will continue to grow and will in 2009 reach an integrated exposure of 1 $km^3 \cdot yr$. This will be an important milestone as it represents roughly what is needed to reach the level of detection for an astrophysical neutrino flux [4]. When completed, the acceptance of the detector will naturally be larger, but it will also have an improved performance for reconstruction due to its larger size. In the case of the search for point sources for instance, the longer lever arm for the reconstruction of the muons tracks will lead to a better angular resolution of the detector which will become better than a degree.

6.2 One step further: extension of the IceCube detector at low energies with DeepCore

The capabilities of IceCube will be extended at both lower and higher energies in the near future. Starting next austral summer, a compact core of 6 strings using IceCube's DOM technology, called the DeepCore detector, will start to be deployed near the center of the main in-ice detector. The interstring spacing will be of the order of 72 m, allowing for the exploration of energies as low as 10-20 GeV. The surrounding IceCube strings will be used as an active veto to reduce the atmospheric muon background. The energy range that is explored is very important for dark matter seaches that were initiated with AMANDA. Moreover, the ability to select contained events opens the search for downgoing astrophysical neutrino signals at low energies. This will allow one to look above the current horizon of IceCube, even opening the possibility to look at the galactic center or sources like RX J1713.7-3946 [27].

6.3 The second step: extensions at higher energies

At EeV energies, on the other end of the energy range, an extension of IceCube is also studied. The radio or the acoustic signal generated by neutrino interacting in the ice can be detected with a high energy extension of IceCube. With a much increased detection volume, we will aim at detecting the GZK neutrino flux. With attenuation lengths of the order of the kilometer for acoustic (kHz frequency range) and for radio signals (MHz frequency range), a sparse instrumentation will suffice for this extention. Two projects are currently explored for this extension: AURA (Askarian Underice Radio Array) for the radio signal [28] and SPATS (South Pole Acoustic Test Setup) for the acoustic signal [29]. They are currently studying the polar ice and developing the hardware necessary for the building of a hybrid detector enclosing IceCube in another array of strings with a much larger spacing that will allow to study these very scarce and energetic events.

Acknowledgments

We acknowledge the support from the following agencies: National Science Foundation-Office of Polar Program, National Science Foundation-Physics Division, University of Wisconsin Alumni Research Foundation, Department of Energy, and National Energy Research Scientific Computing Center (supported by the Office of Energy Research of the Department of Energy), the NSF-supported TeraGrid system at the San Diego Supercomputer Center (SDSC), and the National Center for Supercomputing Applications (NCSA); Swedish Research Council, Swedish Polar Research Secretariat, and Knut and Alice Wallenberg Foundation, Sweden; German Ministry for Education and Research, Deutsche Forschungsgemeinschaft (DFG), Germany; Fund for Scientific Research (FNRS-FWO), Flanders Institute to encourage scientific and technological research in industry (IWT), Belgian Federal Office for Scientific, Technical and Cultural affairs (OSTC); the Netherlands Organisation for Scientific Research (NWO); M. Ribordy acknowl-

edges the support of the SNF (Switzerland); A. Kappes and J. D. Zornoza acknowledge support by the EU Marie Curie OIF Program.

References

1. T. K. Gaisser, F. Halzen and T. Stanev, Phys.Rept. 258 (1995) 173-236; Erratum-ibid. 271 (1996) 355-356, arXiv:hep-ph/9410384v1
2. J. Abraham *et al.* [The Pierre Auger collaboration] Astroparticle Physics, Volume 29, Issue 3, p. 188-204
3. F. Halzen and A. O'Murchadha, arXiv:0802.0887
4. E. Waxman, J. Bahcall, Phys. Rev. D, Volume 59, Issue 2, 15 January 1999
5. J. Ahrens *et al.*, IceCube collaboration, Astropart.Phys. 20 (2004) 507-532
6. R. Engel, D. Seckel and T. Stanev, Phys.Rev. D64 093010 (2001)
7. A. Achterberg *et al.* [AMANDA Collaboration], Astropart.Phys. 26 (2006) 155-173
8. F. Halzen, J.E. Jacobsen, E. Zas, Phys.Rev. D53 (1996) 7359-7361, arXiv:astro-ph/9512080v1
9. A. Kappes *et al* for the IceCube Collaboration, ICRC07 proc., Merida. arXiv:0711.0353
10. F. Halzen and D.Hooper, Phys. Rev. D73 1233507 (2006)
11. H. Wissing for the IceCube collaboration, ICRC07 proc., Merida. arXiv:0711.0353
12. A. Kusenko et al. Phys. Rev. Lett. 80, 3185, (1998)
13. IceCube preliminary design document, J.Ahrens et al. [IceCube Collaboration], *http://icecube.wisc.edu*
14. T. Gaisser *et al.* [IceCube Collaboration], ICRC 2007 proc., Merida arXiv:0711.0353
15. S. R. Klein, D. Chirkin for the IceCube Collaboration ICRC2007 proc., Merida, arXiv:0711.0353
16. X. Bai for the IceCube Collaboration, Nucl Phys B (Proc. Suppl.) 175-176(2008)415
17. K. Hanson, O. Tarasova [IceCube Collaboration], Nucl.Instrum. Meth A 567, 214 (2006)
18. A. Achterberg *et al.* [IceCube Collaboration], Phys. Rev. D 75, 102001 (2007) arXiv:astro-ph/0611063.
19. A. Achterberg *et al.* [IceCube Collaboration], Phys. Rev. D 76, 042008 (2007) [arXiv:astro-ph/0705.1315].
20. A. Achterberg *et al.* [AMANDA Collaboration], Astropart. Phys. 26, 129 (2006).
21. M. Ackermann *et al.* [AMANDA Collaboration], Astropart. Phys. 24, 459 (2006) arXiv:astroph/0508518.
22. J. Angle *et al.* arXiv:0706.003, (2007)
23. M. Ackermann et al. [AMANDA Collaboration], ApJ 675:1014 (2008)
24. A.Achterberg *et al*, [IceCube collaboration], Phys. Rev. D 76, 027101 (2007)
25. C. Finnley, J. Dumm and T. Montaruli for the IceCube Collaboration. ICRC2007 proc., Merida. arXiv:0711.0353
26. K. Hoshina, J. Hodges, G. C. Hill for the IceCube Collaboration. ICRC2007 proc., Merida. arXiv:0711.0353
27. J. Alvarez-Muñiz, F. Halzen, Astrophys.J. 576 (2002), arXiv:astro-ph/0205408v3
28. H. Landsmann *et al.* for the IceCube collaboration ICRC2007 proc., Merida, arXiv:0711.0353
29. S. Böser *et al.* for the IceCube Collaboration, ICRC2007 proc., Merida, arXiv:0711.0353

The ANTARES Neutrino Telescope : first results

Thierry PRADIER
for the ANTARES Collaboration [a]
University Louis-Pasteur & Institut Pluridisciplinaire Hubert Curien
Subatomic Research Department (DRS)
23 rue du Loess BP 28 - F67037 Strasbourg, France

The ANTARES Collaboration is completing the deployment of a 12 lines underwater detector, 2500m deep in the Mediterranean Sea, dedicated to high energy neutrino astronomy. Starting with the first line in 2006, 10 lines were continuously recording data by the end of 2007, which allow us to reconstruct downward-going cosmic muons, and search for the first upward-going ν-induced muons. Calibration topics will be described and preliminary results presented.

1 The neutrino as a new high-energy messenger

The advantage of using neutrinos as new messengers lies firstly on their weak interaction cross-section ; unlike protons ($E_{\text{cut-off}} \sim 5 \times 10^{19}$eV, $l_{\text{free path}} \sim 50$ Mpc) or γ ($E_{\text{cut-off}} \sim 10^{14}$eV, $l_{\text{free path}} \sim 10$ Mpc), they provide a cosmological-range unaltered information from the very heart of their sources. Secondly, charged particles are deflected by magnetic fields, with a mean deflection $\Delta\theta \sim L(\text{kpc})\frac{ZB(\mu G)}{E(\text{EeV})}$, yielding for Galactic Sources $\Delta\theta \sim 12^\circ$ at $10^{19}eV$. Neutrinos on the other hand point directly to their sources and exact production site.

The neutrinos ANTARES is aiming at are typically TeV neutrinos from AGNs (supermassive black holes believed to be hosted in the center of each galaxy), typically 30 orders of magnitude lower in flux [1] than solar neutrinos. The detection of those specific neutrinos requires under water/ice instruments, or alternatively acoustic/radio techniques in the PeV-EeV range and air showers arrays above 1 EeV. In spite of efforts in those various energy ranges, since the detection of the MeV neutrino burst from SN 1987A by KAMIOKANDE/BAKSAN/IMB/MONT-BLANC [2] no astrophysical source for neutrinos above a few GeV has ever been identified.

[a] http://antares.in2p3.fr

2 TeV cosmic neutrinos : production and detection

Sources for TeV ν are typically compact objects (neutron stars/black holes), from which often emerge relativistic plasma jets with a still unclear composition - leptonic or hadronic ?

2.1 Sources of TeV cosmic neutrinos ?

Most of these sources have already been extensively studied from radio wavelengths up to γ-rays. These photons can be produced by e^- *via* inverse compton effect (on ambient photon field)/synchrotron radiation, or by protons/nuclei *via* photoproduction of $\pi^0/\pi^\pm$:

$$p/A + p/\gamma \longrightarrow \pi^0\ \pi^\pm, \quad \text{with } \pi^0 \longrightarrow \gamma\gamma, \quad \text{and } \pi^\pm \longrightarrow \nu_\mu\ \mu, \quad \mu \longrightarrow \nu_\mu \nu_e e \tag{1}$$

In the former scenario, no neutrinos are produced, whereas in the latter, the neutrino flux is directly related to the gamma flux: a TeV neutrino detection from gamma sources would then yield a unique way to probe the inner processes of the most powerful events in the universe. Several hints exist which indicates that hadrons could be accelerated up to very high energies. Firstly, the combined radio, X-rays and γ-rays observations of the shell-type supernova remnant RX J1713.7-3946 [3] favour the production of photons *via* π^0 decay (figure 1, left). Secondly, the correlations between X and γ for the Blazar 1ES1959+650 [4] prove the existence of γ flares not visible in X (figure 1, right), which is difficult to account for in purely leptonic models. Finally, it should be reminded that the so-called GZK cut-off (interaction of ultra-high energy cosmic rays with the CMB) is a guaranteed source of sub-EeV neutrinos [5].

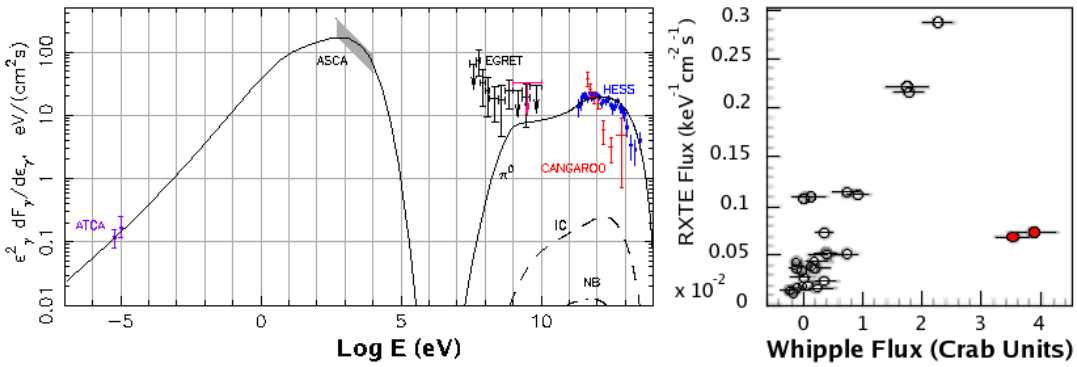

Figure 1: Left : Multiwavelength observations of the SNR RXJ 1713.7-39; the solid curve at energies above 10^7 eV corresponds to π^0-decay γ-ray emission, whereas the dashed and dash-dotted curves indicate the inverse Compton (IC) and Nonthermal Bremsstrahlung (NB) emissions, respectively. Right : Whipple vs RXTE flux, for the Blazar 1ES1959+650, which shows the existence of orphan γ flares (in red).

2.2 Practical issues for their detection

ANTARES can be seen as a fixed target experiment: a cosmic muon neutrino interacts in the Earth and produces a muon that propagates in sea water. The Čerenkov light emitted by the muon is detected by an array of photomultipliers arranged in strings, able to reconstruct the energy and direction of the incident muon/neutrino [6].

The main physical backgrounds are twofold. Atmospheric muons ($\sim 1/s$ at the reconstruction level in ANTARES), produced in the upper atmosphere by the interaction of cosmic rays, can be strongly suppressed because of their downward direction. Upward-going atmospheric neutrinos ($\sim$ 10/days in ANTARES) on the other hand are more delicate to identify: they have exactly the same signature as the expected cosmic signal ANTARES awaits for.

For a given neutrino flux Φ_ν, the number of events expected for a telescope of effective area A_μ (*i.e.* the size of a detector 100% efficient for muons) can be estimated as follows:

$$N_\mu \propto \Phi_\nu \times P_{\rm absorption}(\theta, E_\nu) \times \sigma_\nu \times R_\mu \times A_\mu, \tag{2}$$

where typically $\sigma_\nu \approx 2 \times 10^{-34}\ cm^2$, $R_\mu \approx 10\ km$, and $A_\mu \approx 0.06\ km^2$ (roughly the geometrical surface for ANTARES for reconstructed events with an angular resolution below 1°) at 100 TeV.

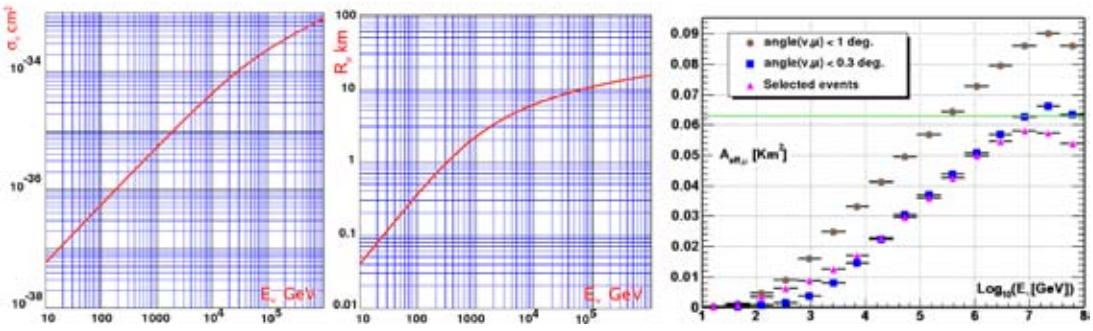

Figure 2: ν interaction cross-section, μ range in water, and effective area for muons.

The neutrino luminosity $L_\nu = 4\pi d^2 \Phi_\nu$ needed to detect N_ν events can then be written :

$$L_\nu \approx 10^{46} N_\nu \left(\frac{d}{4\ \mathrm{Gpc}}\right)^2 \left(\frac{E_\nu}{100\ TeV}\right)^{1-\alpha} \left(\frac{A_\mu\ T_{\rm obs}}{km^2\ yr}\right)^{-1} \mathrm{erg/s}, \tag{3}$$

for a source observed over a time $T_{\rm obs}$; $\alpha \sim 1/0.5$ below/above 100 TeV. Typically for blazars ($d \sim$ Gpc and $L \sim 10^{47}$erg/s), the required effective area is $A_\mu \sim 1\ km^2$, far beyond the reach of ANTARES. For galactic sources and $L \sim 10^{35}$erg/s, the necessary effective area goes down to $A_\mu \sim 0.1\ km^2$, typically the size of ANTARES.

3 ANTARES : description, performances & milestones

Two main kinds of signals can be detected with ANTARES: μ tracks initiated by the charged current interaction of a ν_μ in the Earth, and showers produced by the interaction of a neutrino (mainly ν_e and ν_τ by charged or neutral current channels) in water. Those signals are faint signals, and because of light scattering and absorption in water, their detection require single-photoelectron-sensitive devices. The measurements of the time of the hits (time resolution of the order of ns) and the amplitude of the hits (with a resolution of about 30%), together with the position of the hits (by measuring the position of each PMT, to reach a resolution of about 10 cm) are needed to achieve the reconstruction of those signals with the desired resolution.

Muon tracks are detected *via* their directional Čerenkov light (angle in water $\approx 42°$) and can be reconstructed with an angular resolution below 0.3° above 10 TeV (the resolution below this energy is dominated by the kinematics of the interaction). The energy resolution is quite poor, a factor 2-3 on average, restricted by the granularity/density of the light sensors and the fact that the muon traverses the detector. Showers produced by ν_e on the other hand emit quasi-isotropic light, and can be reconstructed with a better energy resolution (roughly 30 %) but with a poorer angular resolution $\sim$ 3-5 °.

3.1 Detector description

The ANTARES neutrino telescope, deployed at 2500 m below sea surface, 40 km off the coast of Toulon (Southern France) is composed of 12 strings, with 25 storeys each containing a triplet of

10" photomultipliers oriented at 45 degrees downward to be optimally sensitive to upward going muons. As of March 2008, 10 lines were connected and continuously taking data since end of 2007: the first line was operating as soon as March 2006, the second line in September 2006, and in January 2007 5 lines in whole were operational. A schematic description of the detector, together with the layout of the lines, can be found in figure 3 (left plot). The full completion of the telescope should be performed by summer 2008.

An instrumented line is also present on site, to perform environmental measurements : sea water temperature, salinity, sound velocity probes, as well as speed of the sea current and direction, all parameters required for an optimum track reconstruction, and for studies of biological backgrounds. The quality of sea water in particular, and its knowledge, is a fundamental parameter for Čerenkov photon detection [7]. The absorption length at the ANTARES site at 470 nm is roughly 60 m, with an effective scattering length of 300 m. It is a combination of this water quality (scattering and chromatic dispersion, accounting for 1.5 ns at a distance of 40m) and of the timing performances described below which finally takes down the angular resolution at the 0.2° level at high energy (where the neutrino and the produced muon are essentially colinear).

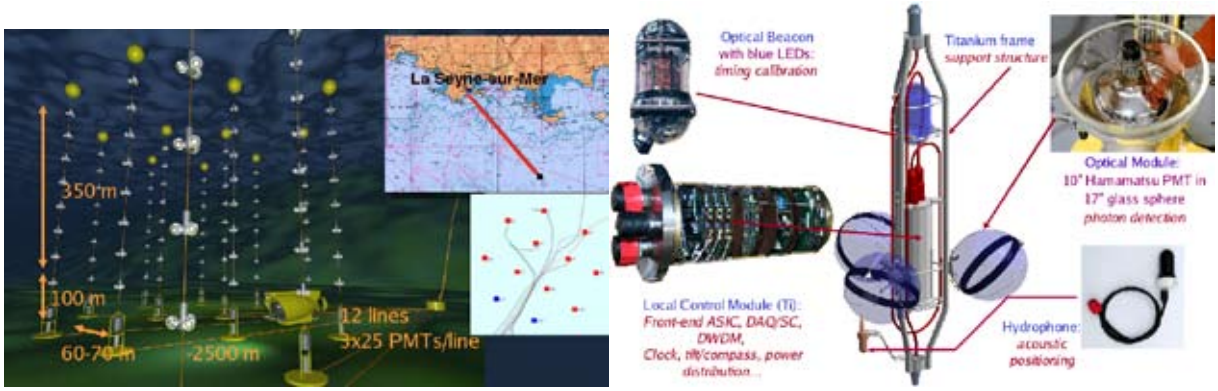

Figure 3: Left : Description, position and layout of the 12 lines of the ANTARES telescope, 10 of which are currently taking data. Right : Instruments on board of one of the ANTARES storeys.

The right panel of figure 3 displays the content of one of the ANTARES storey. PMTs are enclosed in pressure-resistant spheres [8], and a Titanium cylinder contains the front-end electronics. The intrinsic photoelectron transit time spread between the photocathode and its first dynode is roughly 1.3 ns, and the last dynode signal being digitised by a devoted chip, the ARS, gives a resolution better than 0.5 ns. The tilt/compass cards, and hydrophones on some of the storeys, allow us to measure continuously the position of the optical modules (see section 4). Finally, time calibration (see section 4) can be performed using a laser and LED beacons.

3.2 Physics performances

The energy resolution is a crucial element for the study of diffuse ν flux. The link between extragalactic sources of both cosmic rays, γ-rays and ν leads to severe limits on the ν diffuse flux expressed in the Waxman-Bahcall (WB) upper bound [9] $E^2\Phi < 4.5 \times 10^{-8}\mathrm{GeV.cm^{-2}.s^{-1}.sr^{-1}}$. After 3 years, ANTARES is expected to set an upper limit of $E^2\Phi < 3.9\times10^{-8}\mathrm{GeV.cm^{-2}.s^{-1}.sr^{-1}}$, just below the WB estimate.

The ANTARES sensitivity to point-like sources can be estimated as a function of the declination of a potential source: figure 4 (left) shows that ANTARES will be able to observe the Galactic Centre and other interesting γ sources, for most of the time complementary to ICECUBE. The 90% upper limit for $\nu_\mu + \bar{\nu}_\mu$ flux in case of null signal after 1 year is $E^2\frac{dN}{dE_\nu} = 4\times10^{-8}\mathrm{GeV.cm^{-2}.s^{-1}}$ at $\delta = -90°$, and rises to $1.5\times10^{-7}\mathrm{GeV.cm^{-2}.s^{-1}}$ at $\delta = +40°$.

Those limits improve those of MACRO for the Southern Sky, as can be seen in figure 4 (right), and are comparable to those obtained by AMANDA II for the Northern Sky [10].

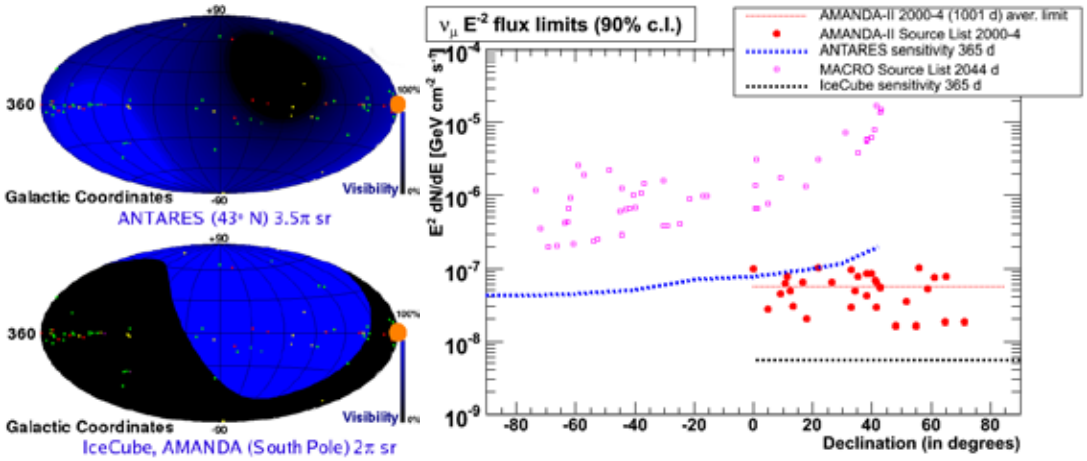

Figure 4: Left : Sky as visible by ANTARES and AMANDA/ICECUBE, in Galactic coordinates, the circle indicating the Galactic Centre. Right : Sensitivity for Point-like sources.

3.3 ANTARES *Milestones*

Conceiving and building a Neutrino Telescope in the Mediterranean require much preparatory work: the proposal of the experiment dates back to 1999 [11]. Nine years were thus needed to realise the 10 lines (soon 12!) that are currently taking data. Here is a short historical overview, before describing the calibration and results of ANTARES:

- **1996-2000 : Validation of the Project -** Water properties were first studied in order to choose the best site, and marine technologies were developed and improved. This period ended with the deployment of a demonstrator line [12] and the reconstruction of the first atmospheric muons in the ANTARES Collaboration.
- **2001-2004 : Final R&D, first deployments -** The Electro-Optical cable between the shore and the site was deployed in 2001, the Junction Box (distribution of power to lines) was operational in 2002. Finally, a Prototype Sector Line (similar to a final ANTARES line, but with only one sector consisting of 5 storeys) sucessfully took data between end of 2002 until its recovery in July 2003 ; a Mini-Instrumentation Line (MIL, environmental probes mainly) was also operated for a few months between Feb. and May 2003 [13].
- **2005-2007 : Construction, deployment and operation -** The MIL was recovered to be upgraded with two storeys of Optical Modules (MILOM), and took data for 2 years (April 2005 - March 2007), before the deployment, connection and operation of the first complete ANTARES line in March 2006 [14].

4 ANTARES in operation : calibration of a neutrino telescope

To be able to extract physical results from raw data, a neutrino telescope like any other detector has to be understood and calibrated : some aspects of this calibration will be reviewed here.

4.1 Acoustic positionning

The particularity of an underwater neutrino telescope, as compared with a ν Telescope in ice (ICECUBE), is that the lines, maintained as vertical as possible with a buoy, are moving under the

influence of water currents. Hence, a reconstruction of the line shape is needed for the positions of each individual PMTs to be known with an accuracy of 10-cm, which is required to achieve the 0.2° angular resolution at high energy. This is performed by an acoustic positioning system [15], as shown in figure 5 (left panel). Transponders on the sea ground emit signals, detected by hydrophones equipping some of the storeys. Together with data from tilt/compass cards, this allows for the determination of shape of the line; the actual position of the top storey can differ from the original straight line position by up to 15 m for strong sea currents ! If not accounted for, this would imply an error in the absolute positioning of a source of several degrees.

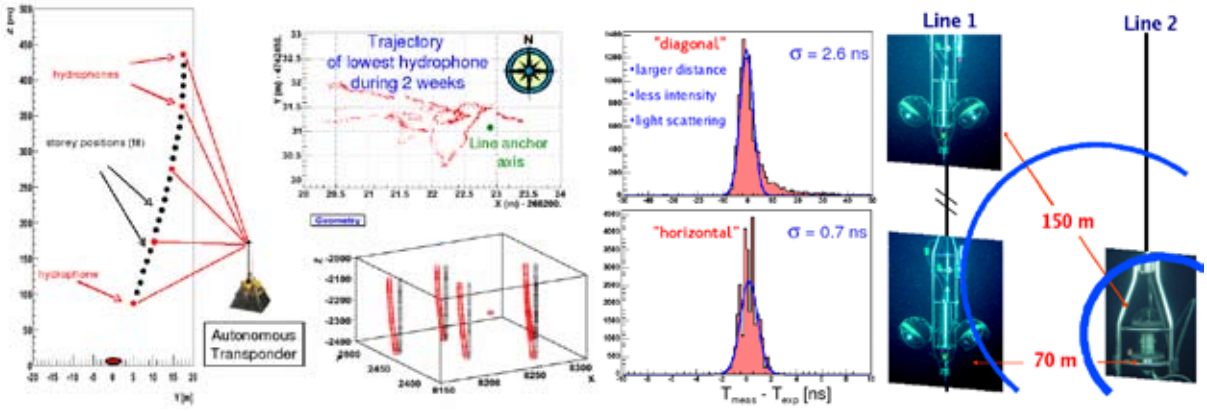

Figure 5: Left : Principles of acoustic positioning. Right : Principles of Time Calibration with LED Beacons.

4.2 Time calibration

An error of 0.3 ns in the photon arrival time on one of the PMTs is equivalent to a 10-cm error on its position: timing performances are thus as primordial as the line positioning. They can be studied using the light emitted by LED Beacons [16]. This blue light is detected by PMTs on adjacent lines, and the timing resolution as shown in figure 5 (right panel) can be estimated to be (*horizontal* case) as low as 0.7 ns, which is then dominated by the electronics.

4.3 ^{40}K calibration

Sea water contains ^{40}K which is a β emitter, the e^- in turn emitting Čerenkov radiation. Adjacent PMTs can thus coincidently detect this light, and this ^{40}K calibration is a powerful way to estimate the acceptance of each optical module [17].

5 ANTARES in operation : first signals and selected results

The trigger rate of ANTARES is roughly 1/s, mostly corresponding to atmospheric muons, 70% of which are multiple quasi-parallel muons, arriving at the same time in the detector [18]. A nice muon bundle seen with 10 lines is displayed in figure 6. Showers developping along a μ track can also be observed (fig. 6, right).

5.1 Line 1 data : first estimate for atmospheric muons flux

The angular distribution of reconstructed events can be transformed into an intensity *versus* depth (using acceptance corrections from simulation) in the region of uniform acceptance: each value of the zenith angle corresponds to a certain slant depth through the water mass above the detector. To compute the muon vertical intensity, the distribution of muons at sea level has to

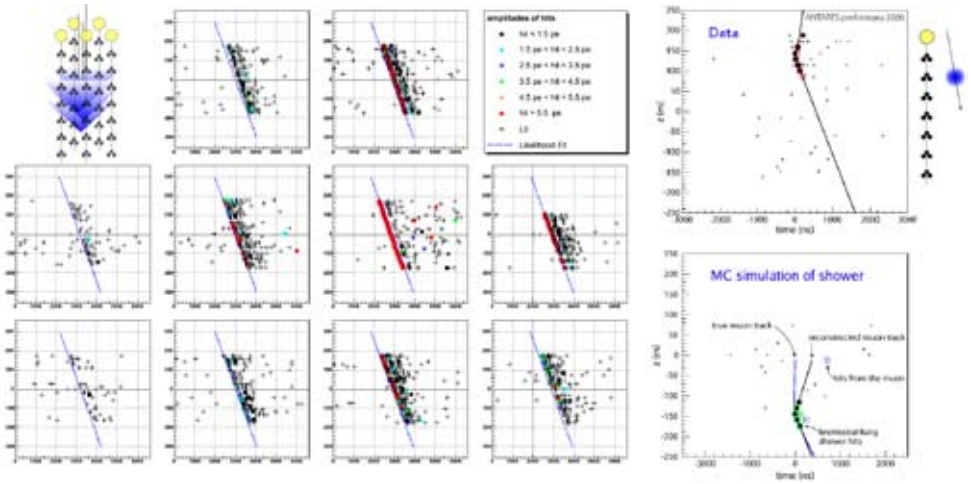

Figure 6: A μ bundle seen in 10 lines (altitude of hits *vs* time of hits, left) and a shower in 1 line (right), from Line 1 data (top) and Monte-Carlo (bottom).

be taken into account [19]. The results obtained using Line 1 data, with low sea currents from May to September 2006 (equivalent live time 10 days), are shown in figure 7. The errors of the order of 50% are dominated by the PMT acceptance. The agreement between data and other published values is good, showing that physics results can be extracted even with only 1 line!

5.2 Data with 5 lines : neutrino candidates

Figure 7 (right) shows a zenith angle distribution obtained with 5 Lines data (February-May 2007, equivalent live time 54 days). These data contain roughly 5×10^6 events, reconstructed with a 90% efficiency. After quality cuts, 20000 events remain, for which $\cos\theta$ is shown. The events reconstructed as upgoing ($\cos\theta > 0.1$) are 55 neutrino candidates, the events reconstructed as downgoing corresponding to atmospheric muons. The peak at -1 are vertically downward-going atmospheric μ, or muon bundles, very nicely reconstructed. Finally the slight excess near $\cos\theta \sim 1$ is an acceptance effect : the telescope is more sensitive to purely vertical tracks.

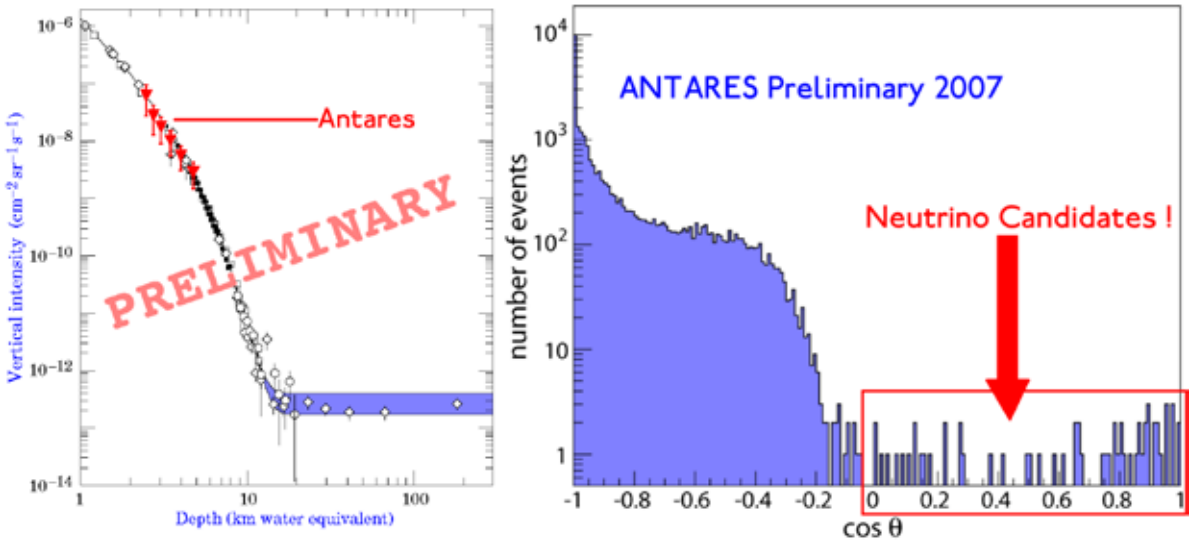

Figure 7: Left : Line 1 data, vertical intensity of atmospheric muons *versus* depth (water equivalent). Right : 5 lines data, distribution in zenith angle of (selected) events.

6 Conclusions and outlook

The 2 remaining ANTARES lines should be taking data by summer 2008, giving birth to the biggest Neutrino Telescope in the Northern Hemisphere. The current 10-lines telescope is already operating, and its acoustic positioning is fully functional. Despite its smaller size with respect to ICECUBE[20], ANTARES observes the Galactic Centre and other potential sources of TeV ν not accessible from the South Pole, leaving some margins for unexpected discoveries.

Furthermore, ANTARES is a part of the GCN, Gamma-ray bursts Coordinates Network[21], dedicated to γ-ray bursts, thought to be potential sources of high energy neutrinos : satellites/telescopes broadcast real-time alerts, which in turn trigger the recording of all ANTARES data within a 2 minutes time window[22]. Over a period of 15 months, 172 GCN alerts were distributed to ANTARES, and the telescope took data for 152 of them, corresponding to a $\sim 90\%$ live time !

ANTARES must be seen as the first stage towards a km^3-scale telescope, for which European institutes involved in current ν astronomy projects (ANTARES, NEMO, NESTOR) are already collaborating. This network, KM3NET[23], will give birth to a telescope with which neutrinos will be as common messengers as gamma-rays are now.

References

1. K. Mannheim, R. J. Protheroe & J. P. Rachen, *Phys. Rev.* D **63**, 023003 (2001)
2. K. S. Hirata *et al.*, *Phys. Rev. Lett.* **58**, 1490 (1987); R. M. Bionta *et al*, *Phys. Rev. Lett.* **58**, 1494 (1987); E. N. Alexeyev *et al*, *PZETF* **45**, 461 (1987); MONT-BLANC (controversial) : V. L. Dadykin *et al.*, *PZETF* **45**, 464 (1987)
3. E. G. Berezhko & H. J. Völk, `arXiv:0707.4647v1`, 30$^{\text{th}}$ ICRC 2007, Mexico
4. J. Holder (VERITAS Collaboration), `arXiv:astro-ph/0305577v1`, 28$^{\text{th}}$ ICRC 2003, Japan
5. D. Allard *et al.*, *Journal of Cosmology and Astroparticle Physics* **09**, 005 (2006)
6. M. A. Markov, *International Conference on High-Energy Physics*, 578 (1960)
7. ANTARES Collaboration, *AstroPart.Phys.* **19**, 253 (2003), *AstroPart.Phys.* **23**, 131 (2005)
8. ANTARES Collaboration, *Nucl. Instrum. Methods* A **484**, 369 (2002)
9. E. Waxman & J. Bahcall, *Phys. Rev.* D **59**, 023002 (1998)
10. AMANDA II limits: *Phys. Rev.* D **75**, 102001 (2007); MACRO: *Astrophysical Journal* **546**, 1038 (2001); ICECUBE: *Astropart. Phys.* **20**, 507 (2004)
11. ANTARES Collaboration, *Proposal* `arXiv:astro-ph/9907432v1`
12. A. Kouchner (ANTARES), *Preliminary demonstrator results*, Moriond EW 2000
13. Th. Pradier (ANTARES), *Frascati Physics Series* **XXXVII**, 89 (2004)
14. ANTARES Collaboration, *Astropart.Phys.* **26**, 314 (2006)
15. P. Keller (ANTARES), *Acoustics in* ANTARES, International Workshop *UnderWater Sensors & Systems*, Valencia (Spain) (2007)
16. F. Salesa (ANTARES), *The Optical Beacon Calibration System of* ANTARES, *ibid.*
17. D. Zaborov (ANTARES), *Coincidence studies in* ANTARES*: K^{40} and muons*, these proceedings
18. C. Picq (ANTARES), *Determination of cosmic μ multiplicity in* ANTARES, *ibid.*
19. ANTARES Collaboration, *Performance of the first* ANTARES *detector line*, to be submitted
20. K. Rawlins (ICECUBE), *AIP Conf.Proc.* **928**, 69 (2007)
21. **Gamma-ray bursts Coordinates Network** : `http://gcn.gsfc.nasa.gov`
22. M. Bouwhuis (ANTARES), 28$^{\text{th}}$ ICRC 2003, Japan
23. **KM3NeT** : `http://www.km3net.org`

TESTING DARK MATTER WITH NEUTRINO DETECTORS

SERGIO PALOMARES-RUIZ
IPPP, Department of Physics, Durham University, Durham DH1 3LE, United Kingdom

Neutrinos are the least detectable Standard Model particle. By making use of this fact, we consider dark matter annihilations and decays in the galactic halo and show how present and future neutrino detectors could be used to set general limits on the dark matter annihilation cross section and on the dark matter lifetime.

1 Introduction

With the next generation of neutrino experiments we will enter the era of precision measurements in neutrino physics. As a consequence, a lot of efforts are being dedicated to decide which are the best experimental set-ups. However and in addition to the detailed study of neutrino parameters, present and future neutrino detectors, thanks to their great capabilities, might also be used for other purposes. Among the possible synergies of these detectors, they could be used to test some of the properties of the dark matter (DM) of the Universe. For instance, it has been pointed out [1] that by using the spectral information of neutrinos coming from annihilations of DM particles in the center of the Sun, some of the DM properties could be reconstructed. In this talk however, we consider neutrinos coming from DM annihilations or decays in our galactic halo and show how they can be used to test some other DM properties.

We will use the fact that among the Standard Model (SM) particles, neutrinos are the least detectable ones. Therefore, if we assume that the only SM products from the DM annihilations (decays) are neutrinos, a limit on their flux, conservatively and in a model-independent way, sets an upper (lower) bound on the DM annihilation cross section (lifetime). This is the most conservative assumption from the detection point of view, that is, the worst possible case. Any other channel (into at least one SM particle) would produce photons and hence would give rise to a much more stringent limit. Let us stress that this is not an assumption about a particular and realistic case. On the other hand, for the reasons just stated, it is valid for any generic model, in which DM annihilates (decays) at least into one SM particle. Hence, the bounds so

obtained are bounds on the total annihilation cross section (lifetime) of the DM particle and not only on its partial annihilation cross section (lifetime) due to the annihilation (decay) channel into neutrinos.

In this talk, and following and reviewing the approach of Refs. [2,3,4,5], we consider this case and evaluate the potential neutrino flux from DM annihilation (decay) in the whole Milky Way, which we compare with the relevant backgrounds for detection. In such a way, we obtain general constrains on the DM annihilation cross section and on the DM lifetime, which are more stringent than previous ones [6,7,8,9,10].

2 Neutrino Fluxes from the Milky Way

Detailed structure formation simulations show that cold DM clusters hierarchically in halos which allows the formation of large scale structure in the Universe to be successfully reproduced. In the case of spherically symmetric matter density with isotropic velocity dispersion, the simulated DM profile in the galaxies can be parametrized via

$$\rho(r) = \rho_{\rm sc} \left(\frac{R_{\rm sc}}{r}\right)^{\gamma} \left[\frac{1+(R_{\rm sc}/r_{\rm s})^{\alpha}}{1+(r/r_{\rm s})^{\alpha}}\right]^{(\beta-\gamma)/\alpha}, \tag{1}$$

where $R_{\rm sc} = 8.5$ kpc is the solar radius circle, $\rho_{\rm sc}$ is the DM density at $R_{\rm sc}$, $r_{\rm s}$ is the scale radius, γ is the inner cusp index, β is the slope as $r \to \infty$ and α determines the exact shape of the profile in regions around $r_{\rm s}$. Commonly used profiles [11,12,13] (see also Ref. [14]) tend to agree at large scales, although they differ considerably in the inner part of the galaxy.

The differential neutrino plus antineutrino flux per flavor from DM annihilation or decay in a cone of half-angle ψ around the galactic center, covering a field of view $\Delta\Omega = 2\,\pi\,(1-\cos\psi)$, is given by

$$\frac{d\Phi}{dE_\nu} = \frac{\Delta\Omega}{4\,\pi}\,\mathcal{P}_k(E_\nu, m_\chi)\,R_{\rm sc}\,\rho_0^k\,\mathcal{J}_{\Delta\Omega,k}\,, \tag{2}$$

where m_χ is the DM mass, $\rho_0 = 0.3$ GeV cm^{-3} is a normalizing DM density, which is equal to the commonly quoted DM density at $R_{\rm sc}$, and $\mathcal{J}_{\Delta\Omega,k}$ is the average in the field of view (around the galactic center) of the line of sight integration of the DM density (for decays, $k=1$) or of its square (for annihilations, $k=2$), which is given by

$$\mathcal{J}_{\Delta\Omega,k} = \frac{2\,\pi}{\Delta\Omega}\,\frac{1}{R_{\rm sc}\,\rho_0^k}\int_{\cos\psi}^{1}\int_0^{l_{\rm max}} \rho(r)^k\,dl\,d(\cos\psi'), \tag{3}$$

where $r = \sqrt{R_{\rm sc}^2 - 2lR_{\rm sc}\cos\psi' + l^2}$ and $l_{\rm max} = \sqrt{(R_{\rm halo}^2 - \sin^2\psi R_{\rm sc}^2)} + R_{\rm sc}\cos\psi$. The contribution at large scales is negligible and thus, this integral barely depends on the size of the halo for $R_{\rm halo} \gtrsim$ few tens of kpc.

The factor $\mathcal{P}_k$ embeds all the dependences on the particle physics model and it reads

$$\mathcal{P}_1 = \frac{1}{3}\,\frac{dN_1}{dE_\nu}\,\frac{1}{m_\chi\tau_\chi} \quad \text{for decays and} \quad \mathcal{P}_2 = \frac{1}{3}\,\frac{dN_2}{dE_\nu}\,\frac{\langle\sigma_{\rm A}v\rangle}{2\,m_\chi^2} \quad \text{for annihilations}\,, \tag{4}$$

where the neutrino plus antineutrino spectrum per flavor is given by

$$\frac{dN_1}{dE_\nu} = 2\,\delta(E_\nu - \frac{m_\chi}{2}) \quad \text{for decays and} \quad \frac{dN_2}{dE_\nu} = 2\,\delta(E_\nu - m_\chi) \quad \text{for annihilations}\,, \tag{5}$$

and the factor of 1/3 comes from the assumption that the annihilation or decay branching ratio is the same for the three neutrino flavors. Let us note that this is not a very restrictive assumption, for even even when only one flavor is predominantly produced, there is a guaranteed

flux of neutrinos in all flavors thanks to the averaged neutrino oscillations between the source and the detector. Hence, although different initial flavor ratios would give rise to different flavor ratios at detection, the small differences affect little our results and for simplicity herein we consider flavor democracy.

2.1 Annihilations versus Decays: DM Halo Uncertainties

As mentioned above, while DM profiles tend to agree at large scales, uncertainties are still present for the inner region of the galaxy. In the two cases considered (annihilations and decay), the overall normalization of the flux is affected by the value of $\mathcal{J}_{\Delta\Omega,k}$. However, in the case of DM annihilations, it scales as ρ^2, whereas for DM decays, it scales as ρ. Our lack of knowledge of the halo profile is hence much more important for the neutrino flux from DM annihilations. For the three profiles considered here [11,12,13], astrophysical uncertainties can induce errors of up to a factor of 6 for the case of DM decays [5], but they can be as large as a factor of ~ 100 for DM annihilations [3,4]. In addition, if the DM mass is not known, DM annihilation and DM decay in the halo might have the same signatures. However, due to the fact that the dependence on the DM halo density is different for each case, in case of a positive signal, directional information would be crucial to distinguish between these two possibilities.

For concreteness, in what follows we present results using the Navarro, Frenk and White (NFW) simulation [12] as our canonical profile.

3 Neutrino Bounds

In order to obtain the constraints on the DM annihilation cross section and DM lifetime we assume that DM annihilates [2,3,4] or decays [5] only into neutrinos. If DM annihilates or decays into SM particles, neutrinos (and antineutrinos) are the least detectable ones. Any other possible annihilation or decay mode would produce gamma rays, which are much easier to detect, and would allow to set a much stronger (and model-dependent) bound. Thus, the most conservative approach [2,3,4,5] is to assume that only neutrinos are produced in DM annihilations or decays. Even in this conservative case, it has been shown that stringent limits can be obtained by comparing the expected time-integrated annihilation signal of all galactic halos [2] and the signal from annihilations [3,4] or decays [5] in the Milky Way Halo with the background at these energies.

3.1 The Atmospheric Neutrino Background

For $E_\nu \gtrsim 100$ MeV, the main source of background for a possible neutrino signal from DM annihilations or decays is the flux of atmospheric neutrinos, which is well known up to energies of ~ 100 TeV. Thus, in order to obtain a bound on the DM annihilation cross section and lifetime we need to compare these two fluxes, and in particular we consider the $\nu_\mu + \overline{\nu}_\mu$ spectra calculated with FLUKA [15].

In this energy range, we will follow the approach of Ref. [3]. By assuming that the only resultant products of DM annihilation (decay) are neutrino-antineutrino pairs, we first obtain a general bound by comparing the $(\nu_\mu + \overline{\nu}_\mu)$ neutrino flux from DM annihilation (decays) in the halo with the corresponding atmospheric neutrino flux for $E_\nu \sim 100$ MeV–100 TeV in an energy bin of width $\Delta \log_{10} E_\nu = 0.3$ around $E_\nu = m_\chi$ ($E_\nu = m_\chi/2$). For each value of m_χ, the limit on $\langle \sigma_{\rm A} v \rangle$ (τ_χ) is obtained by setting its value so that the neutrino flux from DM annihilations (decays) in the Milky Way equals the atmospheric neutrino spectrum integrated in the chosen energy bin. The reason for choosing this energy bin is mainly that the neutrino signal is sharply peaked around a neutrino energy equal to the DM mass (half of the DM mass) and this choice is within the experimental limits of neutrino detectors.

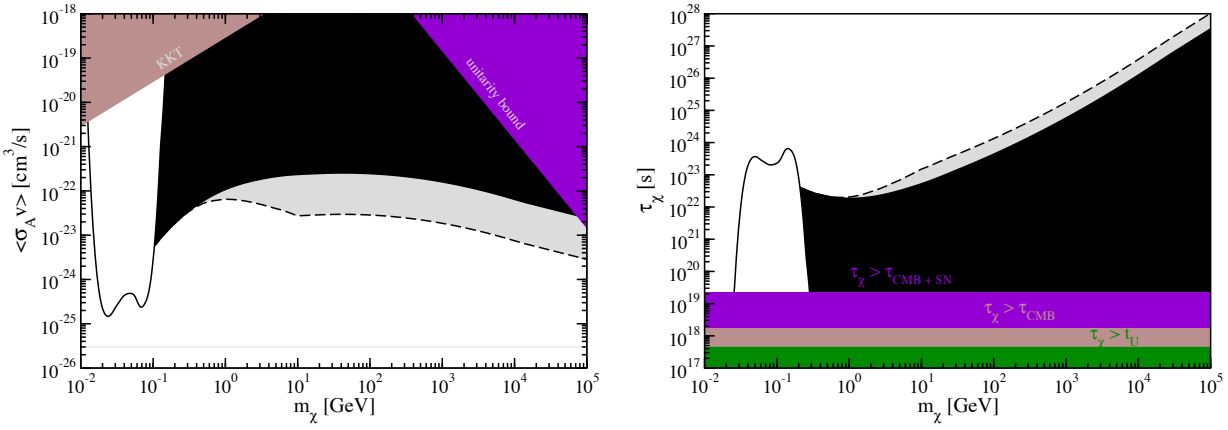

Figure 1: Bounds on the total DM annihilation cross section (left panel) and DM lifetime (right panel) for a wide range of DM masses obtained using different approaches: full-sky signal (dark area), angular signal (light area) and 90% CL limit using SK data at low energies [16] (hatched area). Results are obtained for a NFW profile. Other general bounds are also shown. Right panel: the unitarity bound [6], the limit above which the cusps of the DM halos are too flat (KKT) [7] and the natural scale for thermal relics. Left panel: bounds from Cosmic Microwave Background observations [9] and Cosmic Microwave Background plus Supernovae data [10] (both at 2σ confidence level) and the line $\tau_\chi = t_U$, with $t_U \simeq 4 \times 10^{17}$ s the age of the Universe. Adapted from Refs. [4,5].

The most conservative bound is obtained by using the full-sky signal, and this is shown in both panels of Fig. 1 where the dark areas represent the excluded regions. However, a better limit can be obtained by using angular information. This is mainly limited by the kinematics of the interaction. In general, neutrino detectors are only able to detect the produced lepton and its relative direction with respect to the incoming neutrino depends on the neutrino energy as $\Delta\theta \sim 30^o \times \sqrt{\mathrm{GeV}/E_\nu}$. As in Ref. [3] and being conservative, we consider a field of view with a half-angle cone of 30^o ($30^o \times \sqrt{10\,\mathrm{GeV}/E_\nu}$) for neutrinos with energies above (below) 10 GeV. This limit is shown in both panels of Fig. 1 by the dashed lines (light areas), which improves upon the previous case by a factor of a few for $E_\nu > 5$ GeV.

3.2 MeV Dark Matter

As we have just described, it is expected that a more detailed analysis, making a more careful use of the directional as well as energy information for a given detector, will improve these results. Note for instance that for energies $\sim$ 1-100 GeV neutrino oscillations would give rise to a zenith-dependent background, whereas we expect a nearly flat background for other energies for which oscillations do not take place. We now show how a more careful treatment of the energy resolution and backgrounds can substantially improve these limits [4,5].

Here we describe the analysis followed in Refs. [4,5] to set neutrino constraints on the DM total annihilation cross section and DM lifetime in the energy range 15 MeV $\lesssim E_\nu \lesssim$ 130 MeV. In this energy range the best data comes from the search for the diffuse supernova background by the Super-Kamiokande (SK) detector which has looked at positrons (via the inverse beta-decay reaction, $\overline{\nu}_e + p \rightarrow e^+ + n$) in the energy interval 18 MeV–82 MeV [16]. As for these energies there is no direction information, we consider the full-sky $\overline{\nu}_e$ signal. In this search, the two main sources of background are the atmospheric ν_e and $\overline{\nu}_e$ flux and the Michel electrons and positrons from the decays of sub-threshold muons. Below 18 MeV, muon-induced spallation products are the dominant background, and below $\sim$ 10 MeV, the signal would be buried below the reactor antineutrino background.

Although for $E_\nu \lesssim 80$ MeV the dominant interaction is the inverse beta-decay reaction (with free protons), the interactions of neutrinos (and antineutrinos) with the oxygen nuclei contribute significantly and must be considered. For our analysis we have included both the interactions of

$\overline{\nu}_e$ with free protons and the interactions of ν_e and $\overline{\nu}_e$ with bound nucleons, by considering, in the latter case, a relativistic Fermi gas model[17] with a Fermi surface momentum of 225 MeV and a binding energy of 27 MeV. We then compare the shape of the background spectrum to that of the signal by performing a χ^2 analysis, analogous to that of the SK collaboration [16]. In this way, we can extract the limits on the DM annihilation cross section and DM lifetime [4,5]. Hence, we consider the sixteen 4-MeV bins in which the data were divided and define the following χ^2 function [16]

$$\chi^2 = \sum_{l=1}^{16} \frac{[(\alpha \cdot A_l) + (\beta \cdot B_l) + (\gamma \cdot C_l) - N_l]^2}{\sigma_{stat}^2 + \sigma_{sys}^2} \,, \tag{6}$$

where the sum l is over all energy bins, N_l is the number of events in the lth bin, and A_l, B_l and C_l are the fractions of the DM annihilation or decay signal, Michel electron (positron) and atmospheric ν_e and $\overline{\nu}_e$ spectra that are in the lth bin, respectively. The fractions A_l are calculated taking into account the energy resolution of SK, interactions with free and bound protons and the correct differential cross sections [4]. The fractions B_l are calculated taking into consideration that in water 18.4% of the μ^- produced below Čerenkov threshold ($p_\mu < 120$ MeV) get trapped and enter a K-shell orbit around the oxygen nucleus and thus, the electron spectrum from the decay is slightly distorted with respect to the well-known Michel spectrum [18]. In the calculation of the fractions B_l and C_l we have used the low energy atmospheric neutrino flux calculation with FLUKA [19]. Note that, in a two-neutrino approximation and for energies below $\sim$300 MeV (where most of the background comes from), half of the ν_μ have oscillated to ν_τ, whereas ν_e remain unoscillated. Although this approximation is not appropriate, in principle, to calculate the low energy atmospheric neutrino background, however, for practical purposes, it introduces very small corrections [20]. Thus, in order to calculate B_l and C_l we use the two-neutrino approximation. The fitting parameters in the χ^2-function are α, β and γ, which represent the total number of each type of event. For the systematic error we take $\sigma_{sys} = 6\%$ for all energy bins [16].

In absence of a DM signal, a 90% confidence level (C.L.) limit can be set on α for each value of the DM mass. The limiting α_{90} is defined as

$$\int_0^{\alpha_{90}} P(\alpha)\, d\alpha = 0.9 \,, \tag{7}$$

where [a] $P(\alpha) = K \cdot e^{-\chi^2_\alpha/2}$ is the relative probability and χ^2_α is the minimum χ^2 for each α. The normalizing constant K is such that $\int_0^\infty P(\alpha)\, d\alpha = 1$. It is straightforward to translate the limit on α into limits of the total DM annihilation cross section and DM lifetime and these 90% CL bounds are shown in both panels of Fig. 1 by the hatched areas and they clearly improve (and extend to lower masses) by about an order of magnitude upon the general and very conservative bound obtained with the simple analysis described above for higher energies.

4 Conclusions

In this talk we have shown how neutrino detectors can also be used to test some of the DM properties and have obtained general bounds on the DM annihilation cross section and DM lifetime, which greatly improve over previous limits [6,7,8,9,10]. In order to do so, we have assumed that the only SM products from DM annihilations or decays are neutrinos, which are the least detectable particles of the SM. By making this assumption we have obtained conservative but model-independent bounds. In a simple way and for energies between $\sim$ 100 MeV and $\sim$ 100 TeV, we have considered the potential signal from DM annihilations or decays in the Milky Way and

[a] Note that there is an error in Eq.(8) of Ref. [4]. Nevertheless, this implies very small corrections to the results presented. I thank O. L. G. Peres for pointing this out.

have compared it to the atmospheric neutrino background. The general bounds are obtained by considering this potential signal and imposing that it has to be at most equal to the background in a given energy interval. We have also shown how this crude, but already very stringent limit, can be substantially improved by more detailed analysis which make careful use of the angular and energy resolution of the detectors, as well as of backgrounds. In this way, we have obtained[4,5] the 90% CL bounds on the DM annihilation cross section and DM lifetime for $m_\chi \lesssim 200$ MeV, which is about an order of magnitude more stringent.

Acknowledgments

The author is partially supported by the Spanish Grant FPA2005-01678 of the MCT.

References

1. O. Mena, S. Palomares-Ruiz and S. Pascoli, arXiv:0706.3909 [hep-ph].
2. J. F. Beacom, N. F. Bell and G. D. Mack, Phys. Rev. Lett. **99**, 231301 (2007) arXiv:astro-ph/0608090.
3. H. Yuksel, S. Horiuchi, J. F. Beacom and S. Ando, Phys. Rev. D **76**, 123506 (2007) arXiv:0707.0196 [astro-ph].
4. S. Palomares-Ruiz and S. Pascoli, Phys. Rev. D **77**, 025025 (2008) [arXiv:0710.5420 [astro-ph]].
5. S. Palomares-Ruiz, arXiv:0712.1937 [astro-ph].
6. K. Griest and M. Kamionkowski, Phys. Rev. Lett. **64**, 615 (1990); L. Hui, Phys. Rev. Lett. **86**, 3467 (2001) [arXiv:astro-ph/0102349].
7. M. Kaplinghat, L. Knox and M. S. Turner, Phys. Rev. Lett. **85**, 3335 (2000) [arXiv:astro-ph/0005210].
8. M. Kachelriess and P. D. Serpico, Phys. Rev. D **76**, 063516 (2007) [arXiv:0707.0209 [hep-ph]].
9. K. Ichiki, M. Oguri and K. Takahashi, Phys. Rev. Lett. **93**, 071302 (2004) [arXiv:astro-ph/0403164].
10. Y. Gong and X. Chen, arXiv:0802.2296 [astro-ph].
11. B. Moore, T. Quinn, F. Governato, J. Stadel and G. Lake, Mon. Not. Roy. Astron. Soc. **310**, 1147 (1999) [arXiv:astro-ph/9903164].
12. J. F. Navarro, C. S. Frenk and S. D. M. White, Astrophys. J. **462**, 563 (1996) [arXiv:astro-ph/9508025].
13. A. V. Kravtsov, A. A. Klypin, J. S. Bullock and J. R. Primack, Astrophys. J. **502**, 48 (1998) [arXiv:astro-ph/9708176].
14. W. Jaffe, Mon. Not. Roy. Astron. Soc. **202**, 995 (1983); N. W. Evans, Mon. Not. R. Astron. Soc. **260**, 191 (1993); *ibid.* **267**, 191 (1994); N. W. Evans, C. M. Carollo and P.T. de Zeeuw, Mon. Not. R. Astron. Soc. **318**, 1131 (2000).
15. G. Battistoni, A. Ferrari, T. Montaruli and P. R. Sala, Astropart. Phys. **19**, 269 (2003) [Erratum-ibid. **19**, 291 (2003)] [arXiv:hep-ph/0207035]; and arXiv:hep-ph/0305208.
16. M. Malek *et al.* [Super-Kamiokande Collaboration], Phys. Rev. Lett. **90**, 061101 (2003) [arXiv:hep-ex/0209028].
17. R. A. Smith and E. J. Moniz, Nucl. Phys. B **43**, 605 (1972) [Erratum-ibid. B **101**, 547 (1975)].
18. P. Haenggi, R. D. Viollier, U. Raff and K. Alder, Phys. Lett. B **51**, 119 (1974).
19. G. Battistoni, A. Ferrari, T. Montaruli and P. R. Sala, Astropart. Phys. **23**, 526 (2005).
20. G. L. Fogli, E. Lisi, A. Mirizzi and D. Montanino, Phys. Rev. D **70**, 013001 (2004) [arXiv:hep-ph/0401227].

NEUTRINO SELF INTERACTIONS IN SUPERNOVAE

Gianluigi Fogli[1], Eligio Lisi[1], Antonio Marrone[1,a] Alessandro Mirizzi[1,2]
[1] *Dipartimento di Fisica and Sezione INFN di Bari, Via Amendola 173, 70126 Bari, Italy*
[2] *Max-Planck-Institut für Physik (Werner-Heisenberg-Institut), Föhringer Ring 6, 80805 München, Germany*

Oscillations of neutrino emerging from a supernova core are studied. In this extremely high density region neutrino self interactions induce collective flavor transitions. When collective transitions are decoupled from matter oscillations, as for our chosen matter profile, an analytical interpretation of the collective effects is possible, by means of a mechanical analogy with a spherical pendulum. For inverted neutrino hierarchy the neutrino propagation can be divided in three regimes: synchronization, bipolar oscillations, and spectral split. Our simulation shows that averaging over neutrino trajectories does not alter the nature of these three regimes.

1 Introduction

Supernova neutrino oscillations are a very important tool to study astrophysical processes and to better understand neutrino properties [1]. When neutrinos leave the surface of the neutrinosphere, they undergo vacuum and matter oscillations. Beside this, in the first few hundred kilometers neutrino-neutrino interactions induce collective flavor transitions, whose effect can be very important, depending on the neutrino mass hierarchy. Self-interaction effects are expected to be non negligible when $\mu(r) \sim \omega$, where $\mu(r)$ is the neutrino potential associated to the neutrino background ($\mu = \sqrt{2}G_F(N_\nu(r) + \overline{N}_\nu(r))$, analogously to the MSW potential $\lambda = \sqrt{2}G_F N_{e^-}(r)$) and ω is the vacuum oscillation frequency. We neglect the solar mass square difference $\delta m^2 = m_2^2 - m_1^2 \ll \Delta m^2 = |m_3^2 - m_{1,2}^2|$, and consider a two-neutrino mixing scenario where the oscillations are governed by the mixing angle θ_{13}. Since in the supernova context ν_μ and ν_τ cannot be distinguished we generically speak of $\nu_e \leftrightarrow \nu_x$ oscillations. In our work we assume $\Delta m^2 = 10^{-3}$ eV^2 and $\sin^2\theta_{13} = 10^{-4}$. Figure 1 shows the radial profiles of the matter

[a] Speaker

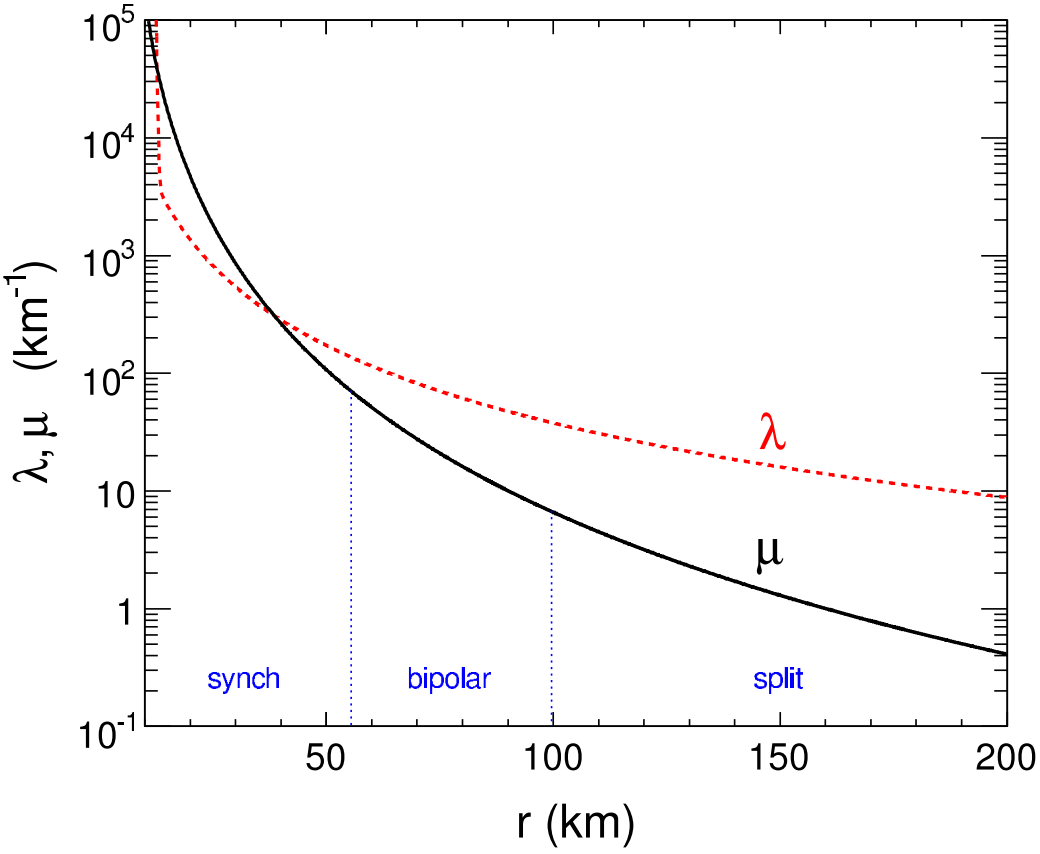

Figure 1: Radial profiles of the neutrino self-interaction parameter $\mu(r) = \sqrt{2}\,G_F\,(N + \overline{N})$ and of the matter-interaction parameter $\lambda(r) = \sqrt{2}\,G_F\,N_{e^-}$ adopted in this work, in the range $r \in [10,\ 200]$ km.

potential $\lambda(r)$ and of the neutrino potential $\mu(r)$, and the approximate ranges where collective flavor transitions of different type occur: synchronization, bipolar oscillation and spectral split. The nonlinearity of the self interactions induce neutrino oscillations very different from the ordinary MSW effect. When undergoing collective flavor transition neutrinos and antineutrinos of any energy behave similarly, as we will see in the following. This kind of transitions occurs for small r, well before the ordinary MSW resonance, allowing for a clear interpretation of the numerical simulations. For matter profiles different from our own, the MSW resonance condition can occur in the same region of the collective transitions: shallow electron density profiles [2] can trigger MSW effects around $O(100)$ km. In that case it is much more difficult to disentangle collective from MSW effects in the results of the simulations.

2 Reference model and pendulum analogy

In our work, we use normalized thermal spectra with $\langle E_e \rangle = 10$ MeV, $\langle \overline{E}_e \rangle = 15$ MeV, and $\langle E_x \rangle = \langle \overline{E}_x \rangle = 24$ MeV for ν_e, $\overline{\nu}_e$, ν_x and $\overline{\nu}_x$, respectively. The geometry of the model, the so called "bulb model" [2], has a spherical symmetry, since we assume that neutrinos are half-isotropically emitted from the neutrinosphere. Along any radial trajectory there is, therefore, a cylindrical symmetry. By virtue of that, we need only two independent variables to describe the neutrino propagation and interaction: the distance form the supernova center r, and the angle ϑ between two interacting neutrinos. If the dependence on ϑ is integrated out, we speak of "single-angle" approximation, while the general situation of variable ϑ is dubbed "multi-angle" case. The numerical simulation in the multi-angle case is extremely challenging, since it requires the solution of a large system (size of order 10^5) of coupled non-linear equations. The propagation

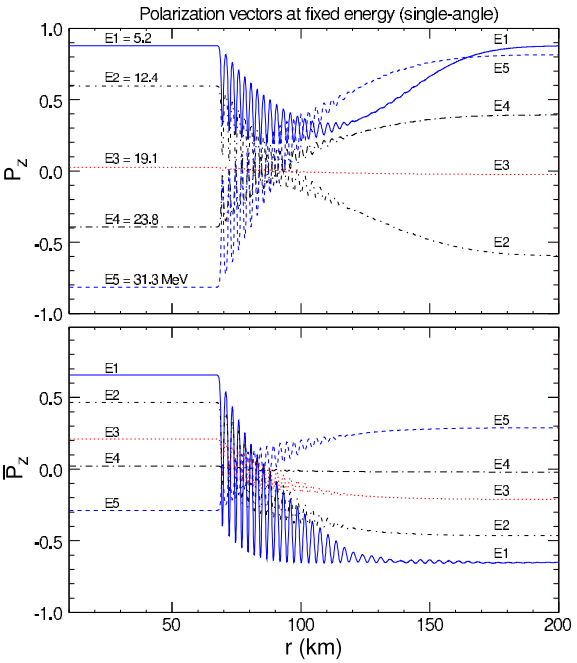

Figure 2: Single-angle simulation in inverted hierarchy: P_z (neutrinos) and $\overline{P}_z$ (antineutrinos) as a function of radius, for five energy values.

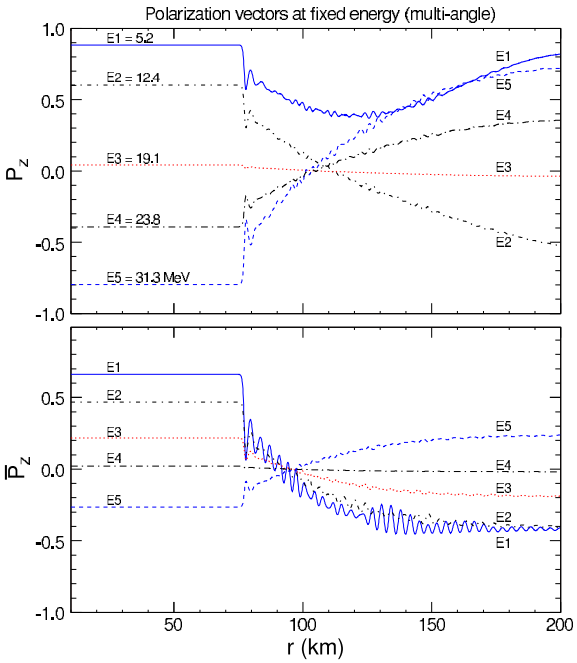

Figure 3: Multi-angle simulation in inverted hierarchy: P_z (neutrinos) and $\overline{P}_z$ (antineutrinos) as a function of radius, for five energy values.

of neutrinos of given energy E is studied through the Liouville equation for the density matrix. By expanding the density matrix on the Pauli matrices and on the identity, the equations of motion can be expressed in terms of two polarization vectors, $\mathbf{P}(E)$ and $\bar{\mathbf{P}}(E)$, for neutrinos and antineutrinos, respectively. By introducing a vector $\mathbf{B}$ that depends on the mixing angle θ_{13}, and a vector $\mathbf{D} = \mathbf{J} - \overline{\mathbf{J}}$ that is the difference between the integral over the energy of $\mathbf{P}$ and $\overline{\mathbf{P}}$, the equations of motion can be written as

$$\dot{\mathbf{P}} = (+\omega\mathbf{B} + \lambda\mathbf{z} + \mu\mathbf{D}) \times \mathbf{P} \ , \quad (1)$$

$$\dot{\overline{\mathbf{P}}} = (-\omega\mathbf{B} + \lambda\mathbf{z} + \mu\mathbf{D}) \times \overline{\mathbf{P}} \ . \quad (2)$$

In the general case, the polarization vectors depend also on the neutrino emission angle θ_0 (the neutrino incidence angle ϑ can be expressed in terms of r and of the emission angle at the neutrinosphere θ_0). The electron neutrinos survival probability P_{ee} is a function of the polarization vector, $P_{ee} = 1/2(1 + P_f^z/P_z^i)$, where the i and f refer to the initial and final state respectively (analogously for antineutrinos). The equations of motion for $\mathbf{P}(E)$ and $\bar{\mathbf{P}}(E)$ can be reduced (under reasonable approximations [3]) to the equations of motion of a gyroscopic pendulum, a spherical pendulum of unit length in a constant gravity field, characterized by a point-like massive bob spinning around the pendulum axis with constant angular momentum. The pendulum inertia is inversely proportional to $\mu(r)$, while its total angular momentum depends on the difference of the integrated polarization vectors $\mathbf{J}$ and $\bar{\mathbf{J}}$ [3]. The motion of a spherical pendulum is, in general, a combination of a precession and a nutation [4,5]. In the case of normal hierarchy of the neutrino mass spectrum the pendulum starts close to the stable, downward position and stays close to it, as μ slowly decreases and no collective effect is present. In the inverted hierarchy case, the pendulum starts close to the "unstable," upward position. At the beginning, for small r, when μ is large (m is small), the bob spin dominates and the pendulum remains precessing in the upward position conserving angular momentum [5], a situation named synchronization [6,4]. Nevertheless, since μ decreases with r, at a certain point any $\theta_{13} \neq 0$ triggers the fall of the pendulum and its subsequent nutations, the so called bipolar oscillations. The increase of the

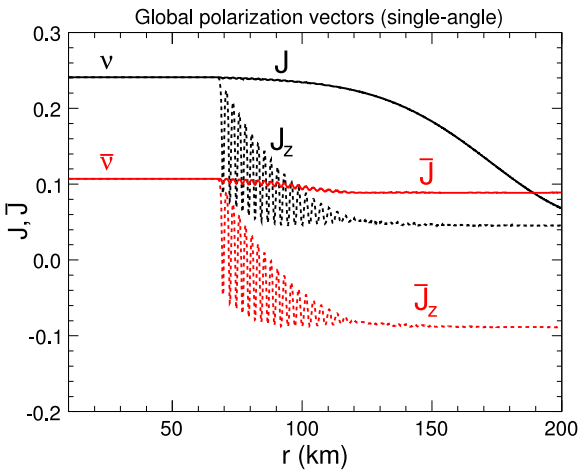

Figure 4: Single-angle simulation in inverted hierarchy: modulus and z-component of $\mathbf{J}$ and $\overline{\mathbf{J}}$.

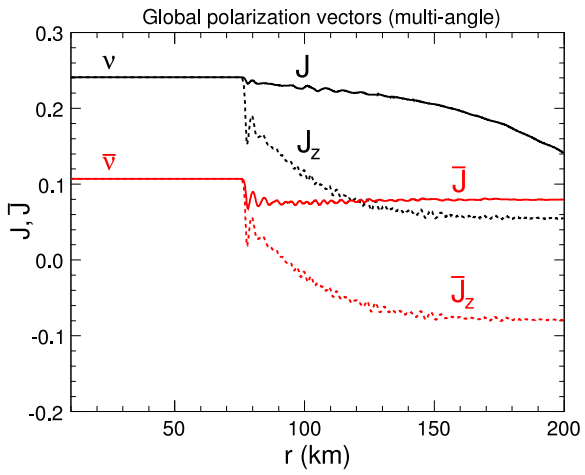

Figure 5: Multi-angle simulation in inverted hierarchy: modulus and z-component of $\mathbf{J}$ and $\overline{\mathbf{J}}$.

pendulum inertia with r reduces the amplitude of the nutations, and bipolar oscillations are expected to vanish when self-interaction and vacuum effects are of the same size. At this point, at the end of the bipolar regime, self-interaction effects do not completely vanish and the spectral split builds up: a "stepwise swap" between the ν_e and ν_x energy spectra. The neutrino swapping can be explained by the conservation of the pendulum energy and of the lepton number [7]. The lepton number conservation is related to the constancy of $D_z = J_z - \overline{J}_z$, that is a direct consequence of the equation of motion. For a detailed description of the pendulum analogy and of our reference model the reader is referred to our previous work [3] and references therein.

3 Simulations

Figures 2 and 3 show the third component of $\mathbf{P}$ and $\bar{\mathbf{P}}$, as a function of the radius, for different energy values, for the single- and multi-angle simulations, respectively. Bipolar oscillations starts at the same r and their periods are equal for both ν and $\overline{\nu}$ at any energy, confirming the appearance of a self-induced collective behavior, in the single- and in the multi-angle case. The behavior of each P_z and $\overline{P}_z$ depends on its energy. For neutrinos, Figure 2, the spectral split starts around the critical energy $E_c \simeq 7$ MeV: the curve relative to $E < E_c$ ends up at the same initial value ($P_{ee} = 1$), while the curves for $E > E_c$ show the P_z inversion ($P_{ee} = 0$). Neutrinos with an energy of $\sim$ 19 MeV do not oscilate much, because this is roughly the energy for which the initial ν_e and ν_x fluxes are equal. For antineutrinos, all curves show almost complete polarization reversal, with the exception of small energies (of few MeV, not shown in Figure 3). Figures 4 and 5 show the evolution of J and J_z for neutrinos and antineutrinos, in the single- and multi-angle cases. The behavior of these vectors can be related to the gyroscopic pendulum motion. At the beginning, in the synchronized regime, all the polarization vectors are aligned so that $J = J_z$ and $\overline{J} = \overline{J}_z$: the pendulum just spins in the upward position without falling. Around $\sim$ 70 km the pendulum falls for the first time and nutations appear. The nutation amplitude gradually decreases and bipolar oscillations eventually vanish for $r \sim 100$ km. At the same time, the spectral split builds up: antineutrinos tend to completely reverse their polarization, while this happens only partially for neutrinos. As said before, also for antineutrinos there is a partial swap of the spectra for $E \sim 4$ MeV. From Figure 5 it appears that bipolar oscillations of $\mathbf{J}$ and $\overline{\mathbf{J}}$ are largely smeared out in the multi-angle case. The bipolar regime starts somewhat later with respect to the single-angle case, since neutrino-neutrino interaction angles can be larger than the (single-angle) average one, leading to stronger self-interaction effects, that force the system

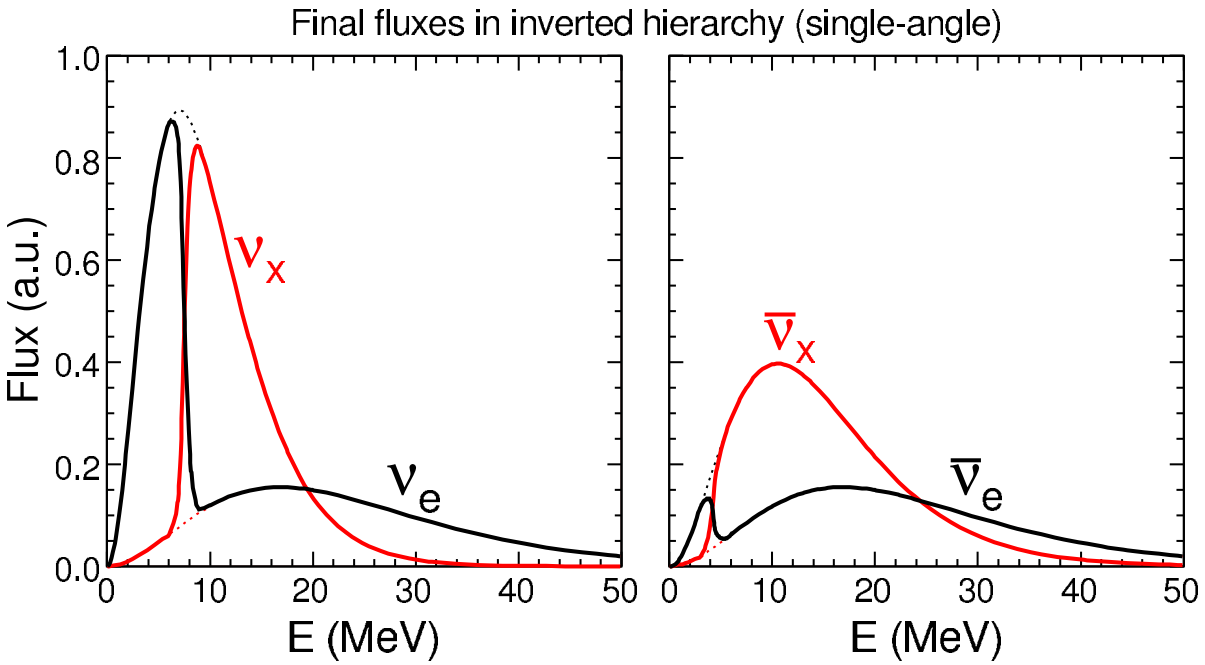

Figure 6: Single-angle simulation in inverted hierarchy: final fluxes (at $r = 200$ km, in arbitrary units) for different neutrino species as a function of energy. Initial fluxes are shown as dotted lines to guide the eye.

in synchronized mode slightly longer. However, just as in the single-angle case, the spectral split builds up, $\overline{J}_z$ gets finally reversed, while the difference $D_z = J_z - \overline{J}_z$ remains constant. Figures 6 and 7 show the final neutrino and antineutrino fluxes, in the single- and multi-angle simulations. The neutrinos clearly show the spectral split effect and the corresponding sudden swap of ν_e and ν_x fluxes above $E_c \simeq 7$ MeV. In the right panel of Figure 6, the final antineutrino spectra are basically completely swapped with respect to the initial ones, except at very low energies, where there appears an "antineutrino" spectral split. This phenomenon can be related to the loss of $\overline{J}$ and of $|\overline{J}_z|$ [3]. Also in the multi-angle case of Figure 7 , the neutrino spectral swap at $E > E_c \simeq 7$ MeV is rather evident, although less sharp with respect to the single-angle case, while the minor feature associated to the "antineutrino spectral split" is largely smeared out.

4 Conclusions

We have studied supernova neutrino oscillations in a model where the collective flavor transitions (synchronization, bipolar oscillations, and spectral split) are well separated from the MSW resonance. We have performed numerical simulations in both single- and multi-angle cases, using continuous energy spectra with significant ν-$\overline{\nu}$ and ν_e-ν_x asymmetry. The results of the single-angle simulation can be analytically understood to a large extent by means of a mechanical analogy with the spherical pendulum. The main observable effect is the swap of energy spectra, for inverted hierarchy, above a critical energy dictated by lepton number conservation. In the multi-angle simulation, the details of self-interaction effects change (e.g., the starting point of bipolar oscillations and their amplitude), but the spectral swap remains a robust, observable feature. In this sense, averaging over neutrino trajectories does not alter the main effect of the self interactions. The swapping of neutrino and antineutrino spectra could have an impact on r-process nucleosynthesis, on the energy transfer to the shock wave during the supernova explosion and on the propagation of the neutrinos through the shock wave. From the point of view of neutrino parameters, collective flavor oscillations in supernovae could be instrumental in identifying the inverse neutrino mass hierarchy, even for very small θ_{13}. [8]

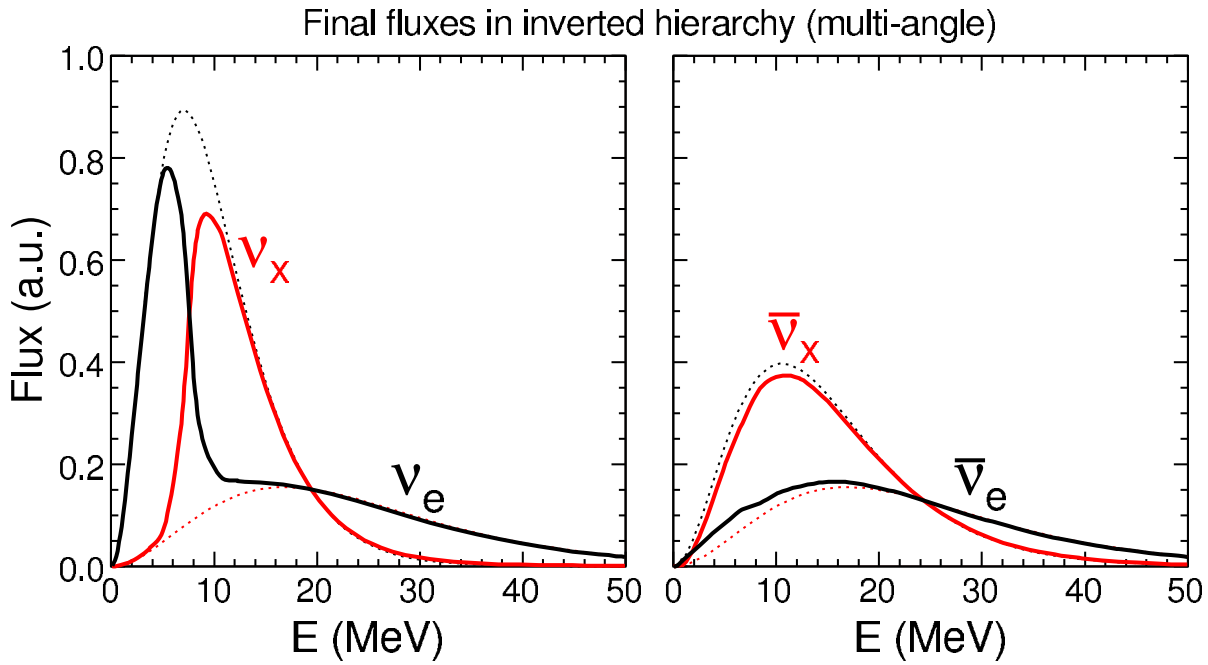

Figure 7: Multi-angle simulation in inverted hierarchy: final fluxes (at $r = 200$ km, in arbitrary units) for different neutrino species as a function of energy. Initial fluxes are shown as dotted lines to guide the eye.

References

1. G. G. Raffelt, "Supernova neutrino observations: What can we learn?," astro-ph/0701677.
2. H. Duan, G. M. Fuller, J. Carlson and Y. Z. Qian, "Simulation of coherent non-linear neutrino flavor transformation in the supernova environment. I: Correlated neutrino trajectories," Phys. Rev. D **74**, 105014 (2006) [astro-ph/0606616].
3. G. L. Fogli, E. Lisi, A. Marrone and A. Mirizzi, "Collective neutrino flavor transitions in supernovae and the role of trajectory averaging," arXiv:0707.1998 [hep-ph].
4. S. Hannestad, G. G. Raffelt, G. Sigl and Y. Y. Y. Wong, "Self-induced conversion in dense neutrino gases: Pendulum in flavour space," Phys. Rev. D **74**, 105010 (2006) [astro-ph/0608695].
5. H. Duan, G. M. Fuller, J. Carlson and Y. Z. Qian, "Analysis of Collective Neutrino Flavor Transformation in Supernovae," Phys. Rev. D **75**, 125005 (2007) [astro-ph/0703776].
6. S. Pastor, G. G. Raffelt and D. V. Semikoz, "Physics of synchronized neutrino oscillations caused by self-interactions," Phys. Rev. D **65**, 053011 (2002) [hep-ph/0109035].
7. G. G. Raffelt and A. Y. Smirnov, "Self-induced spectral splits in supernova neutrino fluxes," arXiv:0705.1830 [hep-ph].
8. B. Dasgupta, A. Dighe and A. Mirizzi, "Identifying neutrino mass hierarchy at extremely small theta(13) through Earth matter effects in a supernova signal," arXiv:0802.1481 [hep-ph].